January 2014

Size and Texture Effects on Ferroelectrics

Sarah E. Leach
Purdue University

Graduate School ETD Form 9
(Revised 01/14)

PURDUE UNIVERSITY
GRADUATE SCHOOL
Thesis/Dissertation Acceptance

This is to certify that the thesis/dissertation prepared

By Sarah Ellen Leach

Entitled
SIZE AND TEXTURE EFFECTS ON FERROELECTRICS

For the degree of Doctor of Philosophy

Is approved by the final examining committee:

R. Edwin Garcia

Ganesh Subbarayan-Shastri

John E. Blendell

Keith J. Bowman

To the best of my knowledge and as understood by the student in the *Thesis/Dissertation Agreement. Publication Delay, and Certification/Disclaimer (Graduate School Form 32)*, this thesis/dissertation adheres to the provisions of Purdue University's "Policy on Integrity in Research" and the use of copyrighted material.

R. Edwin Garcia

Approved by Major Professor(s): _____

_____

Approved by: David Bahr 10/10/2014

Head of the Department Graduate Program Date

SIZE AND TEXTURE EFFECTS ON FERROELECTRICS

A Dissertation

Submitted to the Faculty

of

Purdue University

by

Sarah E. Leach

In Partial Fulfillment of the

Requirements for the Degree

of

Doctor of Philosophy

December 2014

Purdue University

West Lafayette, Indiana

ACKNOWLEDGMENTS

Many thanks to my adviser, R. Edwin García, who patiently provided invaluable insights, guidance, and encouragement during this research. I also thank the other members of my committee, Keith Bowman, John Blendell, and Ganesh Subbarayan for their constructive discussions and suggestions.

Thanks are also due to collaborators and co-authors Valanoor Nagarajan of the University of New South Wales and Yuanyuan Jing of Purdue. The student members of the piezoelectrics research group: Meredith Rogers, Chris Fancher, Özgür Keleş, Zizhao Zhao, and Matthias Ehmke contributed useful discussions, observations, and insights. Fellow García research group students Zhiwen Liang and David Ely also offered valuable suggestions and advice.

I would also like to thank Professor Emeritus Al Miller, University of Notre Dame du Lac for sharing his wisdom and infectious appreciation for materials science. Finally, I thank my husband for his unwavering confidence and support.

TABLE OF CONTENTS

Page

LIST OF TABLES

LIST OF FIGURES

Figure Page

Appendix Figure Page

SYMBOLS

C_{ijkl}	elastic stiffness tensor
d_{ijk}	piezoelectric tensor
d_{ij}	piezoelectric tensor (reduced index form)
D_i	total polarization vector
e_{ijk}	piezolelectric tensor (e-form)
E_c	coercive electric field magnitude
E_i	electric field vector
F	Helmholtz free energy
M	polarization mobility
P_r	remnant polarization
P_k	polarization order parameter
Q_{ijkl}	electrostrictive tensor
Y	Young's modulus
α_{kl}	thermal expansion tensor (kl-th component)
β_{ml}	dielectric susceptibility
ε_{ij}	strain tensor
$\overleftrightarrow{\epsilon}$	permittivity tensor
ϵ_{ij}	dielectric permittivity tensor
κ_{ij}	relative dielectric permittivity tensor, dielectric constant.
ν	Poisson's ratio
ρ	local charge density
χ_{ij}	dielectric susceptibility tensor
$\chi_\circ$	effective mesa elastic modulus

ABSTRACT

Leach, Sarah E. Ph.D., Purdue University, December 2014. Size and Texture Effects on Ferroelectrics. Major Professor: R. Edwin García.

Analytical and numerical theories are proposed to describe the polarization hysteresis behavior of individual PZT grains as a function of epitaxial strain and crystallographic orientation for polycrystalline ferroelectrics. The film stresses and average remnant polarization are shown to be controlled by the aspect ratio of the mesa. Calculations demonstrate that the stresses at the edges are relaxed for film height, h_f, to mesa width, w, ratios $h_f/w \leq 1 \times 10^{-4}$. For $h_f/w \geq 1 \times 10^{-2}$, the effective in-plane stress is relaxed throughout the deposited film. Moreover, the effective stresses at the center of the mesa are 15% of the stresses of an infinitely wide film, $h_f/w \to 0$. For films with $h_f/w = 0.0011$, the remnant polarization decreases from 0.69 C/m^2 for highly textured films to 0.66 C/m^2 for untextured films. Results show that as $h_f/w \to 1$, the average value of remnant polarization decreases to approximately 0.64 C/m^2. This means that small mesas will have a reduced value of remnant polarization compared with infinitely wide films, but the remnant polarization does not decrease to zero. For an individual grain in a polycrystalline ferroelectric, enhanced or inhibited hysteresis behavior is observed, depending on proximity to the grain boundaries, the orientation of the grain to adjacent grains, and the orientation of the grain with respect to the geometry of the thin film. Grain boundaries with different misorientation angles create different local strain fields that couple to the local electric field via the piezoelectric effect, and change the switching behavior of adjacent regions. For 100 nm diameter grains, the coercive field required for polarization switching can vary approximately $\pm 10\%$ between a region near a grain boundary and one near the grain center.

CHAPTER 1. INTRODUCTION

1.1 Motivation

Thin film ferroelectrics have generated a great deal of interest in the fabrication of low-voltage non-volatile memory, sensors, and actuators [1–5]. The commercial market for non-volatile memory as valued in excess of 10 billion dollars in 2009 and was projected to exceed 20 billion dollars in 2014 [6]. The demand for ferroelectric materials in non-volatile memory is driven primarily by the need for lower power devices. In all applications, the stress state of a thin film influences its response to an externally applied electric field. The stress state controls the electrostrictive, ferroelectric, or piezoelectric behavior, and influences the coercive field necessary to switch, the symmetry of the hysteresis loop, and the remnant polarization value [7–10]. An accurate and detailed understanding of the response of ferroelectric materials, in both single-crystal and polycrystalline thin film form, is necessary to understand and engineer optimal performance. This understanding needs to derive from appropriately chosen analytical and computational modeling. Ideally, the modeling needs to capture the underlying physics of ferroelectric switching for actual materials and devices. The challenge is to include relevant information from a range of length scales, anisotropic material properties, and device dimensions.*

1.2 Literature Review

The field of ferroelectric materials has undergone enormous advances since its advent in the 1940s. A great deal of progress in the chemistry, microstructure design, processing, and characterization techniques has paved the way for the introduction of

*The material in this chapter was the basis of the publication: S. E. Leach and R. E. García. "Microstructural modeling of ferroelectric materials: state of the art, challenges and opportunities." *Materials Science Forum* 606:119-134, 2009.

high performance actuator, sensors, and memory devices [4, 11, 12]. Supporting this continuing effort, the theoretical understanding of ferroelectric materials has evolved into a sophisticated set of accurate analytical and numerical descriptions (models). New materials, technological applications, and freshly discovered multiphysical phenomena have added challenges and opportunities. The rich theory of ferroelectrics spans three length scales: atomistic, mesoscopic, and macroscopic. After nearly eighty years of ongoing ferroelectric research, myriad models, numerical implementations, and theoretical approaches have emerged to describe the underlying multifunctionality associated with ferroelectric materials and devices in both single-crystal and polycrystalline forms. Each of these descriptions has specific strengths and weaknesses in terms of their underlying complexity and the length scale that they are able to represent.

Traditional atomistic approaches capture the equilibrium and time dependent behavior for systems in the range of femtoseconds and have led to great improvements in the chemistries of these systems [13, 14]. Similarly, macroscopic engineering approaches have focused on the development of phenomenological descriptions which capture the empirical static and time-dependent behavior (for longer time-scales) [15–17]. At the interface of these two apparently disparate approaches, thermodynamic-based microstructural evolution descriptions inspired by phase field models have risen as the necessary link between the atomic and macroscopic levels. This method starts from the predicted behaviors given by their atomic counter-parts, but resolves the effects of grain boundaries and deconvolves the grain-grain mesoscopic interactions. Much of the future of ferroelectrics modeling lies in the delivery of improved chemistries and microstructures and upon bridging currently existing atomistic and continuum descriptions. However, understanding ferroelectric fatigue, realizing optimal performance from lead-free materials, and developing theories and models to describe the emerging field of multiferroics, will continue to motivate ferroelectrics modeling. Moreover, while it is expected that an accurate understanding of the intrinsic properties of materials is the key to define improved ferroelectric solids,

it will be the detailed understanding of the the extrinsic response of ferroelectric materials, in both bulk and thin film form, that will enable these materials to reach optimal performances which are yet to be realized.

A ferroelectric material is typically defined in terms of a reorientable spontaneous electric dipole moment. Here, an imposed temperature or stress field alters the material's crystallographic symmetry thus inducing the loss of an inversion center. The change in crystallographic symmetry is followed by a spontaneous change in strain and electric polarization (a first order phase transition). Such a material is called ferroelectric if it has two or more orientation states in the absense of an electric field and can be shifted from one to another of these states (variants) by an applied electric field [18]. In many of these materials, the local state of polarization is directly correlated to the crystal structure of the system. For example, in tetragonal ferroelectrics [19], the degree of tetragonality is directly correlated to the state of polarization of the unit cell. At equilibrium, in a stress-free ferroelectric solid, the direction of the polarization order parameter vector lies along the c-axis of the unit cell. Regions of crystallographically equivalent material with aligned polarization are called domains.

One of the major standing challenges in the modeling of ferroelectrics is the accurate mathematical representation of domain kinetics and their associated temperature-dependent velocity. This fundamental ferroelectric materials challenge spans many time and length scales and has been recast and analyzed for every material chemistry of interest. The detailed understanding of the underlying domain switching processes in a ferroelectric material is of critical importance for the improvement of electromechanical actuators and for the engineering of memories where the total switching time affects the write/read time of the device [4, 5, 20, 21]. While optimal single-crystal equilibrium and kinetic properties are the basic building blocks (and the ideal element) for accurately controlling the performance of these electromechanical systems, their high costs or the technological complexity to fabricate such systems has led to the exploration of systems in polycrystalline form. Polycrystalline ferroelectric

materials, however, pose an additional geometrical complexity. Every single grain is a highly nonlinear, multiphysical, time-dependent, anisotropic system that is spatially interlocked to the surrounding grains. Furthermore, the local thermodynamic state and ferroelectric domain configuration that emerge as a result of the local grain-grain interactions directly impact the response of the solid. Figure 1.1 illustrates such behavior for PZT. Here, at the center of each grain, 90° and 180° domain walls emerge in a simultaneous effort to minimize the free energy of the system and to match spatially compatible crystallographic variants. In the proximity of a grain boundary, domain walls bend to accommodate the continuity of the lattice and guarantee spatial compatibility of the two single crystal grains. An accepted general theory to describe the kinetics and thermodynamics of such physical systems does not exist. A great number of solutions for specific material systems have been proposed; however, such representations are sometimes contradictory and in only a very few cases agree with experiments or the basic theory of thermodynamics.

Fundamentally, the introduction of atomistics or ab initio representations of ferroelectrics embodies the ideal approach to understand the effects of different types of chemistries on the intrinsic properties of ferroelectric ceramics (i.e., the equilibrium thermodynamic properties, including dielectric, elastic, and piezoelectric constitutive behavior). The use of atoms as the smallest unit to describe the behavior of ferroelectric materials demands accurate modeling of individual interactions that simultaneously captures the interatomic behavior as well as the quantum mechanistic details associated with nanometer and femtosecond scales [22]. For the $BaTiO_3$ and $PbTiO_3$ systems, a number of researchers have investigated required coercive field as a function of orientation, domain formation, and domain motion [23–31]. Atomistic models have been greatly helpful to understand and predict the fundamental nature of single-crystal ferroelectrics. However, because each atom must be tracked individually, the number of atoms required to perform a valid calculation, even for nanometer-sized volumes, requires prohibitively complex computation. Moreover, ab

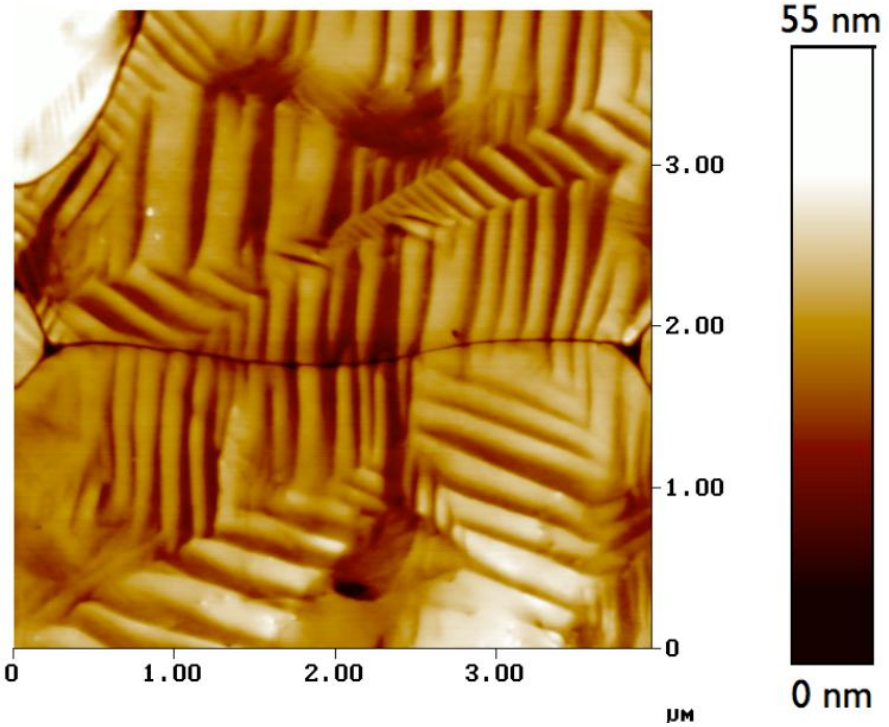

Figure 1.1.: Polarization domain distribution, as measured through Atomic Force Microscopy. The intensity contrast corresponds to the surface height that results from the orientation of the remnant strain of 90° and 180° domains. Note that the orientation of the domain walls, typically specified by the crystallography of the available variants, is altered by the excess of free energy at grain corners and boundaries (Image appears courtesy of Prof. John Blendell).

initio approaches are therefore unable (or do so with great difficulty) to capture the long-range interactions in polycrystalline films.

In the specific case of ferroelectric actuators, atomistic modeling has positioned itself as a key ally to find improved chemistries and greater piezoelectric constants. However, such an ideal is limited by the laws of thermodynamics and the crystallography of the system which imposes constraints on what is physically possible. Figure 1.2 illustrates such limitations. Here, the single-crystal, intrinsic piezoelectric response

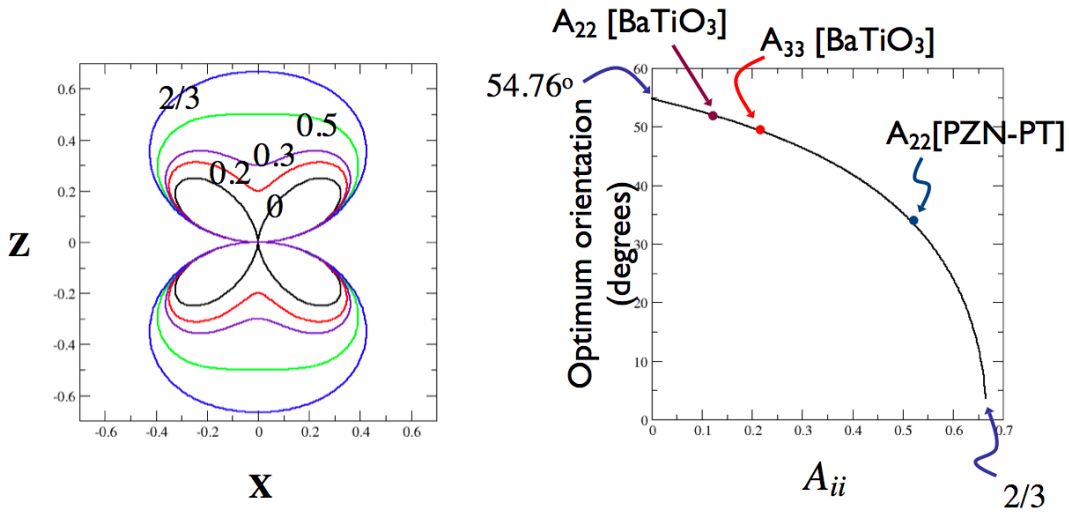

Figure 1.2.: Effect of piezoelectric anisotropy on the single-crystal orientational behavior. Left inset embodies the polar response of the normalized piezoelectric behavior for different anisotropy factors. Note that the optimal orientation changes as the degree of anisotropy increases. Right inset shows the optimal orientation of each single-crystal, as a function of crystallographic anisotropy. Note that contrary to what it is intuitively expected, in the limit of high anisotropy, $A_{ii} \to 2/3$, the crystallographic orientation at which highest piezoelectric strains will occur will asymptotically align with the direction of the applied field. Furthermore, the optimal orientation for materials with weak anisotropy will asymptotically converge to $\theta = 54.76°$. This is the angle for the (111) direction of a cubic structure.

of a tetragonal material as a function of the orientation angle can be normalized to have the form:

$$\begin{aligned} \frac{\varepsilon_{11}}{d_{31}E_3} &= \cos\theta \\ \frac{\varepsilon_{22}}{(d_{33}-d_{15})E_3} &= \cos\theta(A_{22}\cos^2\theta + \sin^2\theta) \\ \frac{\varepsilon_{33}}{(d_{15}+d_{31})E_3} &= \cos\theta(A_{33}\cos^2\theta + \sin^2\theta) \\ A_{22} = \frac{d_{31}}{d_{33}-d_{15}}; \quad A_{33} &= \frac{d_{33}}{d_{15}+d_{31}} \end{aligned} \tag{1.1}$$

The orientational dependence of ε_{22} (the longitudinal strain along the y-axis) and ε_{33} (the longitudinal strain along the z-axis) possess the same mathematical form, and

the details of the properties are summarized in the anisotropy ratio, A_{ii}, a function of the piezoelectric coefficients, as developed by Lee, García, and coworkers [32].

These normalized electromechanical equations are applicable to any chemistry, and allow researchers to tailor the optimal single-crystal intrinsic response. Furthermore, any improvement in the chemistry of a ferroelectric material will asymptotically converge to an optimal orientation of 54.76° for materials with weak anisotropy, or to 0° in the limit of $A_{ii} = 2/3$. The 54.76° orientation corresponds to the (111) direction of a cubic structure.

Single crystal materials are very expensive and in some cases impossible to fabricate. In response to this challenge, polycrystalline ferroelectrics with controlled crystallographic textures attempt to match, and in some cases overcome the limitations of their single-crystal counterparts. Figure 1.3 summarizes the results for two chemistries, $BaTiO_3$ and PZN-PT, as reported in García et al [32]. Here, numerical predictions demonstrate electromechanical enhancements to the macroscopic intrinsic piezoelectric response with values between 60% and 350% with respect to the corresponding single-crystal physical parameters. However, it is those material systems that harness the extrinsic contributions to strain, i.e., those based on domain wall motion and ferroelectric switching, that demonstrate the greatest improvements to device performance. The following sections review those analytical and numerical descriptions and their advantages and limitations, that would most likely contribute to overcome these challenges and find those processing and operation parameters that will facilitate optimal and reliable memories and electromechanical actuators and sensors.

In contrast to chemistry/atomistic-based approaches, the behavior of devices and materials with dimensions on the order of centimeters has been traditionally approached with designs based on macroscopic descriptions that capture the empirical phenomenological behavior of the analyzed systems. In general, the spatial interactions of fields and material properties in a microstructure depend on fine-scale details. The macroscopic response may vary considerably for similar microstructures

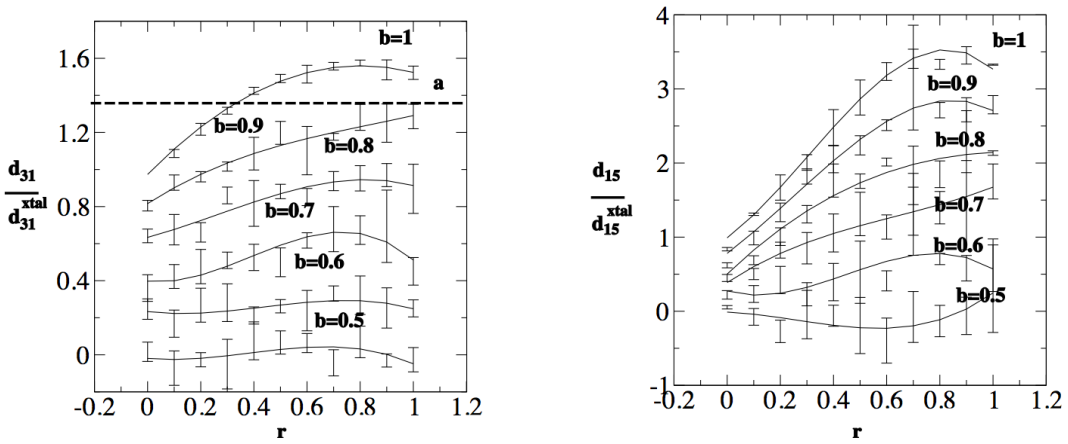

Figure 1.3.: Predicted effect of anisotropy on the macroscopic properties of polycrystalline $BaTiO_3$ (left) and PZN-PT (right), as reported in García, Langer, and Carter [32]. Here, the average and standard deviation response as a function of crystallographic texture and degree of bias was calculated. Results illustrate that although the single-crystal properties may deliver an optimal crystallographic orientation, the corresponding bulk properties may greatly differ due to the local grain-grain interactions and underlying anisotropy (see text and Figure 1.2 for details on single crystal response).

with the same microstructural parameters. To investigate the effects of microstructure on properties, two categorically different approaches have been considered: the fine scale effects can be spatially averaged and the microstructure approximated as a homogeneous material, or the spatial distribution of the properties of a particular microstructure can be incorporated into a complex model that treats all known interactions to the level of spatial resolution. The first, or homogenizing, approach will not describe those macroscopic properties that depend strongly on localized interactions but should be an efficient method for calculation of those properties that depend on the mean of the microstructural distribution. Generally, the homogenization approach derives from fundamental work by Rayleigh and Eshelby [33–37]. For ferroelectric materials specifically, several homogenization approaches have been developed. Most of these methods are based on analytic solutions to electromechanical fields around a piezoelectric ellipsoidal inclusion [38]. The homogenization theory for composites containing piezoelectric inclusions is complex but has been success-

fully developed [39–47]. Another homogenization method, the multiple-scattering method, reduces the calculation of effective properties from a set of integral equations that derive from a Green's function to the superposition of a linear system of equations [48].

While these approaches have delivered great contributions to the description of the equilibrium (or intrinsic) behavior of bulk ferroelectrics, they fail to capture the kinetic (or extrinsic) behavior of polycrystalline ferroelectrics. In response to this challenge, a significant body of literature emerged to capture the measured macroscopic hysteresis behavior for polycrystalline materials. Huang and Tiersten [49] used experimentally determined hysteresis loops to specify the coefficients of a micromechanically-based model [50–52]. Kamlah [51] reviews the development of constitutive models and proposes a microscopically motivated thermodynamic model to describe macroscopic switching. In general, Kamlah, Tsakmakis, and Böhle [53,54] suggest that any macroscopic description which intends to capture successfully the time-dependent ferroelectric behavior is required to specify partial differential equations derived from "balance laws" (i.e., energy conservation, force and momentum balance, charge conservation, etc.) and constitutive equations that capture the individual equilibrium and kinetic properties of the materials involved.

Departing from this deterministic approach, several authors have further developed nucleation and growth-type models of ferroelectric domains based on the classic Johnson-Mehl-Kolmogorov-Avrami theory. Shur [55], in particular, summarized much of the currently ongoing work in a review chapter. Here, he describes the role of such a description in establishing concepts for electrostatic charge screening and its role in the switching behavior. Additionally, Johnson-Mehl-Kolmogorov-Avrami descriptions capture the shapes of evolving domain walls for different ferroelectric materials, describe the role of nucleation in domain wall motion, and identify different domain wall motion mechanisms whose characteristic velocities span several orders of magnitude. The involved researchers have characterized their approach as a phenomenological description of *domain engineering* [56–63]. Fousek et al. [64]

elaborated this concept and established ideas pertaining domain wall thicknesses, their associated contributions to domain nucleation and switching, and the effects of extrinsic contributions to macroscopically measured properties. Smith [65] recently introduced nucleation and domain wall motion kinetics where curved interfaces and domain wall energies are combined. Kalpakides et al. [66] use the level set method to model domain walls as sharp interfaces. The model reproduces the domain structure of a tetragonal ferroelectric, but is applied only to defect-free single-crystal material.

Micromechanical models continue to be an area of active research with models being developed to incorporate additional microstructural or physical features such as polycrystalline structure, defects, or fatigue [67–74]. Landis and coworkers [75–77] made recent advances in micro-electromechanical and macroscopic models that include the associated coupled non-linear behavior. Daniel et al. [78] proposed a multiscale micromechanical model for polycrystalline material. This model allows incorporation of texture, but the approach models the reversible ferroelectric behavior first and then imposes the hysteresis effect. Huber [79] discussed the utility and limitations of micromechanical models and observed that while these descriptions readily describe sharp domain wall interfaces, they do not account for grain-to-grain interactions. Arockiarajan et al. [80] and Jayabal et al. [81] describe models incorporating grain boundary effects, but accomplish this by defining each grain as a finite element.

When the effects due to peculiarities of a particular microstructural feature (such as spatial correlations of crystallographic orientations, morphological texture, interface or boundary proximity effects, or defects such as pore and crack distributions) are to be calculated, homogenization approaches, such as those described above, are very impractical. Homogenization methods that apply to cases where local variations in the microstructural fields are significant or have non-linear couplings, (e.g., electrostriction, photoelasticity, electro-optic effects, etc.) are useful, but equally impractical. Moreover, when material response depends on improbable events or spatial correlations (e.g., when the reliability of ferroelectric devices is considered for those systems with a dilute concentration of defects), homogenization approaches will not

suffice. In response to these challenges, continuum mesoscale formulations capture the behavior of a spatially continuous distribution of material while incorporating the details across tenths and hundreds of nanometers. In many cases, the interfaces themselves are explicitly included in the developed formulations. Several recent reviews detail the development of micromechanical and thermodynamically motivated theoretical descriptions. Setter and Waser [82] recently reviewed advances in electroceramics for the last decade. Bhattacharya and Ravichandran reviewed a selection of recent work [83] with an emphasis on models capturing high strain rates and cracking phenomena. They indicated that a gap remained in the understanding of the effects of defects, motion of domain walls, and morphotropic phase boundaries. Even without a mechanism for incorporating the effects of defects and domain wall dynamics, Zhang and Bhattacharya continued to refine this electromechanical description [84, 85] and added an eighth-order energy barrier to switching. This model predicted moderately higher values of strain and electric field than those measured experimentally. In order to understand the effect of crystallographic texture on high strain rates, Li and Bhattacharya [86] introduced electromechanical contributions to Taylor expansion-based formulations. More recently, Dayal [87] applied the boundary element method to evaluate domain pattern evolution for a ferroelectric material with constrained and unconstrained surfaces.

Historically, theoretical approaches based on the laws of thermodynamics describe the mesoscale kinetics of ferroelectric switching by starting from seminal concepts pioneered by Landau, Devonshire, Jona, Shirane, Allen, and Cahn [88–92]. Here, the state function of a single crystal ferroelectric is defined by expanding in

Taylor series the Helmholtz free energy density, $f = u - Ts$, as a function of the independent degrees of freedom of the system:

$$f = \frac{a}{2}\sum_{i=1}^{3} P_i^2 + \frac{b}{4}\sum_{i=1}^{3} P_i^4 + \frac{c}{6}\sum_{i=1}^{3} P_i^6 - \sum_{i=1}^{3} P_i E_i + \sum_{l=1}^{3}\sum_{k=1}^{3}\sum_{j=1}^{3}\sum_{i=1}^{3} Q_{ijkl}\varepsilon_{kl} P_k^2 P_l^2 + \frac{1}{2}\sum_{i=1}^{3}\sum_{j=1}^{3}\sigma_{ij}\varepsilon_{ij} + \gamma \sum_{i=1, i\neq j}^{3}\sum_{j=1, i\neq j}^{3} P_i^2 P_j^2 + \lambda(P_1^4(P_2^2 + P_3^2) + (P_2^4(P_3^2 + P_1^2) + P_3^4(P_1^2 + P_2^2)) + \xi P_1^2 P_2^2 P_3^2. \quad (1.2)$$

For this theory, a, b, c, γ, λ, and ξ are expansion coefficients that are extracted from the experimentally measured quasistatic hysteretic response of a single-crystal. Physically, the first three terms of the right hand side of first row of the Helmholtz free energy expansion define the equilibrium, stress and electric field free variants of the system. The fourth term couples an externally specified electric field to the local state of polarization. This term biases the stability of those variants that are closer to the applied field. The fifth term couples the state of polarization with the local strain of the system, so that those states of polarization that are parallel to the externally imposed eigenstrains will be thermodynamically favored. Thus, non-trivial states of stress can enhance (or suppress) the local polarization. The sixth term of the equation embodies the energy penalty for accumulating elastic energy in a solid. Similarly, the remaining terms correspond to energy penalties associated with having a polarization vector rotated away from any of their crystallographically allowed variants. These contributions to the free energy greatly penalize the existence of polarization order parameters trapped between stress or electric field free variants.

Many recent models of domain switching in ferroelectric materials are based (or are conceptually equivalent) to the theoretical construction specified above. Here, phase field and other energy minimization approaches generate kinetic equations that are solved through a variety of numerical techniques that span finite differences, finite volumes, and recently through the application of the finite element method. The phase field method, in particular, offers the attractive prospect of describing phase

changes without the necessity of explicitly tracking the location of the domain walls. Recent work has primarily been in the area of validating phase field descriptions through the incorporation of additional terms to account accurately for the total free energy of the system. Successful implementation of phase field models for ferroelectric behavior requires the coordinated use of thermodynamics, mechanics, numerical analysis, and computational science. Hence, the literature for this subject can be found in diverse publications that focus on multiple areas.

A number of researchers have developed the theory of phase-field starting from thermodynamic principles and adapting the Landau-Ginsburg-Devonshire theory [61, 84, 86, 87, 93–97]. Phase-field models have been used to investigate the interaction of domain wall motion with space charges. Xiao et al. [98] included spatially distributed electrostatic charges which were found to interact strongly with 90° domain walls. Su and Landis [69] used discrete charges in a model which combined micromechanical terms with diffuse interface terms and found stronger interactions between 180° domain walls and space charges. Okatan et al. [99, 100] explored the effects of space charges and domain engineering on compositionally graded materials. Schrade et al. [101] modified the order parameter used in the phase-field method to explore the dynamics of domain walls and found that the model predicts a 1.5 times higher mobility for 90° domain walls than for 180° walls. These phase field results have lead collectively to a detailed understanding of the conditions for domain wall motion and pinning. Phase-field modeling has also been used for micromechanical analysis [102] and for phase transitions. Franzbach et al. [103] investigated tetragonal-to-orthorhombic phase transition, and Sun et al. [104] investigated phase transitions as a function of grain size. Recently, Völker et al. [105, 106] developed a multiscale model that links atomistic results to a phase-field model. The free energy equations are adjusted using the atomistic results and through the inclusion of higher-order terms. This enables incorporation of tetragonal as well as cubic elastic behavior. García et al. proposed a thermodynamically based framework for diffuse interface modeling for polycrystalline ferroelectric materials [107]. The numerical implementation of this theory includes

a thermodynamic-based relaxation dynamics description that naturally incorporates Maxwell's equations, resolves the effects of grain corners and boundaries, and incorporates the anisotropy of the underlying components [32, 108, 109]. An example simulation can be observed in Figures 1.4 and 1.5. Here, the effect of microstructure on the out-of-plane electrical and mechanical behavior is analyzed.

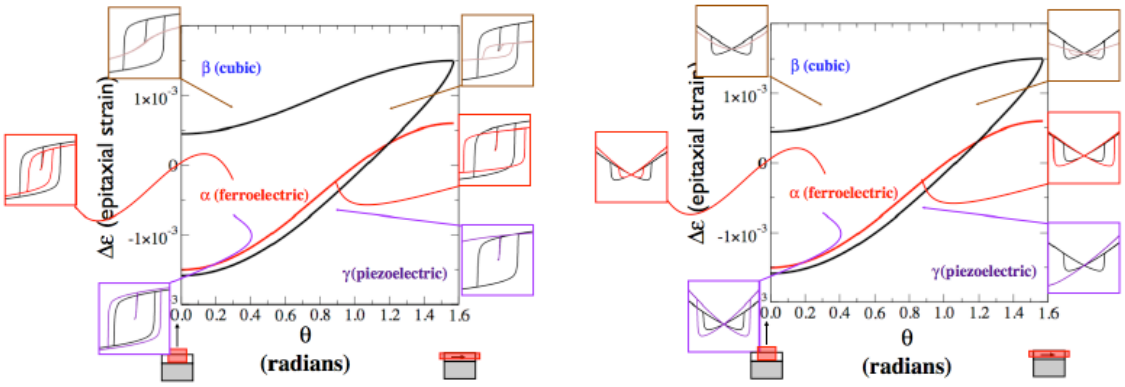

Figure 1.4.: Effect of epitaxial (or deposition) strains on the average extrinsic ferroelectric behavior of a polycrystalline thin-film, as reported by García, Huey, and Blendell [109]. Left inset summarizes the predicted out-of-plane hysteretic response, while the right inset embodies the predicted out-of-plane extrinsic electromechanical behavior. Note that while the electromechanical response for large fields corresponds to the equilibrium (intrinsic) behavior, a great potential for reaching electromechanical enhancements up to one order of magnitude greater than the ones currently available is possible by harnessing the time-dependent switching behavior.

Results demonstrate that: 1) the average state of stress in a ferroelectric film directly determines both the intrinsic and extrinsic butterfly loop response of a ferroelectric film, and 2) the local grain-grain interactions have a deep impact on the built-in electromechanical fields. Furthermore, this analysis demonstrates that the coordinated switching of a solid in thin film form can lead to an improved behavior. While this work suggests that in some cases these interactions can be potentially beneficial, the experimental harnessing and further realization of such performances remains untapped. Moreover, the same microstructural mechanisms that collectively contribute to an improved ferroelectric performance can work against reaching the maximum macroscopic response when used in bulk form. Figure 1.6 illustrates such

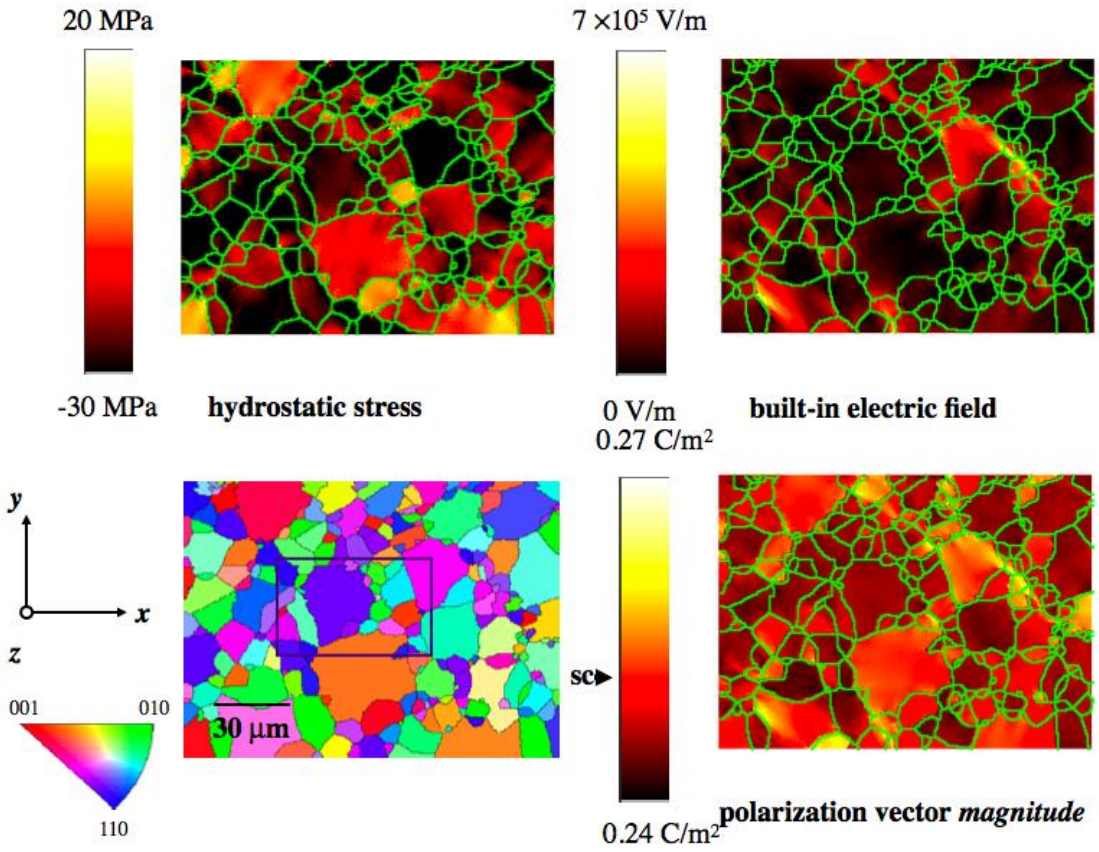

Figure 1.5.: Predicted built-in electromechanical fields in polycrystalline PZN-PT films, as reported by García, Huey, and Blendell [109]. Bottom-left summarizes the crystallographic orientation of each grain, as measured through OIM techniques. Top-left inset shows thermomechanical and electromechanically induced hydrostatic stresses, top-right correspond to built-in electric fields, and bottom-right inset is the spatial distribution of the magnitude of the remnant polarization vector. Note that greatest variations occur at grain corners, boundaries, and in (111) oriented grains. These microstructural features and fields are greatly responsible for specifying the locations and thermodynamic conditions necessary for domain nucleation and pinning, as well as effective out-of-plane polarization enhancements and suppression (see Figure 1.3 and text for further details).

a physical situation. Here, it is clear that a domain whose c-axis is parallel to the applied electric field will try to elongate, while one that is anti-parallel attempts to shrink. A compressive state of stress arises in those grains that are attempting to shrink as a result of the spatial interlocking with those grains that are attempting to elongate. As a result of this behavior, the grains in a compressive state of stress (an-

tiparallel to the applied electric field) will be increasingly polarized and increasingly difficult to switch.

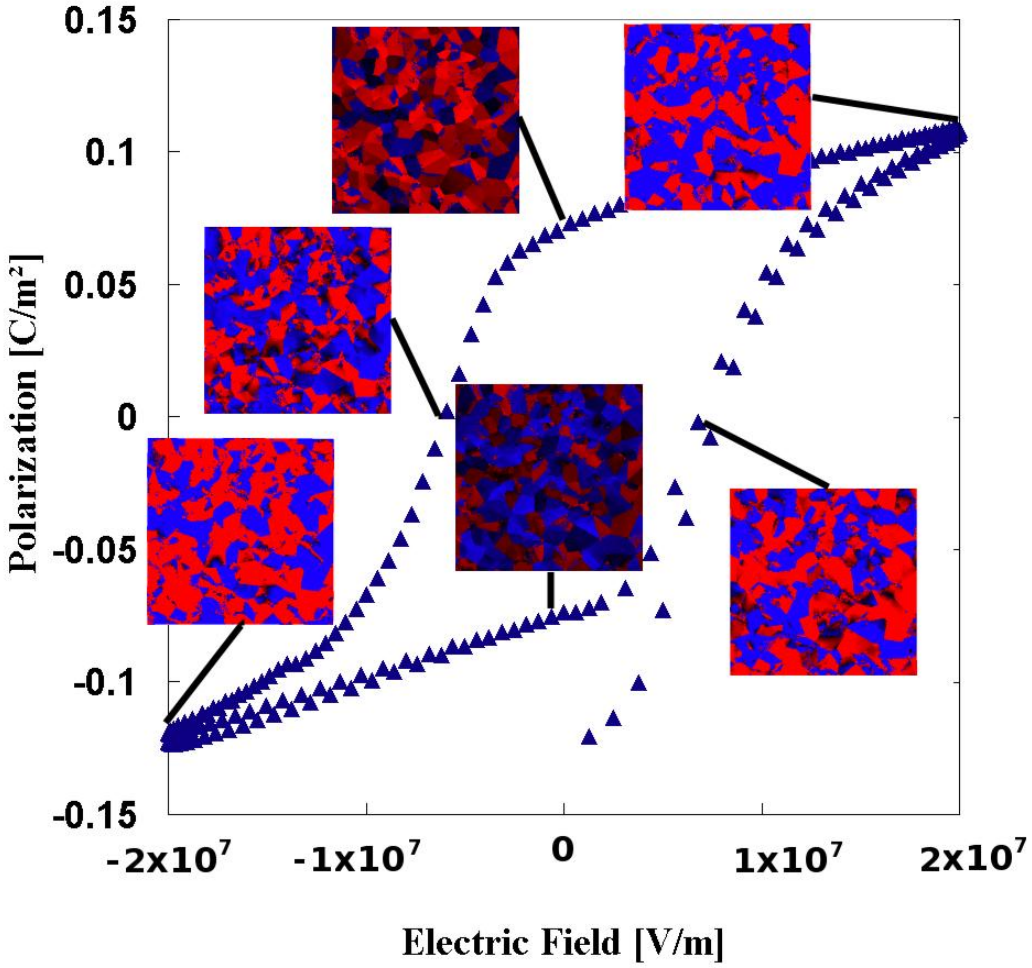

Figure 1.6.: Predicted bulk hysteretic response of polycrystalline, crystallographically untextured PZT sample. Each inset corresponds to the instantaneous distribution of polarization. While it is well known that the bulk hysteretic response is roughly one half of the single crystal behavior (for bulk samples), the microstructural response shows that the interlocking of the grains leads to locally enhanced polarization regions that are macroscopically counteracted through spatial compatibility. Furthermore, the local behavior can be as large as three times the single crystal value, thus suggesting that macroscopic enhancement is possible, provided that the grains cooperate collectively [109].

1.3 Summary and Conclusions

Emerging experimental and theoretical information suggests that a scientific effort that simultaneously engineers the intrinsic and extrinsic electromechanical response of bulk ferroelectric ceramics will lead to greater, never accessed performances. Technological applications, however, will demand memory devices and actuators with higher switching rates, larger remnant polarizations, smaller switchable areas, engineered porosity, and improved lifetimes [2–4,21,110–112]. Furthermore, current trends suggest that the most commonly used piezoceramics, lead titanate/lead zirconates, will be replaced by niobates and perovskite ceramics based on barium titanate and polymers [25, 61, 63, 113–116], in an effort initiated by the environmental policy in the European Union to eliminate lead [117, 118]. In this regard, a better understanding on the degradation and fatigue of ferroelectric materials caused by domain wall pinning, defect agglomeration, or other effects will be critical to deliver commercially viable applications. Theoretical and experimental evidence [58, 119–126] has provided great mechanistic insights into the physics of fatigue, but improved theories and models are required to optimize the microstructure and performance of materials. Recent modeling research includes efforts to include effects of porosity, notches, and cracks [127–129].

In general, improvement in ferroelectric materials is intimately tied to complementary advances in theory, processing, and characterization. In the specific case of improvements in theories and models, it is expected that the advent of multiscale approaches that are able to harness the combined effect of chemistry, microstructure, and materials performance and reliability for all lengthscales [114, 130–132] will lead to improvement in theories and models. Furthermore, mesoscale theories and numerical models based on the diffuse interface approach will become more important as the link between the nano and macro scales, since these descriptions incorporate properties derived from single-crystal measurements or atomistic models, as well as defects, grain boundaries, domain boundaries, and domain interactions, and can di-

rectly characterize the macroscopic behavior of materials and devices, enabling their use as a design tool as well as a means for understanding experimental measurements.

1.4 Thesis Overview

This thesis employs analytical and microstructural modeling to predict polarization behavior as a function of material parameters and device geometries in order to optimize ferroelectric device performance. Results are useful to predict performance criteria and to demonstrate the value of phase field mesoscale modeling. Chapter 2 presents analytical methods to explore the polarization hysteresis behavior of single-crystal thin films as a function of stress and orientation. Results are summarized in terms of epitaxial strain and misorientation which can be used to guide material production towards a desired response. The single-crystal thin film behavior is utilized to understand the polarization response of polycrystalline thin films. A computational model is used to determine the as-deposited stress state and built-in electric field of the film for various distributions of texture. Modeling is then employed to describe the polarization hysteresis behavior of a central grain in the film as a function of film texture and the orientation of the central grain. The behavior of discrete devices or mesas is characterized and developed as a function of mesa size and thickness. Two central grain orientations are used and the simulation characterizes the interactions between texture and mesa size on remnant polarization.

Chapter 3 explores the local stress and polarization results within grains of a polycrystalline material and adjacent to grain boundaries. A microstructural model shows the influence of grain-to-grain interactions on the stress state, built-in electric field, and polarization hysteresis of individual grains. The model is also used to evaluate the conditions which might lead to spontaneous polarization reversal, or back-switching. Grain boundary misorientation is shown to have local effects on remnant polarization and coercive field values even at levels which are insufficient to cause back-switching. The final chapter summarizes the major contributions of the dissertation and proposes areas for future research. Enhancements to the mi-

crostructral modeling tools are suggested to improve the correlation of modeling with experimental results. Additional investigations of the BZT-BCT system are outlined to develop an improved understanding of the phase transformations, properties, and material performance near the morphotropic phase boundary.

CHAPTER 2. EDGE AND SIZE EFFECTS

2.1 Chapter Summary

This chapter describes analytical and microstructural modeling work intended to guide material and geometric parameters to engineer polarization switching behavior for polycrystalline PZT films. The out-of-plane polarization switching of single-crystal and polycrystalline films as a function of crystallographic orientation, epitaxial strain, and mesa aspect ratio is explored. Results for films with large aspect ratios demonstrate a strong correlation of single-crystal properties to the polarization hysteresis behavior of a central representative grain in a polycrystalline film. The average remnant polarization and its variability can also be controlled by the aspect ratio of the mesa, through stress relaxation. Calculations demonstrate that the stresses at the edges are relaxed for film height, h_f, to mesa width, w, ratios $h_f/w \leq 1 \times 10^{-4}$. For $h_f/w \geq 1 \times 10^{-2}$, the effective in-plane stress is relaxed throughout the deposited film. Moreover, the effective stresses at the center of the mesa are decreased to 15% of the stresses of an infinite film. As a consequence, the residual epitaxial stresses resulting from cooling can be mitigated by forming high aspect ratio mesas. Such mesas are also advantageous for applications which require a high density of discrete, addressable locations, as for non-volatile memory devices.*

2.2 Introduction

The thickness to width aspect ratio of ferroelectric films has been found to be of great importance in determining their underlying effective stress [133–138]. Thus, mesa structures with large aspect ratios have lower stress values at the edges when

*This chapter was the basis for the following publication: S. E. Leach, R. E. García, and V. Nagarajan. "Edge and finite size effects in polycrystalline ferroelectrics." *Acta Materialia*, 59:191-201, 2011.

compared with the biaxial stress in a continuous film. The stress state and switching behavior of a polycrystalline film also depends on the crystallographic orientation of the grains in the film. The distribution of crystallographic orientations (texture) determines the grain-to-grain interactions and built-in stresses which result from cooling of the film from the Curie to the operating temperature [32, 109, 139–142]. Experimental results on discrete epitaxial PZT mesas demonstrate that the piezoelectric response is clamped by the substrate and suppressed to values much below the bulk values unless the film is patterned into discrete mesas with lateral dimensions of less than 100 nm [143]. For such small devices, the clamping of the substrate is limited by the total size of the device, so the piezoelectric response approaches bulk values [144]. PZT capacitor mesas with an aspect ratio of unity exhibit hysteresis loops with no change in coercive field with respect to the reported bulk behavior [145]. Thin-film composites and mesas have also shown size-dependent behavior [1, 135, 137, 146–153]. Suhir and coworkers proposed and experimentally verified that the epitaxial strain in finite-size thin-film structures is dramatically different from the same material in continuous film form.

Past modeling efforts used misfit or epitaxial strain to analyze the effects of built-in electric fields [154] and film thickness for PZT [155]. Other modeling efforts focus on $PbTiO_3$ and $BaTiO_3$ systems to predict the effect of compressive epitaxial strain on the polarization switching behavior [156]. Thin film polarization response has also been studied as a function of material symmetry, polarization displacement mechanisms, [8,10,146,157], and grain size [158–160]. In this context, a previous publication by García et al. predicted the out-of-plane hysteretic response of a single-crystal PZN-PT film as a function of misorientation angle, θ, and epitaxial strain, $\Delta\varepsilon$ [109]. Figure 2.1 reproduces these results (dashed line) with the addition of similar results for PZT (solid line). The calculated behavior is a consequence of the anisotropy of the properties of the deposited ferroelectric material and its crystallographic orientation (see Table A.1). The region marked as α indicates the range of $\Delta\varepsilon$ and θ that results in ferroelectric behavior. In the region marked as β, the

material exhibits electrostrictive behavior. In the region marked as γ, the material exhibits piezoelectric behavior. The material properties for PZT promote a wider range of $\Delta\varepsilon$ values where ferroelectric response is favored in comparison to PZN-PT. Insets correspond to representative hysteretic response at selected epitaxial strain and crystallographic orientation values for PZT.

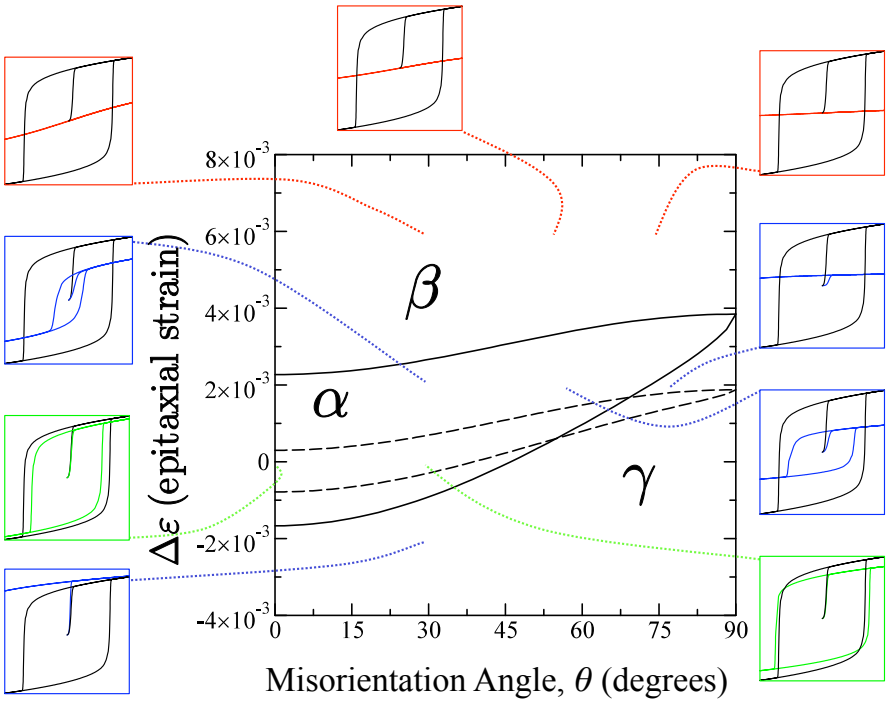

Figure 2.1.: Predicted single-crystal ferroelectric PZT behavior (solid line) compared to previously published PZN-PT behavior (dashed line) [109]. The region marked as α indicates the range of $\Delta\varepsilon$ and θ that results in ferroelectric behavior. In the region marked as β, the material exhibits electrostrictive behavior. In the region marked as γ, the material exhibits piezoelectric behavior. The material properties for PZT promote a wider range of $\Delta\varepsilon$ values where ferroelectric response is favored in comparison to PZN-PT. Insets correspond to representative polarization hysteretic response at selected epitaxial strain and crystallographic orientation values for PZT.

Results from the analytical model described in the next section show that residual stresses are tensile for small misorientations and compressive for large angles. In addition, the epitaxial strain enhances or suppresses the remnant polarization and out-of-plane effective coercive field. The different ranges of behavior are a strong

function of the specific PZT chemistry. Thus, for a commercial PZT (see Table A.2) the different regimes of behavior shift as a result of stiffer elastic properties, weaker electrostrictive constant, and larger stress-free remnant polarization. Figure 2.2 shows the corresponding electromechanical response for the same two materials. The strain hysteresis for ferroelectric behavior exhibits the characteristic butterfly loop shape. Piezoelectric and electrostrictive behavior do not show electromechanical hysteresis.

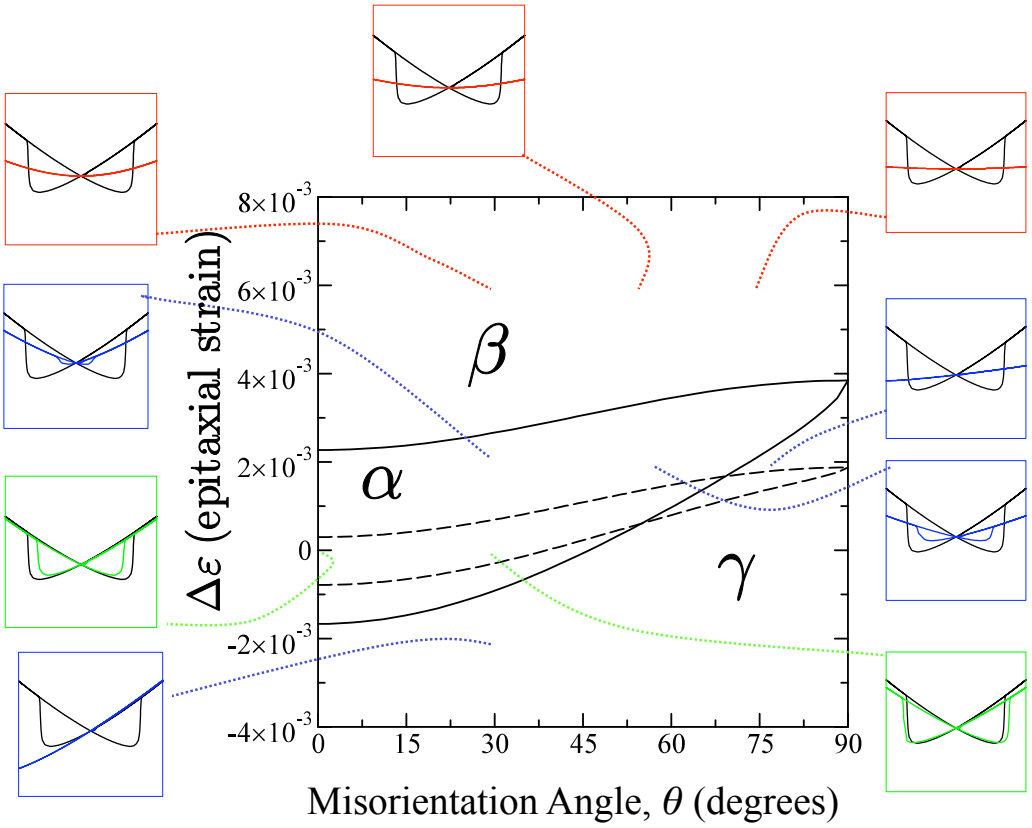

Figure 2.2.: Electromechanical response butterfly loops for single-crystal PZT (solid line) compared to previously published PZN-PT (dashed line) [109]. Ferroelectric behavior is observed in the region marked as α, electrostrictive behavior corresponds to β, and piezoelectric behavior corresponds to γ.

The analytical model presented in this chapter extends previous work and incorporates the effects of the macroscopic edges of the sample. Microstructural modeling assesses the impact on the switching behavior of a representative grain in a poly-

crystalline film. The results are summarized in terms of crystallographic orientation, width, height, and epitaxial strain, into maps, i.e. processing diagrams.

2.3 Theoretical Framework

2.3.1 Thermodynamics of Ferroelectric Materials

The ferroelectric thin film material is modeled using a Taylor series expansion of the Helmholtz free energy density, $f = u - Ts$. For a tetragonal crystal where polarization and strain are the controlling variables, the free energy density takes the form:

$$f(P, \varepsilon_{ij}^T, T, E) = \frac{a}{2}P^2 + \frac{b}{4}P^4 + \frac{c}{6}P^6 - PE + q_{33kl}\varepsilon_{kl}^T P^2 + \frac{1}{2}\sigma_{ij}\varepsilon_{ij}^T \tag{2.1}$$

Where P is the polarization parameter, T is temperature, E is the applied electric field, $\varepsilon^T ij$ is the ij-th component of the total strain tensor, σ_{ij} is the ij-th component of the stress tensor, and q_{ijkl} is the $ijkl$-th component of the electrostrictive tensor. The first four terms of equation 2.1 correspond to the classic Landau expansion as shown in equation 1.2. The fifth term corresponds to the coupling of the strain with the polarization parameter, and the sixth term corresponds to the energy penalty from increasing the elastic energy. The total Helmholtz free energy is given by:

$$F\left(P, \varepsilon_{ij}^T, T, E\right) = \int_\Omega f\left(P, \overleftrightarrow{\varepsilon}^T, T, E\right) d\Omega \tag{2.2}$$

A single-crystal film in a state of biaxial stress is at global equilibrium when the variational derivative of equation 2.2 is equal to zero, *i.e.*,

$$\frac{\delta F}{\delta P} = aP + bP^3 + cP^5 - E + 2q_{33kl}\varepsilon_{kl}^T P \tag{2.3}$$

For cases where the local equilibrium is not reached instantaneously, the polarization order parameter follows the path of steepest descent (in function space)

towards equilibrium. For a case in which the local state of polarization can be described by linearized kinetics:

$$\frac{\partial P}{\partial t} = -M\frac{\partial F}{\partial P} \tag{2.4}$$

where M is the polarization mobility.

The electrostatic and elastic fields of a ferroelectric film are determined by solving the mechanical equilibrium equation and the differential form of Coulomb's Law for each volume element of material:

$$\nabla \cdot \overleftrightarrow{\sigma} = 0 \text{ and } \nabla \cdot \overrightarrow{D} = \rho \tag{2.5}$$

where $\overrightarrow{D}$ is the spatially-dependent total polarization vector and ρ is the local charge density. The local stress and total polarization are coupled through a pair of constitutive equations:

$$D_i = \epsilon_{ij}E_j + e_{ijk}\varepsilon^T_{jk} \tag{2.6}$$

$$\sigma_{ij} = C_{ijkl}\varepsilon^T_{kl} - e_{kij}E_k - C_{ijkl}\alpha_{kl}\Delta T \tag{2.7}$$

ϵ_{ij} is the dielectric permittivity, e_{ijk} is the piezoelectric tensor in its e-form, C_{ijkl} is the elastic stiffness tensor, and α_{kl} is the kl-th component of the thermal expansion tensor. For the most general case, the dielectric, elastic, thermoelastic, and piezoelectric properties are functions of the thermodynamic variables. In particular, piezoelectric properties are coupled to the polarization order parameter through the relationship between the piezoelectric tensor in its d-form, d_{mij}, and the electrostrictive tensor, Q_{ijkl}, the dielectric susceptibility, β_{ml}, and the polarization order parameter, P_k,

$$d_{mij} = Q_{ijkl}\beta_{ml}P_k \tag{2.8}$$

and

$$e_{ijk} = C_{jklm} d_{ilm} \tag{2.9}$$

In order to distinguish between size effects occurring in a single-crystal thin film mesa from the effects of a polycrystalline microstructure (textured or untextured), the effect of size in a single-crystal mesa is analyzed next.

2.3.2 Single-Crystal Mesa Analysis

For a thin film ferroelectric material epitaxially deposited on a thick substrate, stresses are present due to lattice parameter strain mismatch $\Delta\varepsilon$ and a thermal strain mismatch $\alpha_f \Delta T$. For an idealized film with a fixed orientation, the film stress is approximately [137]:

$$\sigma_f = Y_f[\alpha_f \Delta T - \Delta\varepsilon] \tag{2.10}$$

where Y_f is the film's Young's modulus and α_f is the coefficient of thermal expansion. The relationship between the device aspect ratio, h_f/w, and the position-dependent stress is expressed as:

$$Y_f = Y_f^{\circ} \chi_{\circ}(x) \tag{2.11}$$

where Y_f° is the in-plane Young's modulus, $Y_f^{\circ} = Y/(1-\nu)$, x is the distance from the center of the device, and $\chi_{\circ}(x)$ is given by [133]:

$$\chi_{\circ}(x) = 1 - e^{-k(w-x)} \tag{2.12}$$

where the coefficient k is defined as:

$$k = \sqrt{\frac{3[Y_s^{\circ}(1-\nu_s)]}{2(Y_f^{\circ}(1+\nu_s)h_f h_s)}} \tag{2.13}$$

and corresponds to the effective mesa modulus for the film-substrate composite structure. In this expression Y_s° is in-plane Young's modulus of the substrate, ν_s is the

Poisson ratio of the substrate, and h_s and h_f are the substrate and film thicknesses. For thick substrates ($h_s \gg h_f$) and assuming films of constant volume, the normalized stress in the film is described as a function of the film aspect ratio, h_f/w. (see Figure 2.3).

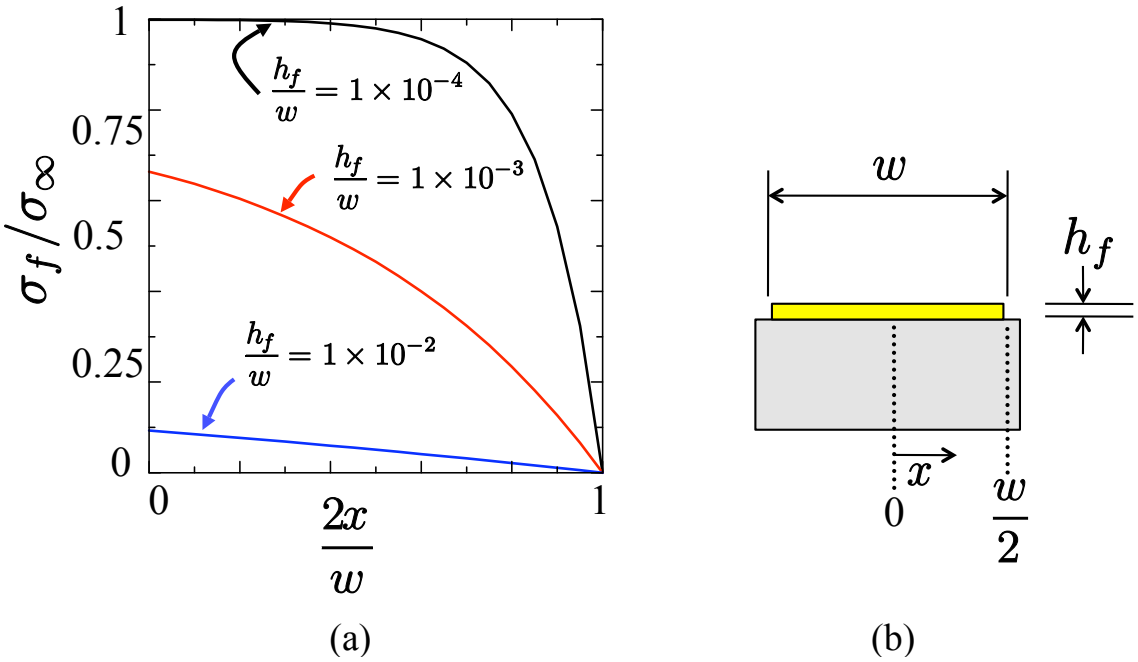

Figure 2.3.: Normalized stress as a function of distance from the center of the mesa for samples with different aspect ratios, h_f/w. The in-plane stress relaxes at the edges of the mesa as a result of the stress-free boundary.

The main advantage of this description, based on Saint Venant's principle, is the possibility of analytically describing the stress relaxation of the off-center axis dependence of the in-plane stresses. In contrast, the model presented herein assumes the out-of-plane stress dependence to be zero and is not able to distinguish between square and circular mesas. In real mesas the shear stresses reach their highest values at the interface between the film and substrate, along the edges and in the corners of a square mesa [161]. A model for circular substrates should include circumferential stresses as described by Suhir [162].

2.4 Single-Crystal Mesa Results and Discussion

For a single-crystal ferroelectric mesa on a thick substrate, stress develops in the film as a consequence of cooling the sample from the Curie temperature. Equation 2.11 predicts that the stress at the center of the mesa will be the same as the one exhibited in an infinite film for $h_f/w \leq 1 \times 10^{-4}$. Figure 2.4 shows that if $h_f/w > 1 \times 10^{-4}$, ferroelectric behavior is favored and accommodates larger values of epitaxial strain. The boundary between ferroelectric and electrostrictive behavior shifts to larger positive values of $\Delta\varepsilon$, while the boundary between ferroelectric and

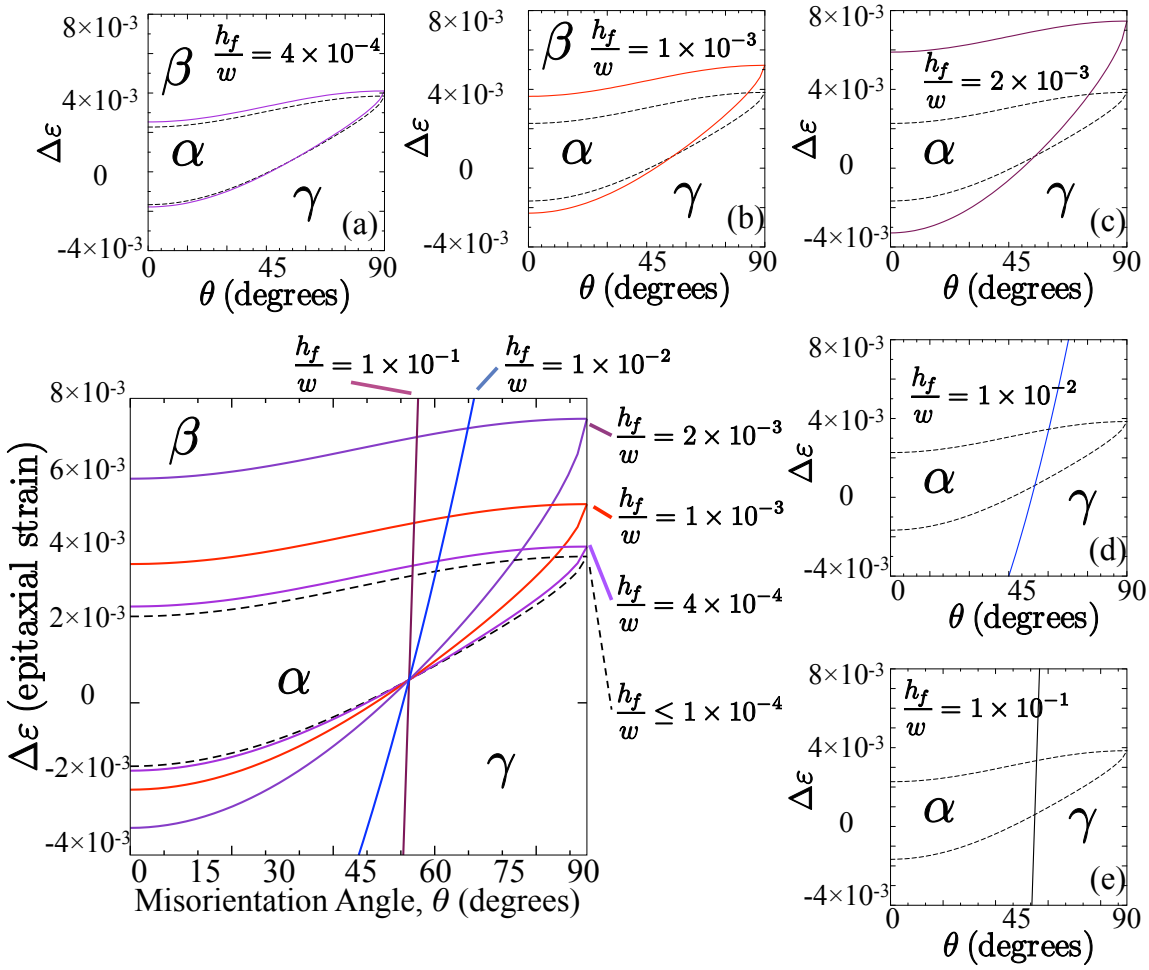

Figure 2.4.: Effect of mesa aspect ratio on the out-of-plane polarization response at the center of PZT mesa for different h_f/w values. Dashed curve corresponds to an infinitely wide film.

piezoelectric behavior shows a critical misorientation of $\theta = 53.67°$, independent of strain. For $h_f/w > 1 \times 10^{-2}$ the sample shows only ferroelectric or piezoelectric behavior for all values of $\Delta\varepsilon$. Results demonstrate that as the shape of the mesa becomes more cuboidal, surface stress relaxation dominates the overall state of stress and associated ferroelectric switching kinetics of the solid. In agreement with experimental results [138,143,163] the out-of-plane ferroelectric behavior is enhanced as the lateral mechanical constraints of (001) oriented tensile films are removed. The out-of-plane response of nearly (011), (010), and (100) oriented films can be engineered by carefully selecting the geometrical aspect ratio of the film. Thus, while high misorientations show ferroelectric behavior for $h_f/w \ll 1$ and $\Delta\varepsilon = 0$, an epitaxial strain of $\Delta\varepsilon = 4 \times 10^{-3}$ can be tuned to deliver any of the electrostrictive, ferroelectric, and even piezoelectric behavior regimes. In practical situations, film thickness and mesa width of the deposited layer are readily controllable processing parameters. These effects are summarized in Figures 2.5 and 2.6.

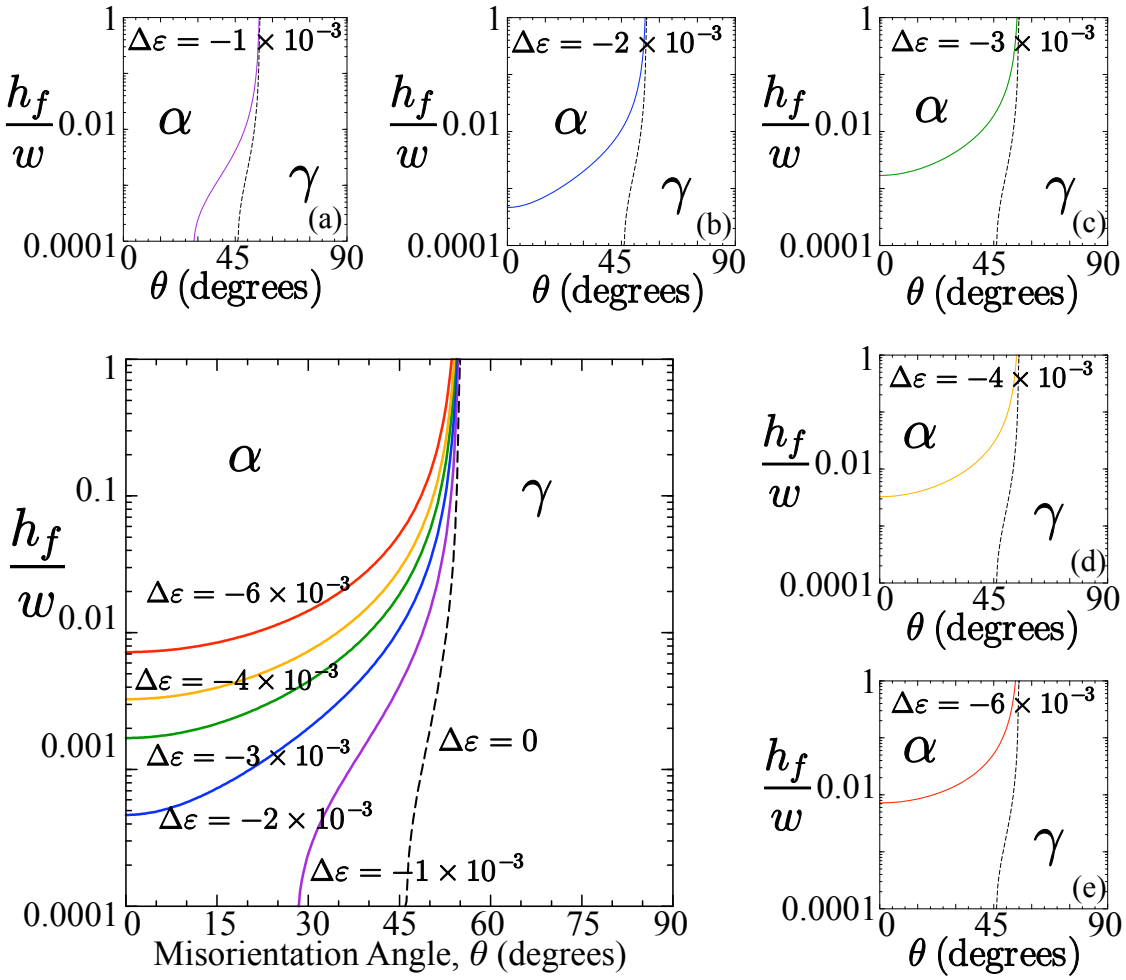

Figure 2.5.: Ferroelectric PZT behavior as a function of aspect ratio and misorientation angle, for values of negative epitaxial strain. In order to achieve ferroelectric behavior for $\Delta\varepsilon > -0.002$, the aspect ratio of the sample must be increased to decrease the effective stress.

Figure 2.5 shows the effect of aspect ratio as a function of c-axis misorientation for compressive strains. Simulations demonstrate that crystallographic orientations beyond the (111) direction will develop a spontaneous polarization but its out-of-plane coercive field is greater than the material breakdown electric field. In contrast, the piezoelectric response is suppressed in films subjected to a tensile strain, as shown in Figure 2.6. Furthermore, for $\Delta\varepsilon > 0.004$ and $h_f/w < 0.0001$, electrostrictive behavior

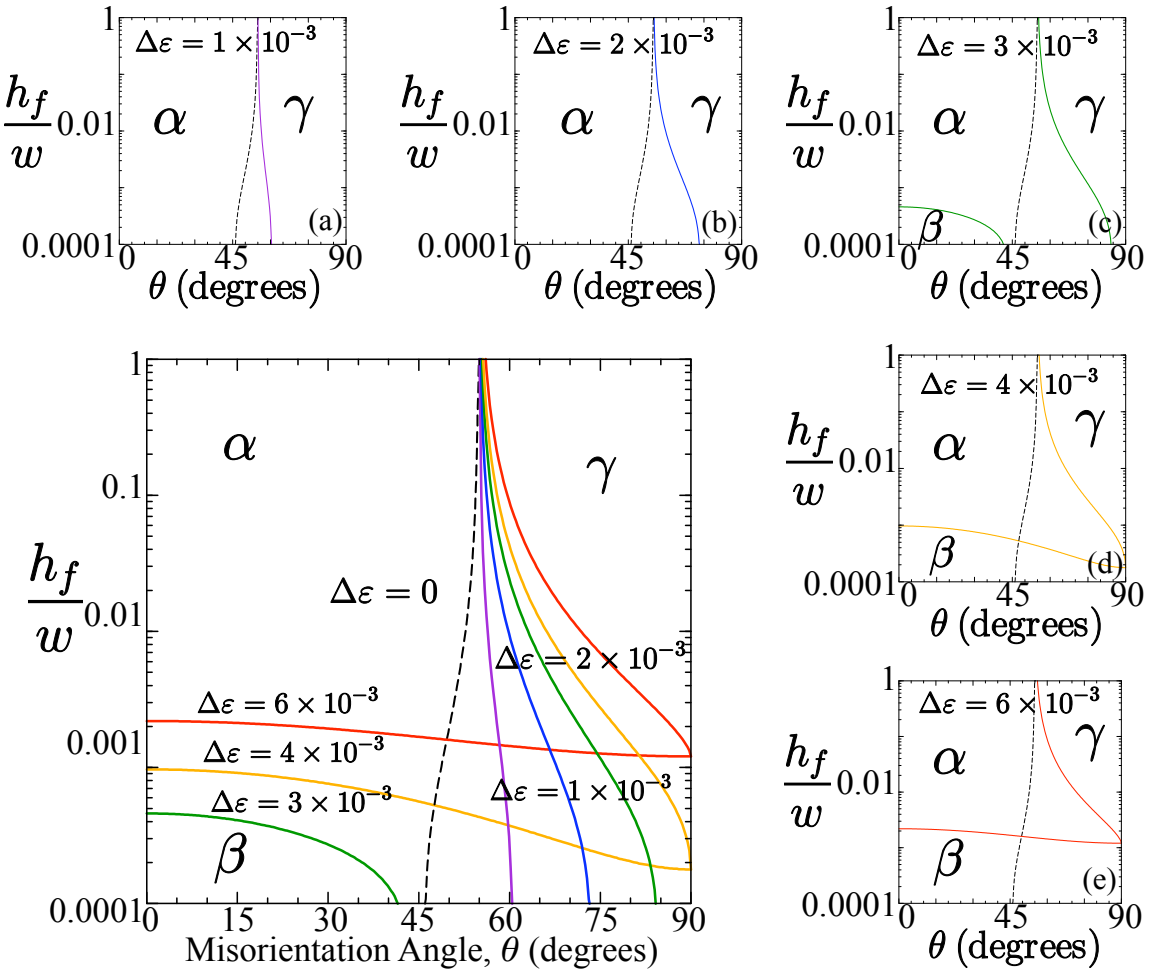

Figure 2.6.: Ferroelectric behavior as a function of size for positive epitaxial strain values. By changing only the h_f/w or $\Delta\varepsilon$ independently, it is possible to influence the behavior of the sample. For example: a sample with a misorientation angle of 75° and $h_f/w = 1 \times 10^{-3}$ would exhibit piezoelectric behavior for $\Delta\varepsilon < 2 \times 10^{-3}$ (a or b), ferroelectric behavior for $\Delta\varepsilon = 4 \times 10^{-3}$ (d), and electrostrictive behavior for $\Delta\varepsilon \geq 6 \times 10^{3}$ (e). A sample with a misorientation angle of 30°, and $\Delta\varepsilon = 3 \times 10^{-3}$ (c) would exhibit electrostrictive behavior for $h_f/w < 3 \times 10^{-4}$, but ferroelectric behavior if $h_f/w > 3 \times 10^{-4}$.

is predicted for all misorientation angles, and ferroelectric switching is suppressed unless the aspect ratio is large enough to relax the effective stress.

The developed single-crystal analysis demonstrates that crystallographic orientation and the mesa aspect-ratio play a critical role in specifying the developed

stress and electromechanical response of the film. With this basis, and in order to assess the effect of grain-grain interactions, a finite element model was developed. The numerical implementation of this model is described next.

2.5 Polycrystalline Film Numerical Model

A model polycrystalline microstructure comprising approximately three hundred grains was constructed based on a Voronoi tessellation from a random distribution of gamma points. A grain size analysis showed that for $h_f/w \ll 1$ the in-plane ferroelectric response reaches an asymptotic, grain-size independent value for simulations comprised of more than 300 grains [32]. The thin film was topologically defined to lie in the laboratory xy-plane with the z-axis parallel to the normal of the film. Grain boundaries were set to be infinitely sharp. Three mesa sizes were analyzed: $w = 100$, 50, and 10 microns. All the grains were assigned a crystallographic orientation by randomly selecting the c-axis orientation of each grain according to a March-Dollase distribution function [164]. This probability distribution describes the orientation distribution of a population of grains using one fitting parameter, r. The misorientation angle, θ, for the grain can take any value from 0° to 90°. The probability density, P, of finding the c-axis of a grain at a particular angle θ from the fiber axis, or in this case the z-axis, is given by

$$P(r,\theta) = \frac{\sin\theta}{(r^2\cos^2\theta + \frac{1}{r}\sin^2\theta)} \tag{2.14}$$

At the limiting value of $r = 0$, all the grains are perfectly aligned with the z-axis (perfect texture). For $r = 1$, the distribution of the grain orientations shows complete randomness (untextured). The probability of finding a specific orientation with respect to an untextured sample, *i.e.* the Multiples of Random Distribution (or MRDs), corresponds to the number of times that a specific orientation is likely to be sampled with respect to a completely random (untextured) sample as reported in the standard literature [165–167]. Here, $MRD = 1/r^3$. The a-axis was assigned

a random direction perpendicular to the c-axis, and the remaining axis was defined to be perpendicular to the first two axes. The defined crystallographic orientation assigment procedure treats all polar angles as equivalent. The object-oriented finite element program (OOF) [168] was extended to model the grain-grain interactions. An initial 125×125 triangular element mesh was laid down on top of the microstructure. The mesh was refined and annealed multiple times to align the mesh elements with the grain boundaries. Equations 2.5 through 2.9 were solved in the finite element analysis program. The equilibrium strains and electric fields are used and Equation 2.4 was solved for every element of the microstructure. An adaptive Runge-Kutta algorithm was used to determine the polarization order parameter. For each value of applied out-of-plane electric field the system was evolved until the polarization reached a steady state value for all elements in the microstructure. The steady state polarization order parameter was then used to recalculate the mechanical and electrical equilibria. The model used non-periodic boundary conditions to simulate a finite-size mesa.

A central grain was selected as representative for polarization hysteretic switching of the microstructure. Using a technique of Virtual Piezo-force Microscopy (VPM) developed by García et al. [109], a sinusoidally varying electric field was applied to this central grain with an amplitude of $1 \times 10^8\ V/m$ at a frequency of 2 radians/second. The out-of-plane polarization state of the central grain was recorded every one-hundredth of a cycle. The crystallographic texture parameter r was varied from $r = 1$ (untextured) to $r = 0.1$ (highly textured) for a (001) textured sample. For a fixed value of texture a Monte Carlo algorithm was used to generate microstructure instances whose microscopic texture corresponds to the March-Dollase function but included the randomness associated with real polycrystals. Ten samples were generated for each texture, all using the same pattern of grain boundaries, in order to assess the variability of the effect of texture on the central grain independent of the shape of the grains comprising the microstructure.

2.6 Polycrystalline Film Results and Discussion

The in-plane hydrostatic stress in a representative untextured one hundred micron-wide film is shown in Figure 2.7(a). Predicted built-in compressive stresses are a result of the thermal coefficient anisotropy and substrate constraint, i.e., [$\alpha_{11} = 5 \times 10^{-7}$ 1/K and $\alpha_{33} = -3 \times 10^{-6}$1/K and $\Delta T = 450°$K]. Thus, as the film becomes increasingly textured, the average in-plane stress undergoes a transition from compressive to tensile. As shown in Figure 2.7(c) the residual stresses are predominantly tensile (positive) because the orientations of the grains in the film are increasingly aligned with the (001) orientation. Figure 2.7(d) shows the microstructure and the central representative grain. Figure 2.8 shows the corresponding built-in electric fields for a one hundred micron mesa ($h_f/w = 1 \times 10^{-3}$) at the same three texture values. Here, as the polycrystal becomes crystallographically ordered, the spatial variations of the built-in electric field decrease. Localized electric field values occur at grain corners and boundaries and coercive field extreme values correlate to regions of large stress values, thus suggesting that piezoelectric-induced built-in fields modify the out-of-plane coercive field of the solid. Figure 2.9 shows the out-of-plane polarization of the film for selected values of texture.

The magnitude of the polarization is directly related to the probability of the c-axis being oriented in the out-of-plane direction. The untextured sample shows small out-of-plane polarization values while highly textured samples are enhanced. The predicted behavior is a result of the self-induced thermomechanical stresses. A comparison between the results of Figures 2.8 and 2.9 demonstrates that increasingly textured polycrystals sample in-plane crystallographic orientations that ultimately lead to average tensile state of stress in the film. Such behavior increases the degree of tetragonality of the unit cell, and thus agrees with the single-crystal results of section 2.2. Figure 2.10 shows the effect of aspect ratio on the built-in hydrostatic stress for untextured samples. As h_f/w increases from 0.001 to 0.01, the effective in-plane stress decreases, which is apparent at the edges and the center of the mesa.

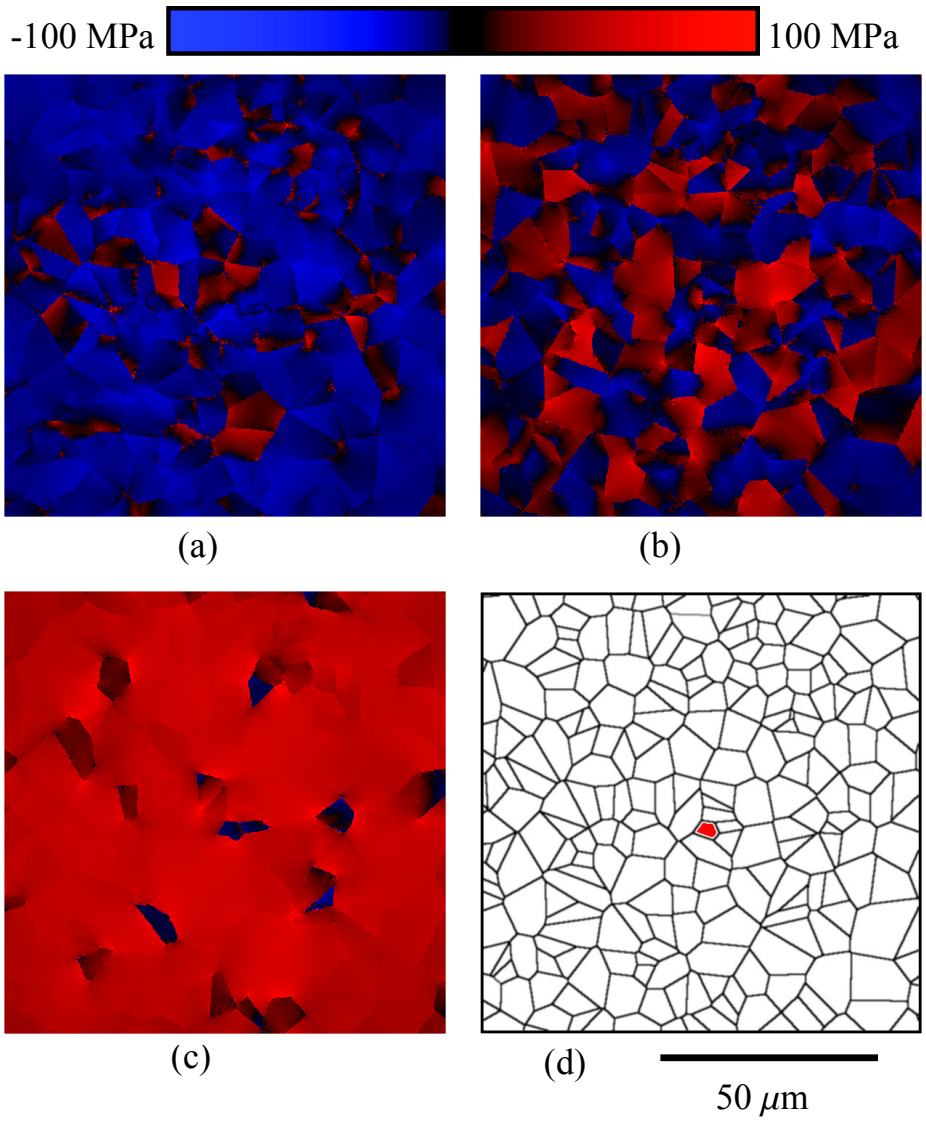

Figure 2.7.: First stress invariant distribution for PZT film, 100 micron film width, $h_f/w = 1 \times 10^{-3}$. (a) shows an untextured film, $r = 1$ ($MRD = 1$), (b) shows a film with $r = 0.5$ ($MRD = 8$) and (c) shows a highly textured film, $r = 0.1$ ($MRD = 1000$). For the untextured film, the thermal expansion coefficients induce compressive residual stresses. As texture increases, residual stresses become tensile (positive), because the orientation distribution of the grains in the film is closely aligned with the (001) direction, in agreement with single-crystal results.

For $h_f/w = 0.01$, the stress at the center of the mesa decreases by more than 15% of the stress expected for a $h_f/w < 0.001$ mesa.

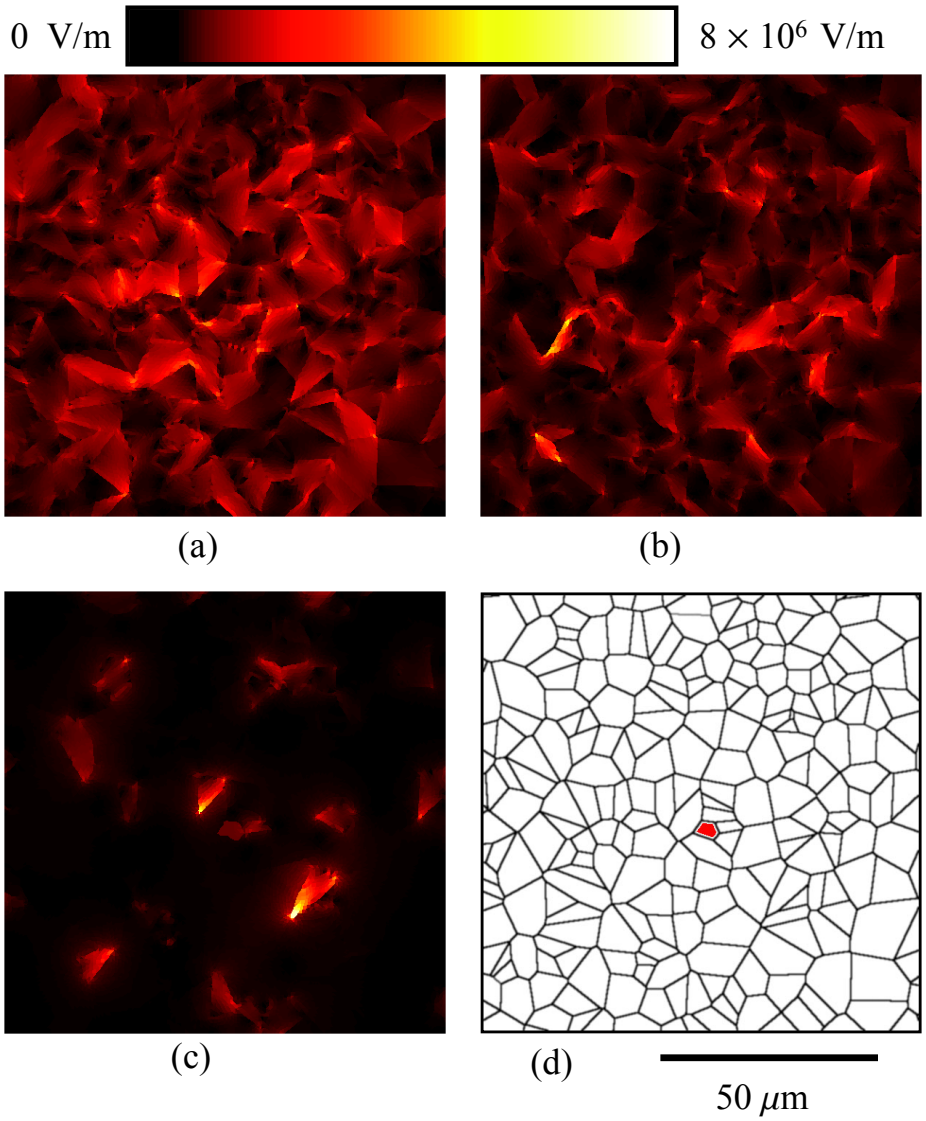

Figure 2.8.: (a) Built-in electric field for untextured film, $r = 1$ ($MRD = 1$), (b) moderate texture, $r = 0.5$ ($MRD = 8$), and (c) highly textured film, $r = 0.1$ ($MRD = 1000$). Built-in electric fields correlate to regions of large stresses.

As the size of the polycrystalline mesa decreases (see Figure 2.10), the average stress and built-in electric fields of the film asymptotically converge to zero. Additionally, the stress and built-in electric field relaxation at the macroscopic edges of the microstructure become increasingly apparent as the aspect ratio of the mesa

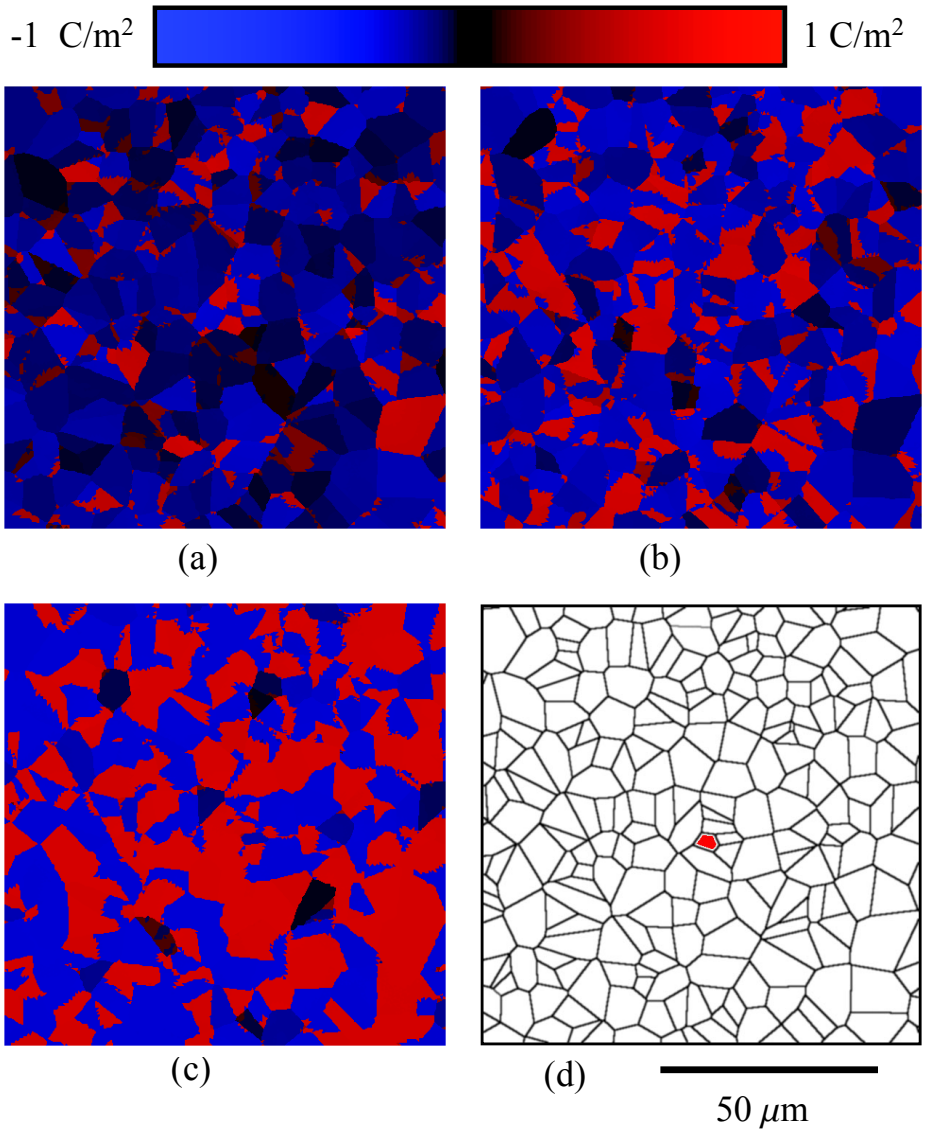

Figure 2.9.: Out-of-plane polarization for untextured film (a), $r = 1$ ($MRD = 1$), intermediate texture (b), $r = 0.5$ ($MRD = 8$) and highly textured sample (c), $r = 0.1$ ($MRD = 1000$). As the film becomes more textured, the c-axis of the grain is more likely to be oriented at an angle near the (001) direction, so the out-of-plane component of the polarization is larger, leading to regions of higher out-of-plane polarization.

becomes more cuboidal. For a representative (001) oriented grain embedded in a tailored polycrystalline PZT network, the remnant polarization decreases by 7.8%.

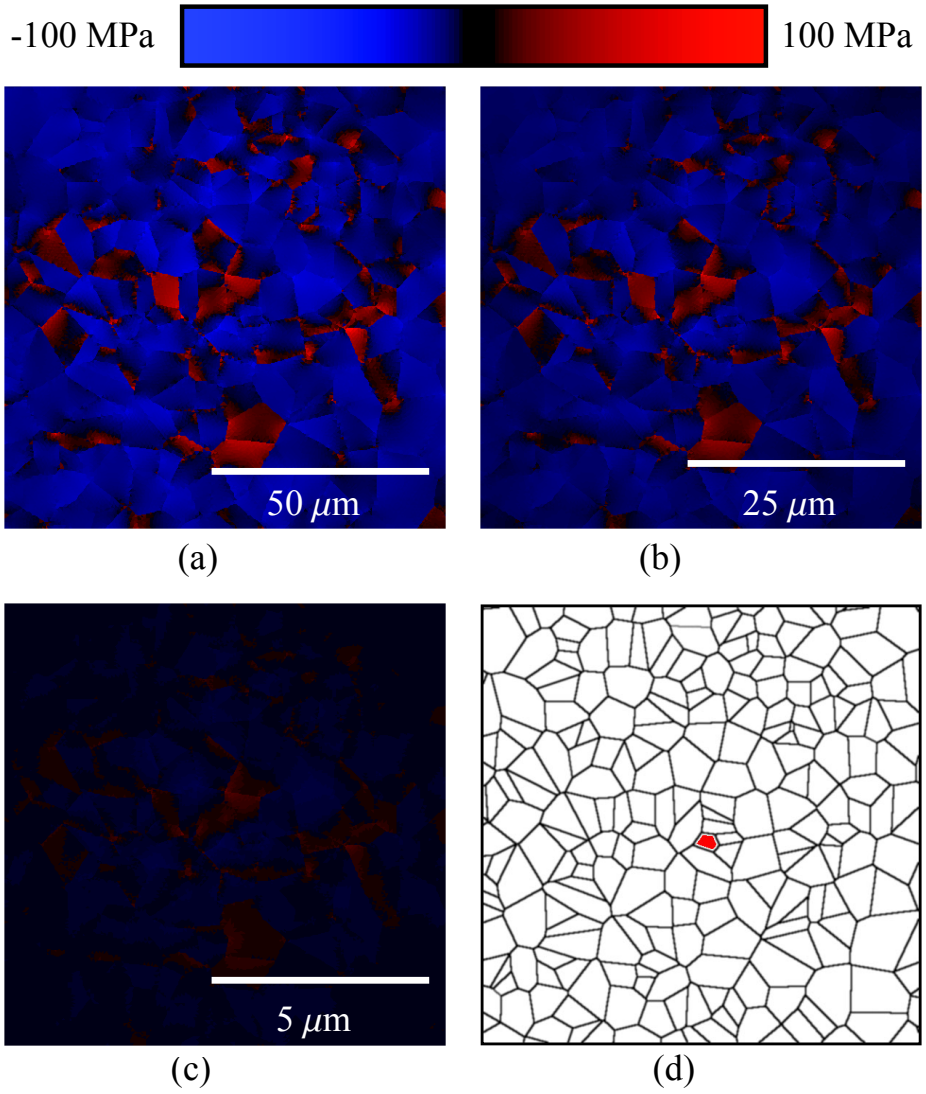

Figure 2.10.: First stress invariant for untextured film samples of three aspect ratio samples: 100 μm ($h_f/w = 0.001$), 50 μm ($h_f/w = 0.002$), and 10 μm ($h_f/w = 0.01$). Simulations show the influence of the size of the sample on the built-in stress, for $h_f = 100$ μm and $h_f < h_s$.

The effect of texture on the out-of-plane remnant polarization for a (001)-oriented grain is summarized in Figure 2.11 for three representative mesa sizes. All of the samples exhibited ferroelectric polarization switching. For films with $h_f/w = 0.0011$ the remnant polarization decreases from 0.69 C/m^2 for highly textured films to 0.66 C/m^2 for untextured films. Results show that as $h_f/w \to 1$ the average

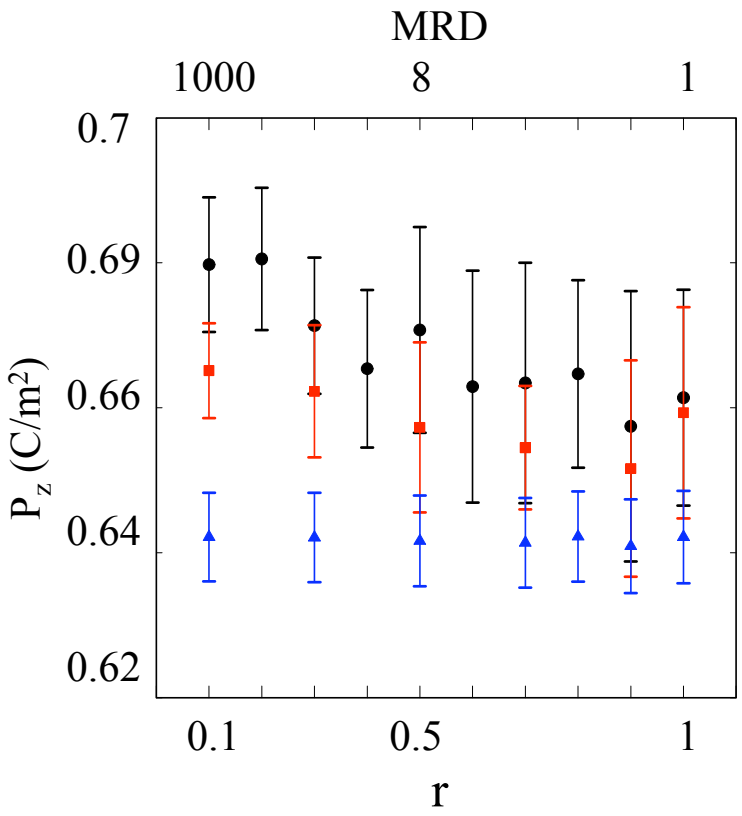

Figure 2.11.: Positive out-of-plane remnant polarization values for three sample sizes, as a function of texture. Central grain is (001) orientation. Circles describe the average remnant polarization for 100 μm samples ($h_f/w = 0.001$). Squares correspond to 50 μm samples ($h_f/w = 0.002$). Triangles correspond to 10 μm samples ($h_f/w = 0.01$). Error bars indicate the value of one standard deviation for a normal distribution. Results show weak dependency on texture and sample size (aspect ratio). The result correlates with behavior of a single crystal with a misorientation angle of 0°.

value of remnant polarization decreases to approximately 0.64 C/m^2, but the effect of texture becomes negligible. Thus, for very thin films spanning large areas, highly textured samples will provide an enhancement of response while cuboidal-looking mesas will be insensitive to texture. In contrast, a (111)-oriented representative grain (see Figure 2.12) shows no texture enhancement effect; however, the in-plane piezoelectric interactions are maximal, leading to a large scatter of the average out-of-plane polarization. All of the center grains exhibited piezoelectric behavior only, as had been

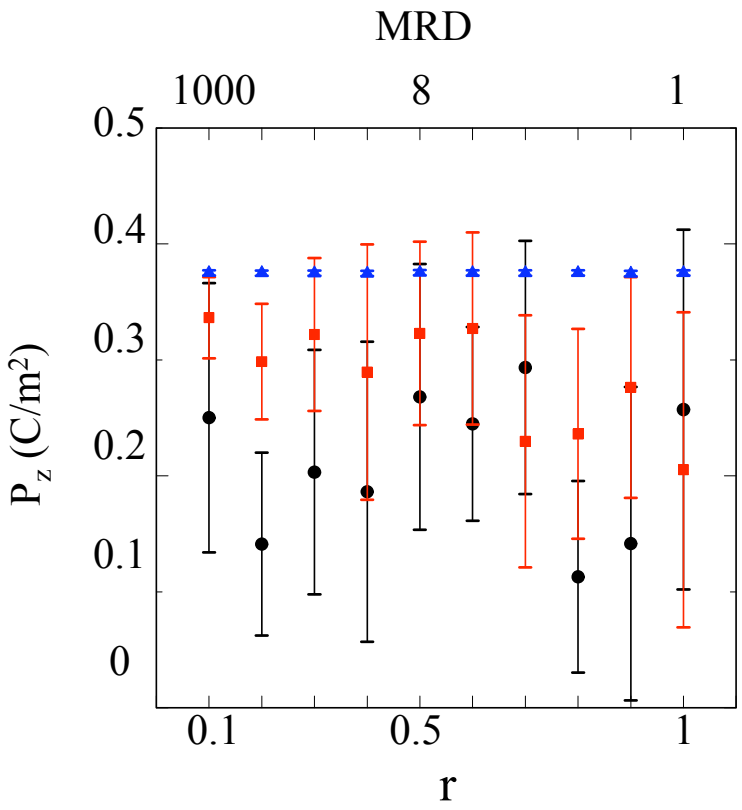

Figure 2.12.: Out-of-plane remnant polarization of the representative (111)-oriented grain. The circles indicate the average remnant polarization for 100 μm samples ($h_f/w = 0.001$). The squares are for 50 μm samples ($h_f/w = 0.002$). The triangles are for 10 μm samples ($h_f/w = 0.01$). Error bars indicate the value of one standard deviation for a normal distribution.

predicted by the behavior map shown in Figure 2.4. Moreover, out-of-plane polarization behavior displays a large degree of scattering for untextured samples because the local coercive field of the (111)-oriented grain is of the same magnitude as the built-in electric field. These effects are removed as the aspect ratio of the deposited polycrystalline layer converges to one. In the stress-free limit, the out-of-plane polarization response experiences an improvement of nearly 100% and directly correlates to the single-crystal response.

2.7 Summary and Conclusions

The out-of-plane polarization behavior for a single grain in a polycrystalline ferroelectric film or mesa can be tailored by manipulating the epitaxial strain, the overall texture of the film, and the geometrical parameters of the layer. Polarization switching of (001)-oriented grains has less variation when the grain is embedded in a mesa with a large aspect ratio due to local stress relaxation. The remnant polarization of piezoelectric (111)-oriented grains is enhanced from an average value of about 0.2 C/m^2 for low aspect ratio films to more than 0.35 C/m^2 for large aspect ratios. The variation in remnant polarization caused by the local stress state of the film is also mitigated through stress relaxation which decreases the built-in electric fields. As shown in Figures 2.5 and 2.6, the physical response can be tuned from ferroelectric to piezoelectric or electrostrictive by specifying the mesa aspect ratio.

In addition to overall texture and geometrical parameters of a polycrystalline film, polarization switching response for an individual grain also depends on the orientation of the adjacent grains. Individual grains can display a whole range of local strain states depending on the individual grain orientation and the distance from a grain boundary. This is shown graphically in Figure 2.8 where some of the individual grains display a range of local built-in electric field depending on location within the grain. The next chapter examines the variation in out-of-plane polarization switching behavior for regions within individual grains and explores the influence of coupling effects between adjacent grains.

CHAPTER 3. GRAIN-GRAIN INTERACTIONS

3.1 Chapter Summary

This chapter examines the effects of residual stresses and polarization switching strains on polarization hysteresis and domain reversal of individual grains and sub-grain domains in polycrystalline thin film ferroelectrics. These effects are important to determine remnant polarization values, polarization stability, and required coercive field values for switching; all of which are significant characteristics in defining device performance for sensors, actuators, or ferroelectric memory. The microstructural model described in Chapter 2 is applied to understand how the built-in electric fields and stresses affect polarization stability and switching within individual grains. Polarization hysteresis is modeled at discrete locations within grains, each measuring 13 nm in diameter. Using a single model microstructure and a central grain with one of two orientations, the polarization and strain response are characterized at locations in the central grain and near grain boundaries in adjacent grains. Built-in electric fields are shown to be smaller than required electrical coercive fields, and so cannot completely account for domain reversal in the absence of an applied coercive field. Strain developed during cooling from the Curie temperature is shown to vary within grains and near grain boundaries sufficiently to influence the required coercive field and remnant polarization values in adjacent grains. The microstructural model results correlate with published experimental results.*

*The material in this chapter was the basis of the following publications:

- S. Wicks, K. Seal, S. Jesse, V. Anbusathaiah, S. Leach, R. E. García, S. V. Kalinin, and V. Nagarajan. "Collective dynamics in nanostructured polycrystalline ferroelectric thin films using local time-resolved measurements and switching spectroscopy." *Acta Materialia*, 58:67-75, 2010.
- Y. Jing, S. Leach, J. E. Blendell, and R. E. García. "Correlated inter-grain switching in polycrystalline ferroelectric thin films." In press, J. of Applied Physics, 2014.

3.2 Introduction

Nanoscale studies by piezoresponse force microscopy (PFM) and macroscale studies by X-ray show that the domain switching in polycrystalline thin films is quite different from that of single crystals [142, 169, 170]. These differences can be attributed mainly to the piezoelectric lattice strain, which is linear to the external electric field in single crystals, but nonlinear in polycrystalline materials. Non-uniform domain switching behavior is believed to originate from the spatially varying local microstructure, defined by grain orientation, grain boundary misorientation, and grain geometry [171]. The anisotropic elastic responses generated by these differently oriented grains and their neighboring grains uniquely define the local stress and electric field that are coupled through the direct and converse piezoelectric effect. The induced field thus reinforces or weakens the applied electric field and results in different switching behaviors for individual grains. For the case of only two stable variants (180° switching only), the free energy density takes the form of Equation 2.1 as described in Chapter 2. This free energy, determined by both the local stress and electric field, is responsible for the grain-to-grain difference in switching behavior.

For a polycrystalline thin film, the orientation distribution influences the stress state and polarization behavior. The hysteresis behavior is influenced by elastic and piezoelectric interactions combined with local grain-to-grain misorientation and grain boundaries [109, 172–174]. Experimental results from Wicks et al. [175, 176] and Jing et al. [177] also reveal that individual grains exhibit initial polarization differences which can be attributed to the location in the grain with respect to grain boundaries and to the edge of the thin film. The effects of local microstructure to determine domain switching were studied by Jing, et al. using Polarization Difference Maps (PDMs) [177]. The effect of grain orientation was confirmed by the observation that for a given external electric field, differently oriented grains showed different switching behaviors [175, 177, 178] (no switching, 90° switching, and 180° switching). The same experiments also revealed that upon the removal of the applied field, many grains

went through relaxation by 90° ferroelastic switching, apparently influenced by the orientations of neighboring grains.

Nagarajan, et al. [179] reported polarization relaxation for individual grains in a polycrystalline PZT thin film. Additional recent experimental work by Jing, et al. [180] explored the switching behaviors of regions within individual grains to understand further the influence of grain boundaries and misorientation of adjacent grains. Boundaries with different configurations were determined to affect the individual grain switching. The switching behaviors of regions within individual nanoscale grains were also analyzed and correlated with proximity to grain boundary and degree of misorientation between adjacent grains. Grain orientations were determined by EBSD. Figure 3.1 shows the results of this experiment and lists the width of the polarization hysteresis loop by position inside 32 individual grains and shows the misorientation angle between the c-axes of the adjacent grains. As seen in this figure, the experimentally measured hysteresis loops near grain boundaries are wider than the loops measured at the centers of grains. This indicates that higher values of coercive field are required for polarization switching near the grain boundaries.

In order to understand the competing mechanisms for domain reversal, Wicks et al [176] applied a synergistic approach that incorporated focused ion beam milling (FIB) [181], time-resolved piezoresponse force microscopy [137, 182, 183], and switching spectroscopy PFM [184] (SSPFM), to provide a unified view of the factors and interactions controlling local polarization dynamics. Gilbert et al. deposited and characterized PZT as a polycrystalline thin film on substrates to form a layer 70 nm thick with an average grain size of 100 nm [185]. The grain boundaries were determined to be vertical, and FIB was used to create mesas approximately 1 micron by 1 micron in size [181]. An atomic force microscope probe tip applied a coercive field and piezoresponse images were acquired repeatedly to determine out-of-plane and in-plane behavior. Figure 3.2 shows the time-dependent out-of-plane behavior for two regions of this material. The top row shows a grain near the center of a mesa, and

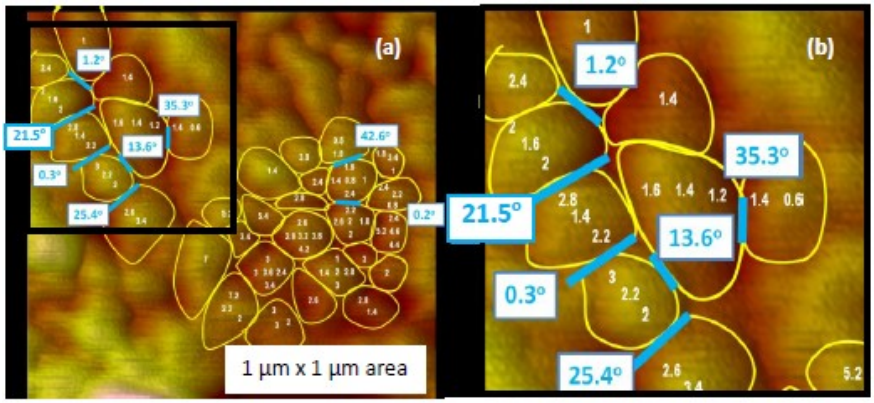

Figure 3.1.: Experimental results from Jing, et al. [180] (a) Loop width map of 32 grains. Loop width data is listed inside the grains, and grain boundary misorientation information is shown in the boxes adjacent to the grain boundaries. The grain boundary misorientation angle labeled is the difference between the c-axis of the two neighboring grains measured experimentally by EBSD. (b) Enlargement of the region inside the black square. A clear correlation of the loop width trend across the grain boundary is observed.(Image appears courtesy of Yuanyuan Jing. [180])

the bottom row shows a grain near the edge of a mesa. In both cases, the first image includes an "x" to mark the grain of interest.

The subsequent images show the grains in the first scan after switching, and then again after a period of time. The grain near the center of the mesa remained in the switched condition, but the grain near the edge spontaneously reversed polarization between the first and second scans, an elapsed time of 9 minutes. Further analysis of the orientations of the switched grains did not reveal a correlation between the orientation of the grain or the out-of-plane polarization component and polarization stability, but did show a correlation between the in-plane polarization component of adjacent grains. That is, the polarization stability was correlated with low in-plane polarization of adjacent grains. A large in-plane polarization of adjacent grains resulted in spontaneous domain reversal of the target grain. This effect was independent of the location of the grain in the mesa. Models for bulk polycrystalline ferroelectric materials propose a close link between polarization switching

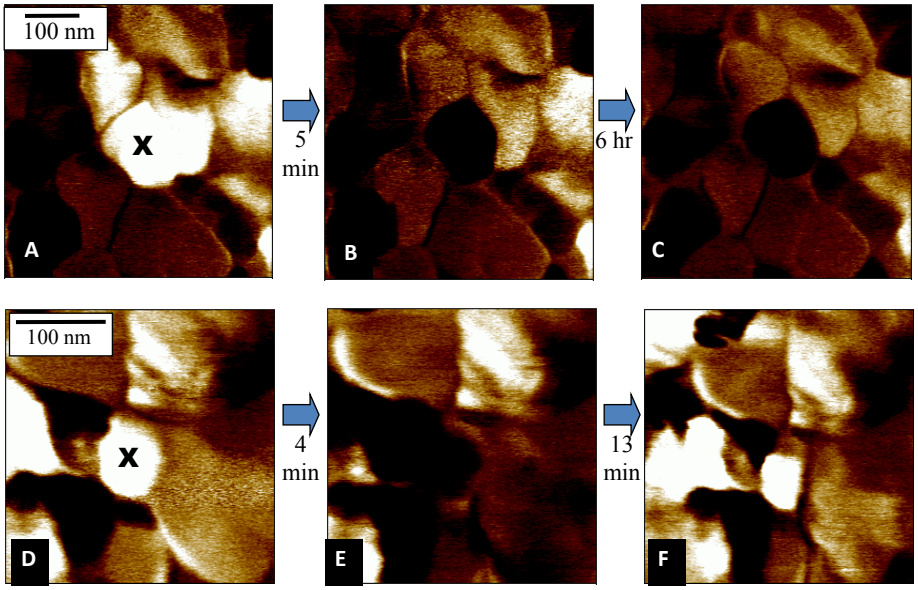

Figure 3.2.: Experimentally acquired vertical piezoresponse force microscopy (OP-PFM) images from Wicks, et al. for different grains as a function of time. Data sets were acquired from a grain at the center of a mesa (top row) and a grain near the edge of the mesa (bottom row). The first image in each row shows the location of the grain before switching. The second image shows the grain in the first scan after switching. The third images show that the top grain has remained stable, while the bottom grain exhibited spontaneous polarization reversal before the second scan was performed at 13 minutes.(Image from [176])

and long-range elastic and piezoelectric strains [67], and recent results indicate that a thorough understanding of the local electromechanical conditions is essential to understand grain-grain interactions in nanoscale ferroelectric devices [169].

3.3 Numerical Model

The object oriented finite element analysis tool, OOF [168] was used to quantify the contributions from the built-in electric fields, the orientational electromechanical coupling of the grains, and spatial grain boundary charge effects on the switching of the grains. These previous approaches do provide invaluable information to describe the physics of ferroelectrics, particularly epitaxial thin films and nanostruc-

tures. However, the FEM tool incorporates the grain boundary orientation effects while simultaneously capturing the effects of the macroscopic edges. Additionally, it can explicitly incorporate the effects of the physical fields (electrical, mechanical, thermal, etc.) which affect the local thermodynamic state of the system. The simulations are direct extension of the effective clamping stress framework for single crystal mesas developed previously [137]. One set of simulations was performed to evaluate the effects of adjacent grains on polarization stability. Here, a central test grain was switched out-of-plane under a virtual PFM tip by using a sinusoidally varying external 8 MV m^{-1} electric field as was reported experimentally. Two orientations were tested: a (0 0 1) orientation to maximize the out-of-plane component of the polarization, and a (1 1 1) orientation to maximize the interaction between the out-of-plane switching and the in-plane effect on neighboring grains.

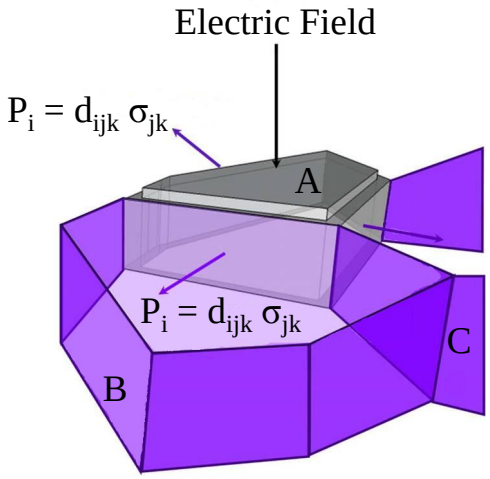

Figure 3.3.: Schematic depiction of possible grain-boundary-induced switching mechanisms for electromechanically coupled grain structure. Here, grain A ((0 0 1) oriented) is switched externally through the application of an out-of-plane E-field. Grains B and C are in turn subjected to stress-induced polarization, polar charge injection or shielding via the direct piezoelectric effect. The intensity of the coupling depends on the misorientation of the abutting grains and underlying material properties. (Image from [176])

A second set of simulations was performed that employed a microstructural model developed to measure the local effects of grain-grain orientation and the variation of physical fields within individual grains. Using initial modeling steps and the VPM method previously described in Chapter 2, a microstructure was generated using a Voronoi tessellation. The microstructure consisted of 169 grains in a 1300 nanometer by 1300 nanometer area. The grain boundaries were defined to be infinitely narrow. The finite element mesh was selectively refined in six grains near the center of the microstructure to enable greater resolution for investigation of phenomena within these grains. The orientation of these central grains was held constant while the remainder of the grains in the film had orientations assigned randomly from a distribution defined by the March-Dollase texture function. The entire microstructure with the central grains indicated, and the refined finite element mesh and virtual probe locations, are shown in Figure 3.4. Simulations were performed for a range of texture, from highly textured to untextured, with the c-axis of the central grain aligned in one of two ways: with the laboratory z-axis, and with the c-axis of the central grain oriented 45° away from the z-axis.

In order to simulate the experimental conditions used by Jing, et al. [177,180], an external sinusoidal voltage from -5 to $+5$ V was applied to areas of approximately 13 nm in diameter. The same locations were used to measure the magnitude of the polarization in the laboratory z-axis. This was an important refinement from previous modeling efforts where the electric field was applied to an entire grain. The simulation used materials properties for PZT and only 180° switching was modeled [174]. Because the sample was a polycrystalline thin film, the built-in stresses and strains resulting from the thermal expansion coefficient mismatch with the substrate were included by incorporating a 300K undercooling from the Curie temperature to room temperature. The substrate was defined to be perfectly rigid with a null thermal expansion coefficient.

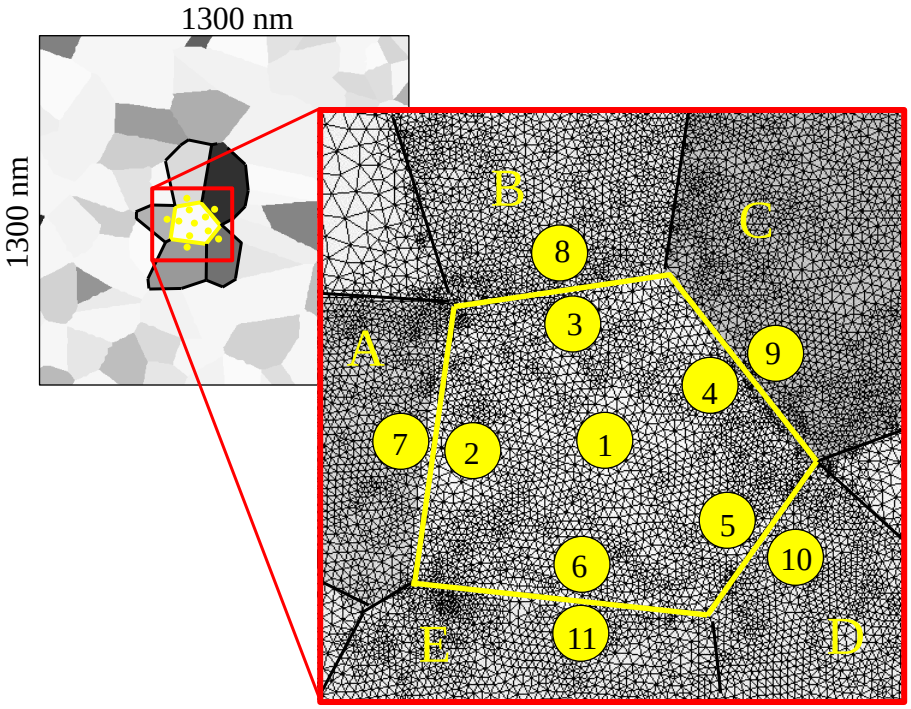

Figure 3.4.: The central region of the model microstructure showing the mesh refinement in the central grain and surrounding grains (labeled A-E) and the areas (yellow circles) for location of the virtual probe.

3.4 Results and Discussion

Simulations demonstrate that for thin continuous films the induced thermal (processing) stresses generate a spatial distribution of built-in electric fields via the direct piezoelectric effect in the cellular solid. As shown in Figure 3.5. The top row illustrates that the largest magnitude for built-in electric fields occurs in the largest samples with random orientations. In the absence of edge effects, stress and built-in electric fields reach their highest values at grain corners and boundaries where the discontinuity of the material properties induce localized stresses which in turn induce skewed local hysteretic behavior, local polarization enhancement, and suppression [109]. It is important to note that grain boundary corners, especially those which form acute angles, are locations where large stress gradients develop. These locations further contribute to the large built-in electric field values observed in acute corners

and locations where three or four grains meet. The anisotropy of the thermal expansion tensor induces in-plane stress concentrations at grain boundaries which via the direct piezoelectric effect induces polarization changes. The induced changes in polarization lead to deviations in stress via the converse piezoelectric effect. However, the effects described above are relaxed when mesa edge effects are taken into consideration. Here, in-plane stresses asymptotically approach zero as the macroscopic size of the sample decreases and the mesa has the opportunity to relieve mechanically the accumulated elastic energy through the stress-free edges of the film. As previously described in Chapter 2, these effects become less dominant for even larger sizes of highly textured samples, i.e., mesas with high multiple random distributions (MRD) [186]. The simulations performed here also demonstrate that for the utilized material parameters and the size of the experimental mesas (1 micron by 1 micron), the built-in in-plane electrical fields approach zero and so do not appear to be a dominant mechanism for domain reversal as observed in the experiments performed by Wicks et al. [176].

The microstructure shown in Figure 3.4 was used to evaluate the built-in electric field for a central grain and surrounding grains. Results for the central grains are shown in Figures 3.6 and 3.7. The locations used for application of the electric field are identifiable because the image was captured very early in the polarization switching cycle after an initial value of external electric field had been applied. The only difference between the conditions shown in Figure 3.6 and Figure 3.7 is the orientation of the central grain. In Figure 3.6 the c-axis of the central grain is aligned with the laboratory z-axis. In Figure 3.7 the c-axis of the central grain is oriented 45° away from the z-axis. As these images show, changing the orientation of the central grain influences the built-in field in the central grain, but also in the adjacent grains. The built-in electric fields also influence the initial z-direction polarization state as shown in Figures 3.8 and 3.9. Again, for Figure 3.8 the c-axis of the central grain is aligned with the laboratory z-axis, while the central grain in Figure 3.9 is oriented 45° away from the z-axis. The central grain in Figure 3.8 is nearly neutral and has a single

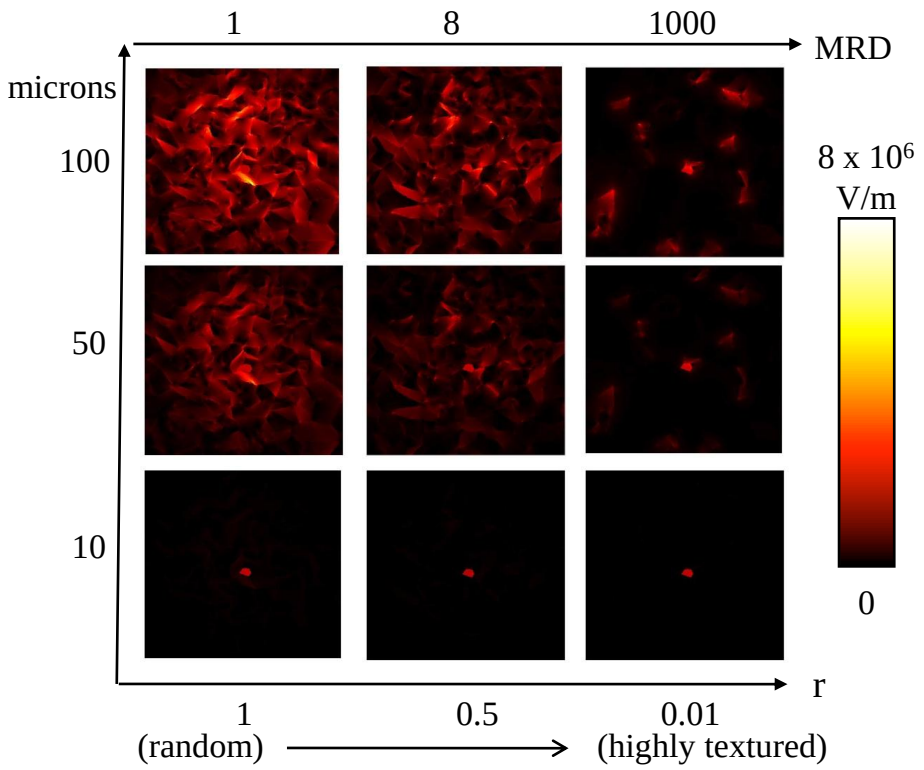

Figure 3.5.: Built-in electric field in polycrystalline ferroelectric as a function of mesa size and crystallographic texture. Note that as texture decreases (crystallographic randomness, i. e., MRD > 1) or the size of the mesa decreases to 10 microns by 10 microns, the built-in electric fields approach zero. (Image from [176])

polarization domain, while the central grain in Figure 3.9 has a negative polarization overall, but shows a positive polarization in the upper left-hand edge near the grain boundaries of two adjacent grains.

The z-direction strain data from the simulations provided further information about the local and grain-grain effects. The results confirm that the local strain is greatly dependent on the film texture. As described in Chapter 2 for a highly textured (001) PZT thin film, the overall strain is tensile (6.07×10^{-4} m/m). Although the overall strain for a randomly textured polycrystalline PZT thin film is still tensile (5.08×10^{-4} m/m), the overall strain is smaller and there are both compressive and

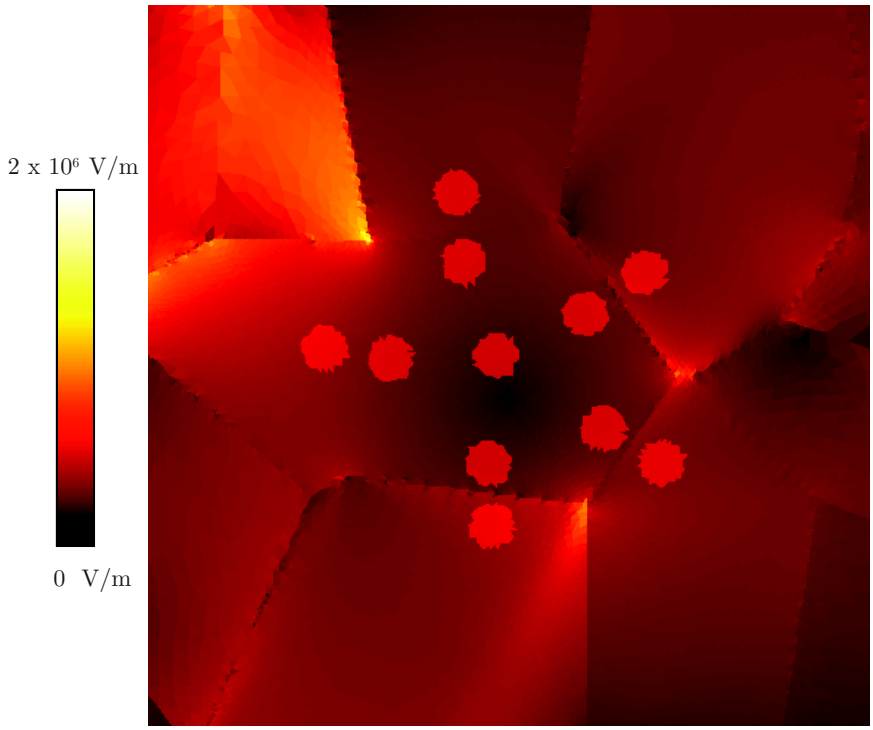

Figure 3.6.: The built-in electric field for the model microstructure shows the areas for applied field and measured polarization with the center grain c-axis aligned with the laboratory z-axis. The magnitude of the built-in electric field varies even within grains. The grain boundary between the central grain and position 9 exhibits a higher built-in field than either grain.

tensile strains that depend on the local microstructure and grain-to-grain interactions. These spatially varying strains can induce built-in electric fields as large as 20 kV/m. Even though this number is well below the typical coercive field of 2 Mv/m for PZT, it is large enough to modify the shape of the switching loops. The simulation results also confirm that the strain can vary significantly within an individual grain. Polarization hysteresis loops for three locations within the central grain of an untextured film were modeled as shown in Figure 3.10. All three loops are for locations within the central grain, but positions 2 and 3 are adjacent to grain boundaries with grain-grain misorientation. The local z-direction strain variation modeled for the as-deposited film with no applied external field is: 6.045×10^{-4} m/m at position 1, $6.941 \times$

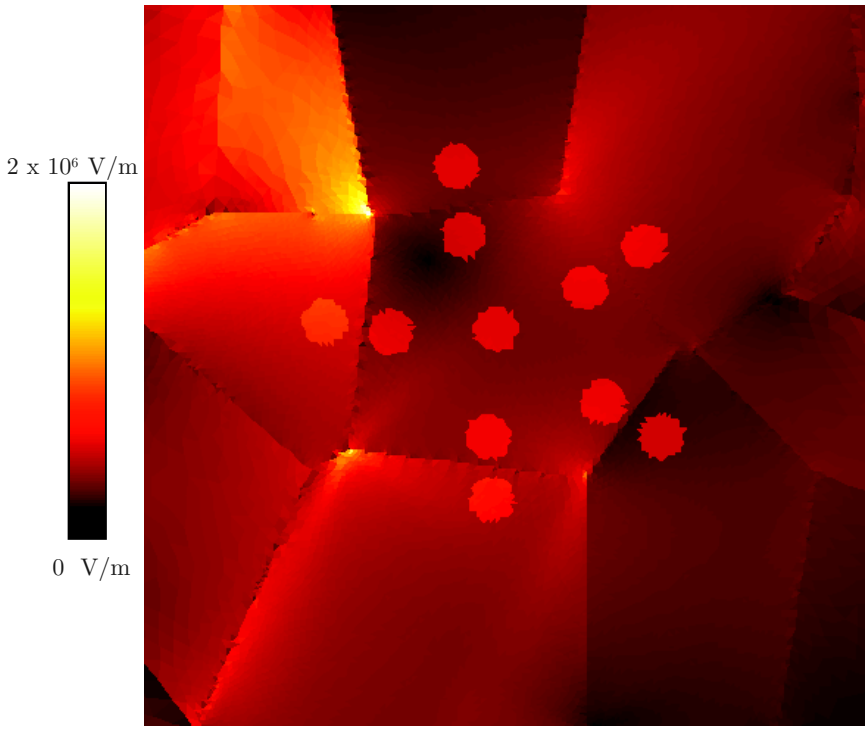

Figure 3.7.: The built-in electric field for the model microstructure shows the areas for applied field and measured polarization with the center grain c-axis tilted 45° away from the laboratory z-axis. The central grain shows an overall built-in field larger than for the model where the central grain is aligned with the laboratory z-axis. The areas of highest electric field are at grain intersections where the peak value is approximately 1.5×10^6 V/m.

10^{-4} m/m at position 2, and 5.911×10^{-4} m/m at position 3. Here positive values are for tensile strain with the z-direction being the sample normal or out-of-plane direction. Higher tensile strains cause the double well potential energy barrier to increase through the effect of the electromechanical coupling, the $q_{33kl}\varepsilon^T_{kl}P^2$ term in equation 2.1. Physically, this means that areas with higher z-direction tensile strain will require larger coercive fields for polarization reversal.

Figure 3.11 shows that as the grain boundary misorientation changes (the center grain orientation rotates about the crystal a-axis), the switching at locations near the grain boundary changes. The local strain at the grain boundary and adjacent regions

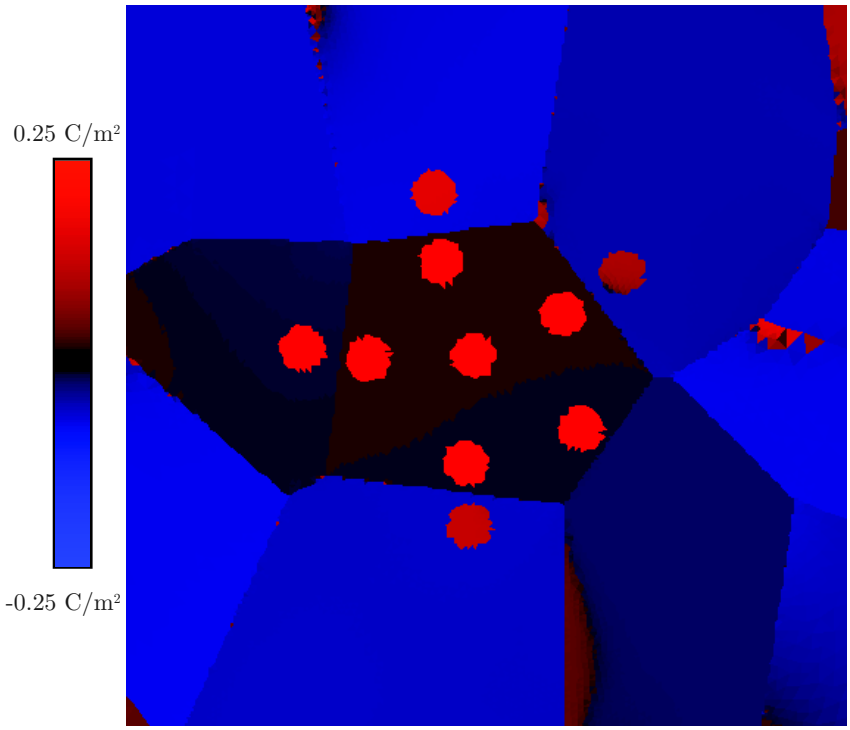

Figure 3.8.: The polarization in the z-axis for the model microstructure shows the areas for applied field and measured polarization with the center grain c-axis aligned with the laboratory z-axis. The center grain shows a neutral polarization value, and the surrounding grains are predominantly negative or neutral. Probe position 9 shows a lower polarization value than the locations in the central grain.

change accordingly. The simulation shows an increase of initial (no applied field) Z-direction tensile strain from 5.924×10^{-4} m/m to 6.001×10^{-4} m/m at position 8, and a decrease of the tensile strain from 4.842×10^{-4} m/m to 4.640×10^{-4} m/m at position 9 as the center grain is rotated from 0° to 45° about the a-axis. The rotation causes increased tensile strain at position 8 and a larger coercive field thus a wider loop, while the decreased local tensile strain at position 9 leads to a narrower loop as the center is rotated. The simulations agree with experimental results. As the misorientation angle changes, one grain becomes easier to switch, another becomes harder to switch. Furthermore, when grains are misoriented by approximately 90°, as in position 8, the coercive field value increases. When the c-axes of the grains

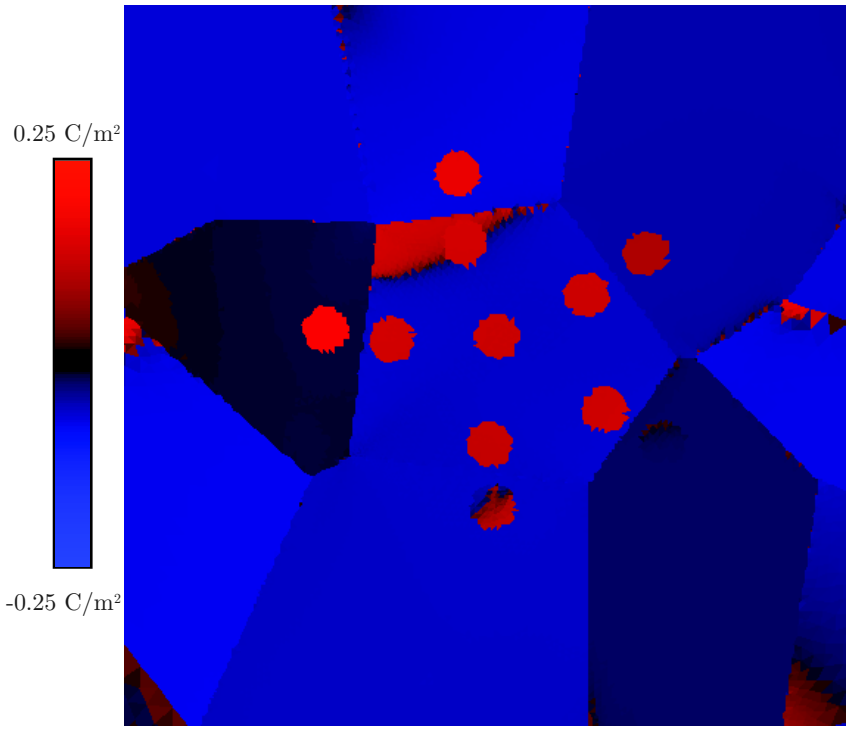

Figure 3.9.: The polarization in the z-axis direction for the model microstructure shows the areas for applied field and measured polarization with the center grain c-axis tilted 45 degrees away from the laboratory z-axis. The central grain has a region of positive polarization, with the remainder of the grain showing negative polarization.

are nearly coincident, the strains resulting from the applied electric field are also coincident and the required coercive field value decreases.

Simulations were also performed with an external electric field applied only to the six virtual probe locations in the central grain, as shown in Figure 3.4 while the five probe locations in the adjacent grains were monitored for polarization and strain changes. No changes were measured in the locations outside the central grain. In addition, only the probe locations in the central grain showed polarization switching. This result indicates that the microstructural modeling was able to capture built-in electrical field and strain effects on polarization switching behavior, but was not sensitive to possible local coupling effects between different domains within grains or between adjacent grains.

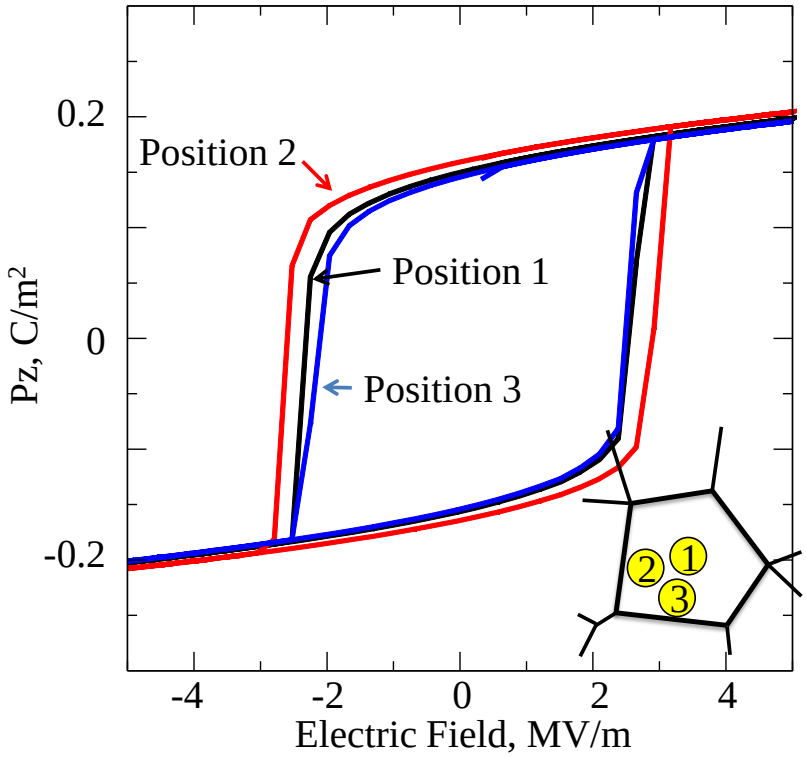

Figure 3.10.: Polarization hysteresis loops for three locations in the central grain from the simulation of ferroelectric switching. The center grain is oriented with the c-axis rotated 45 ° about the a-axis, and the overall polycrystalline thin film is untextured. Virtual Piezoforce Microscopy was done at the locations shown and changes in the loop width are clearly evident. The coercive field for position 2 is approximately 300 kV/m higher than for position 1. The coercive field for position 3 is approximately 200 kV/m lower than for position 1. The changes in coercive field correspond to the local changes Z-direction strain. The strain is tensile for all 3 locations. The strain values are: 6.045×10^{-4} m/m at position 1, 6.941×10^{-4} m/m at position 2, and 5.911×10^{-4} m/m at position 3.

3.5 Summary and Conclusions

Microstructural modeling results confirm the significance of grain-grain interactions in determining the ferroelectric domain switching hysteresis behavior of regions within individual grains. Compared to the center of a grain where the effect of the grain boundaries is minimal, regions adjacent to a grain boundary are influenced by

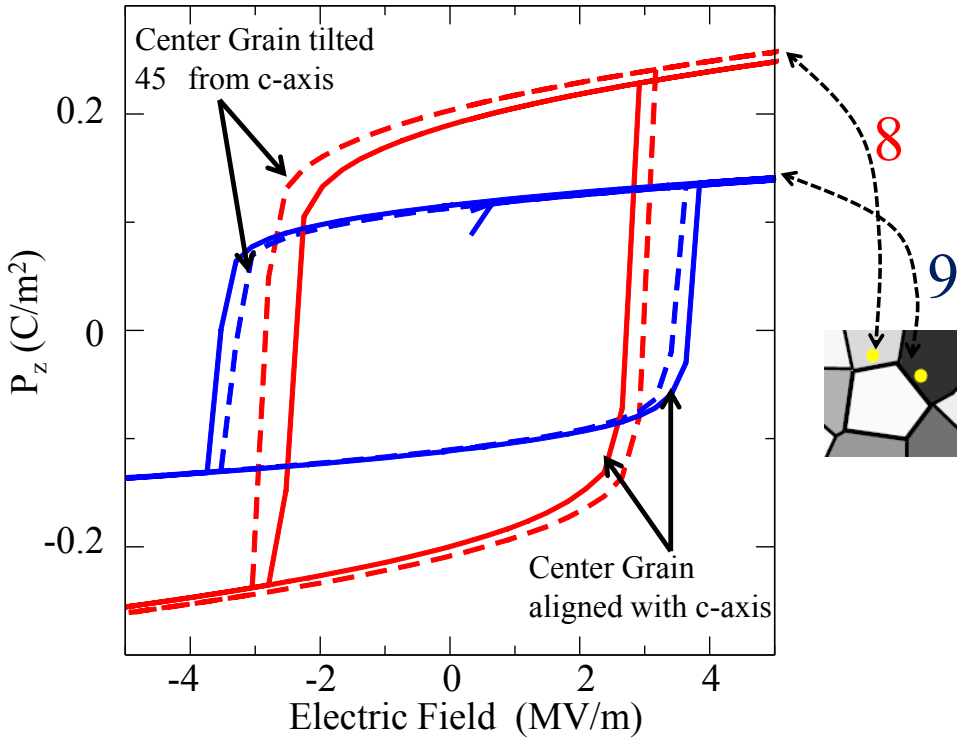

Figure 3.11.: Polarization hysteresis loops from the first switching cycle for the untextured sample simulation. The solid lines are for positions 8 and 9 where the center grain has the c-axis in the normal direction. The dashed lines are for the same two positions when the center grain is oriented with the c-axis rotated 45° about the a-axis. For the rotation, the simulation calculates an increase of initial (no applied field) z-direction tensile strain from 5.924×10^{-4} m/m to 6.001×10^{-4} m/m at position 8, and a decrease of the tensile strain from 4.842×10^{-4} m/m to 4.640×10^{-4} m/m at position 9. The increased tensile strain at position 8 leads to a larger coercive field, while the decreased local tensile strain at position 9 leads to a smaller coercive field.

the grain boundary configuration. Grain boundaries with different misorientation angles exhibit different local strain fields that couple to the local electric field via the piezoelectric effect and change the switching behavior of adjacent regions.

For grains of approximately 100 nm in diameter, the coercive field difference between a position near a grain boundary and the grain center can be as large as +300 or −200 kV/m. The coercive field differences correlate with changes in the tensile

strain. These interactions merit further investigation as the overall size of ferroelectric devices continues to decrease and the read-write area required for memory storage shrinks towards the same scale as the size of the grains in a polycrystalline film.

The current chapter demonstrates that the stress state and built-in electric fields result from a combination of the epitaxial strain, overall film texture, and tertiary coupling effects from adjacent grains. Mechanical coupling between areas of different crystallographic orientation creates strain which enhances or inhibits out-of-plane polarization switching. This local coupling effect is observed in the coercive field required for polarization switching and the remnant polarization.

CHAPTER 4. SUMMARY AND FUTURE WORK

4.1 Summary

This thesis presents investigations and results on the polarization switching behavior of ferroelectric materials from the behavior of single-crystal thin films to the localized behavior of a portion of a grain in a polycrystalline thin film. Polycrystalline thin film behavior is further analyzed to understand the influence of mesa aspect ratio. Thermodynamically-based finite element modeling is used to examine the stress state and built-in electric fields and to characterize the polarization switching hysteresis behavior. Microstructural modeling captures the influence of grain orientation and sample geometry and predicts ways in which material properties and device geometries can be engineered for a particular ferroelectric response.

Chapter 2 presents the polarization hysteresis behavior of a single-crystal material as a function of stress and orientation. Results form a map which can be used to guide material production towards a particular response. The map is also useful to understand and predict the behavior of a grain in a polycrystalline thin film sample. The orientation distribution of a polycrystalline thin film is shown to determine whether the average stress state of the film will be tensile or compressive. The geometry of the film is also shown to influence the magnitude of these built-in stresses. The out-of-plane polarization hysteresis response of a single grain will be influenced by in-plane stresses and by the orientation of the grain. Polarization switching of (001)-oriented grains has less variation when the grain is embedded in a mesa with a large aspect ratio due to local stress relaxation. This stress relaxation creates a corresponding decrease in the localized built-in electric fields. This creates less sample-to-sample variation for a group of simulations with the same overall texture but different local conditions surrounding the central, switched grain. The remnant

polarization of piezoelectric (111)-oriented grains is enhanced from an average value of about 0.2 C/m^2 for low aspect ratio films to more than 0.35 C/m^2 for for large aspect ratios.

Chapter 3 explores local stress and polarization results within grains of a polycrystalline material and adjacent to grain boundaries. The microstructural model shows the influence of grain-to-grain interactions on the stress state, built-in electric field, and polarization hysteresis of individual grains. This chapter also explains the contribution of local strains which either enhance or inhibit hysteresis behavior. THis depends upon proximity to the grain boundaries, the orientation of the grain to adjacent grains, and the orientation of the grain with respect to the geometry of the thin film. The modeling results show that the strains and built-in electric fields that result from local misorientation or polarization switching are not sufficient to cause back-switching of a grain or a region within a grain. For grains of approximately 100 nm in diameter, the coercive field difference between a location near a grain boundary and the grain center can be as large as + 12% or - 8%. Adjacent grains are affected through coupling to the orientation difference across the grain boundary. Rotation of the center grain from 0° to 45° about the a-axis causes an increase of initial (no applied field) z-direction tensile strain from 5.924×10^{-4} m/m to 6.001×10^{-4} m/m in one adjacent grain and a decrease of the tensile strain from 4.842×10^{-4} m/m to 4.640×10^{-4} m/m in another adjacent grain. The rotation causes increased tensile strain and a larger coercive field in the first adjacent grain, while the decreased local tensile strain in the second adjacent grain leads to a narrower loop. The simulations agree with experimental results: as the misorientation angle changes, one grain becomes easier to switch, another becomes harder to switch. Furthermore, when grains are misoriented by approximately 90° the coercive field value increases. When the c-axes of the grains are nearly coincident, the strains resulting from the applied electric field are also coincident and the required coercive field value decreases.

The results presented demonstrate that these modeling methods can produce results which are useful in engineering particular desired polarization switching be-

havior. The analytical methods are predictive for polarization switching behavior of single-crystal material, and the computational models can incorporate the effects of orientation and device geometry for polycrystalline thin films.

4.2 Future Work

The properties of lead-free materials show significant promise for useful polarization switching behavior. The analytical and computational methods used for PZT could be adapted to other materials by using appropriate material parameters. Alloys of Barium-Zirconate-Titanate (BZT) and Barium-Calcinate-Titanate (BCT) have both a rhombohedral structure and a tetragonal structure below the Curie temperature of 367 K. A phase diagram proposed by Liu et al. [187] for BZT-BCT shown in Figure 4.1 shows that for a range of compositions both rhombohedral and tetragonal structures are present. Combining these materials at a 50/50 ratio creates a morphotropic phase boundary (MPB) very near room temperature, at approximately 297 K. The MPB enhances the piezoelectric behavior that yields a remnant polarization value as high as 0.022 C/m^2 [188]. This is lower than PZT, but promising for a lead-free material. Experimental results from Xue et al. [189], Yao et al. [190] and Ehmke [191] for the 50/50 ratio, as shown in Figure 4.2 document discontinuities in physical properties. Xue et al. [189] determined that the temperature for the rhombohedral to tetragonal phase transformation occurs at 302.5 K for heating and at 293.5 K for cooling from the tetragonal to the rhombohedral phase. Based on this 9° difference they characterize the phase transition as first order.

Several authors have reported a strong temperature-dependence of the electrical properties, and have reported a corresponding change in polarization hysteresis for BZT-BCT or other lead-free materials [187,190–194]. Gao et al. propose that the enhanced piezoelectricity at the MPB results from the formation of nano-sized domains which are more easily switched than larger domains [195]. Enhanced piezoelectric properties have also been established for materials poled during cooling from above the Tc. An internal bias field develops from redistribution of defect charge carriers rather

than from a significant change in ferroelectric domain texture [196]. Xue et al [189] suggest that instabilities occur along multiple orientations in the MPB which is the source of high piezoelectric constants. Damjanovic et al. support this explanation and also propose, based on Raman spectroscopy, that an additional phase transition occurs at 213 K [197]. They also observe that the lack of frequency-dependence suggests that the characteristics of the MPB are probably not related to the interaction of domain walls with defects. Tutuncu et al. [198] used x-ray diffraction to demonstrate increased 90° domain wall motion leading to enhanced piezoelectric coefficients.

Following a parameter fitting method developed by Zizhao Zhao [199], Landau coefficients have been fitted to experimental data. This result provides support for the theory proposed by Xue, et al. [189] that the MPB can be understood as a first-order transition with a latent heat of transformation and a discontinuous change in enthalpy.

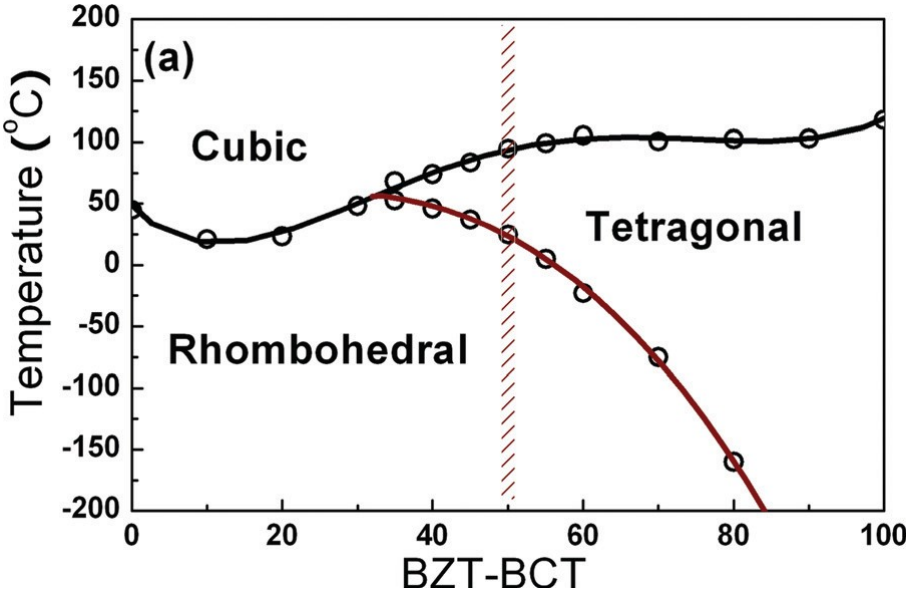

Figure 4.1.: Phase diagram for BZT-50BCT. As the temperature rises from -50 deg. C (223 K) to 120 deg. C (393 K) the phase changes from rhombohedral to tetragonal to cubic. (Image from [189])

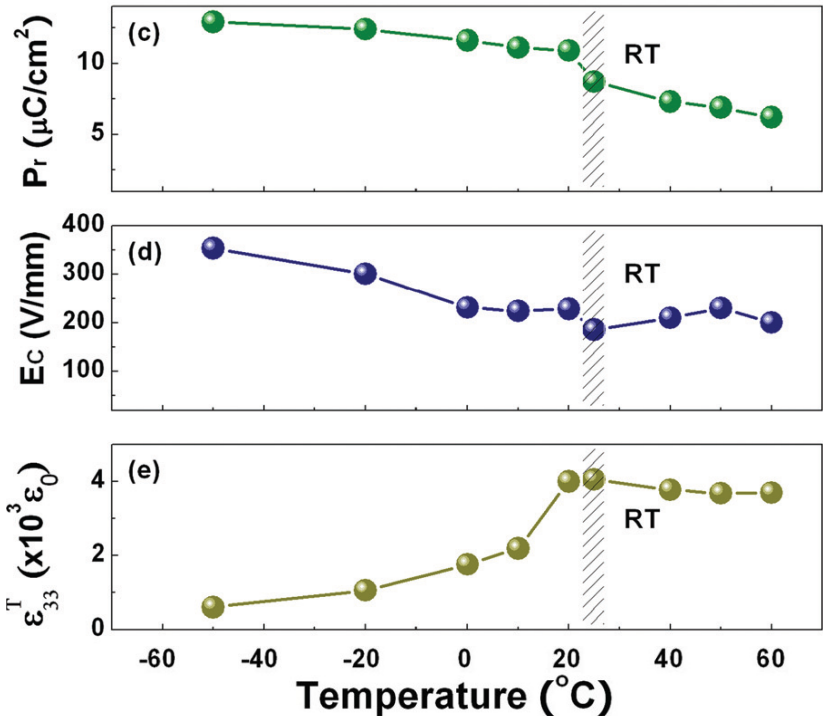

Figure 4.2.: The remnant polarization, coercive field value, and permittivity change with temperature. (Image from [189])

By fitting the Landau coefficients to the polarization hysteresis loops above and below the transformation from rhombohedral to tetragonal the general Taylor expansion can be rewritten to include temperature dependence. For a stress-free solid at equilibrium, where $\delta F/\delta P = 0$, the first four terms of equation 2.1 are arranged so that:

$$E = aP + bP^3 + cP^5 \tag{4.1}$$

where: $a = \alpha(T - Tc)$.

Values for remnant polarization, maximum polarization, coercive field, permittivity, and mobility were extracted from experimentally measured polarization hysteresis loops by digitizing published loops [189, 190] or directly from digital data files [200]. The extracted experimental values were used as inputs to determine Lan-

dau coefficients. The method and equations developed by Zhao for fitting the Landau coefficients from the polarization hysteresis loop parameters are summarized in Appendix B. Determining the coefficients was an iterative process. The fitted coefficients were used to generate polarization hysteresis loops which were compared to the original experimental polarization hysteresis loops to determine closeness of fit. The fitted loops were generated with a sinusoidal electric field at a frequency of 0.1 Hz and a time step of 0.005 seconds. The maximum applied electric field was the same as the experimental data, either 2MV/m (Xue data) or 1MV/m (Yao and Ehmke data). Permittivity, mobility, and coercive field were adjusted at each temperature to arrive at an optimized correlation of the polarization hysteresis to the experimental results. Values for the three Landau coefficients, α, b, and c, were established at each temperature and then analyzed to generate a temperature-dependent equation for each coefficient, excluding the data very near the MPB. In order to maintain the character of a first order ferroelectric transition, the α and c coefficients were positive values, while the b coefficient was negative. The temperature-dependent equations for the Landau coefficients were combined and used with the first four terms of equation 2.1 to calculate the free energy density as a function of polarization for temperatures below and above the MPB.

Figure 4.3 shows the experimental remnant polarization data extracted from the hysteresis loops. These data are also included as Table B.1 in Appendix B. The blue circles show values extracted from data published by Xue, et al. [189] and the red circles show values extracted from data provided by Ehmke [191]. Fitted polarization hysteresis loops were generated for the entire temperature range of the experimental data from 223 K to 353 K as part of the iterative process for determining Landau coefficients. Figure 4.4 is an example of the experimental polarization hysteresis loop plotted with the fitted loop. The fitted loop does not capture the lower part of the hysteresis loop for positive coercive field because the energy equation does not include the effects of orientation distribution, 90° switching, grain boundaries, domain pinning, or other non-uniform states. The upper and lower portions of the fitted

hysteresis loop, as well as the fitted value for coercive field, were used to characterize the fit of the Landau parameters.

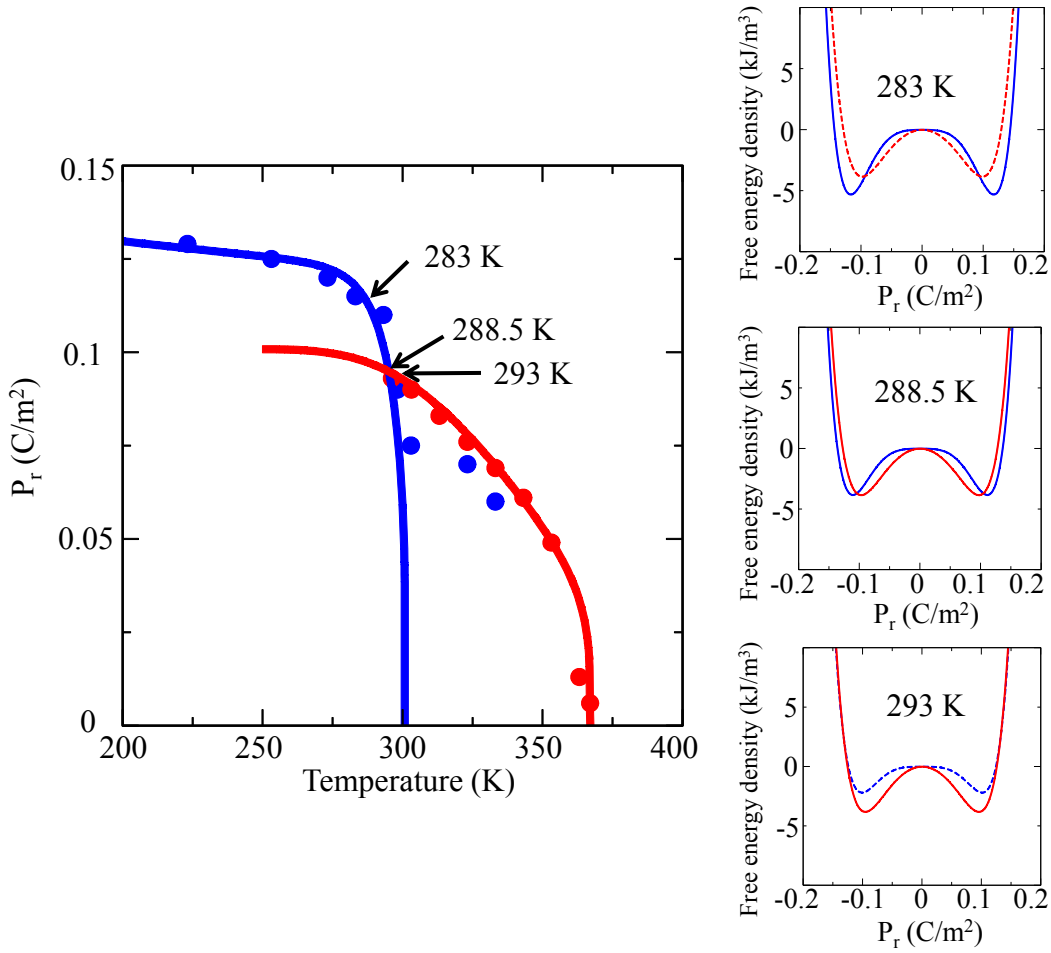

Figure 4.3.: Remnant polarization values for experimental data and parameter fitting. Results from Xue [189] are shown as blue circles and results from Ehmke [191] are shown as red circles. The fitted values for remnant polarization are shown as two curves. Temperature-dependent Landau coefficients for the fitted equations were determined for two ranges of behavior, below and above the MPB. Insets show free energy density vs. remnant polarization values at 283 K, 288.5 K and 293 K using the fitted parameters. The blue curves are from the rhombohedral phase, and the red lines are for the tetrahedral phase. Between 283 K and 293 K the free energy minimum shifts from the rhombohedral to the tetragonal phase. At 288.5 K the minima for the rhombohedral and tetragonal phase are equal, but occur at polarization values of $\pm$ 0.136 C/m^2 for the rhombohedral phase and $\pm$ 0.127 C/m^2 for the tetrahedral phase.

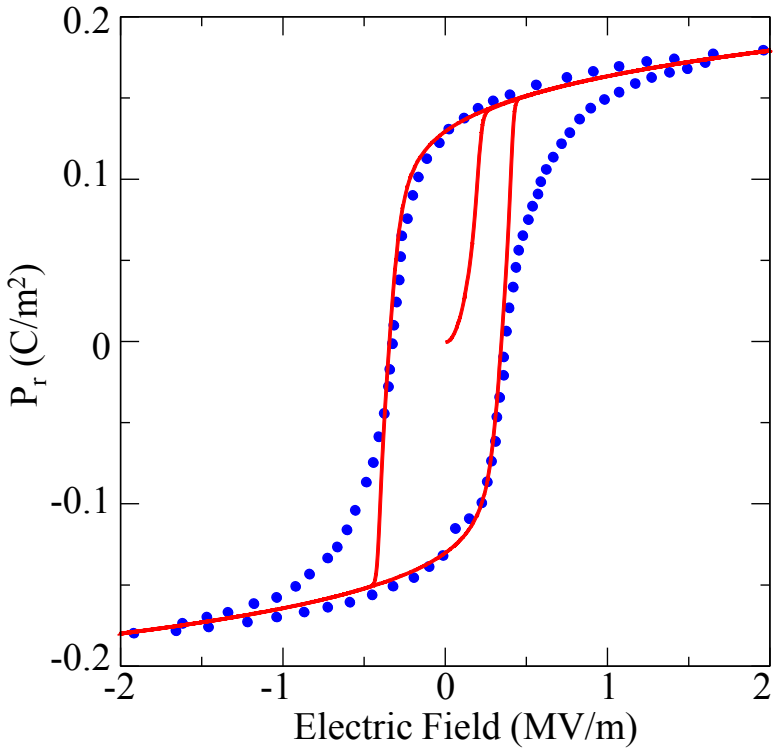

Figure 4.4.: Polarization hysteresis loops for 223 K. Experimental results [189] are shown as blue dots and the fitted result is shown as a dashed red line. The difference between the fitted and the experimental data results from not including the effects of orientation distribution, 90° switching, grain boundaries, domain pinning, or other non-uniform states. The upper and lower portions of the fitted hysteresis loop, as well as the fitted value for coercive field, were used to characterize the fit of the Landau parameters.

The BZT-BCT system reveals several opportunities for further research: these free energy equations could be used in microstructural modeling to elucidate the polarization switching behavior as a function of temperature and composition, particularly through the MPB. BZT-20BCT has only rhombohedral and cubic phases, BZT-60BCT has a larger range of temperature for the tetragonal phase, and BZT-85BCT has only tetragonal and cubic phases. Modeling of the BZT-BCT system could be performed by assigning the properties of the two constituent materials to the grains in a polycrystalline film. The microstructural modeling tools would need to be modified to accomodate two different Curie temperatures in order to capture accurately the stresses resulting from cooling to room temperature. The polarization switching hysteresis could be studied as an average over several grains, for individual grains, or for regions within grains. This modeling would provide insight into the stress states and built-in electric fields developed at the MPB and might be useful to predict optimal microstructures and device geometries.

The addition of 90° switching to the computational modeling tools by extending the OOF functionality would improve the physical accuracy of the models and potentially allow better correlation between model and experimental results. From the free energy density expression shown as Equation 1.2 it can be seen that extending the model will require the addition of free energy terms which include an energy penalty for polarization directions away from the crystallographically allowed variants.

LIST OF REFERENCES

LIST OF REFERENCES

[1] R. W. Whatmore, Q. Zhang, Z. Huang, and R. A. Dorey. Ferroelectric thin and thick films for microsystems. *Materials Science in Semiconductor Processing*, 5:65–76, 2003.

[2] R. Waser and A. Rudiger. Pushing towards the digital storage limit. *Nature Materials*, 3(81-82), 2004.

[3] N. Setter, D. Damjanovic, L. Eng, G. Fox, S. Gevorgian, Hong. S., A. Kingon, H. Kohlstedt, Park N. Y., G. B. Stephenson, I. Stolitchnov, A. K. Taganstev, D. V. Taylor, T. Yamada, and S. Streiffer. Ferroelectric thin films: Review of materials, properties, and applications. *Journal of Applied Physics*, 100(051606), 2006.

[4] J. F. Scott. Applications of modern ferroelectrics. *Science*, 315:954–959, 2007.

[5] A. J. Bell. Ferroelectrics: The role of ceramic science and engineering. *Journal of the European Ceramic Society*, 28:1307–1317, 2008.

[6] K. Parkhi. Semiconductor memory: Technologies and global markets. Technical Report IFT072A, BCC Market Research, 2014.

[7] K. J. Choi, M. Biegalski, Y. L. Li, A. Sharan, J. Schubert, R. Uecker, P. Reiche, Y. B. Chen, X. Q. Pan, V. Gopalan, L.-Q. Chen, D. G. Schlom, and C. B. Eom. Enhancement of ferroelectricity in strained $BaTiO_3$ thin films. *Science*, 306:1005–1009, 2004.

[8] C. Ederer and N. A. Spaldin. Effect of epitaxial strain on the spontaneous polarization of thin film ferroelectrics. *Physical Review Letters*, 95(257601), 2005.

[9] K. M. Rabe. Theoretical investigations of epitaxial strain effects in ferroelectric oxide thin films and superlattices. *Current Opinion in Solid State and Materials Science*, 9:122–127, 2005.

[10] J. Wang, Y. Li, L. Q. Chen, and T. Y. Zhang. The effect of mechanical strains on the ferroelectric and dielectric properties of a model single crystal: Phase field simulation. *Acta Materialia*, 53:2495–2507, 2006.

[11] J. Kreisel, B. Noheda, and B. Dkhil. Phase transitions and ferroelectrics: Revival and the future in the field. *Phase Transitions*, 82(9):633–661, 2009.

[12] K. Uchino. *Ferroelectric Devices*. CRC Press, 2010.

[13] U. Waghmare, M. H. G. Sluiter, T. Kimura, T. Goto, and Y. Kawazoe. A lead-free high-T_C ferroelectric $BaTi_2O_5$: A first-principles study. *Applied Physics Letters*, 84(24), 2004.

[14] C. J. Fennie and K. M. Rabe. First-principles investigation of ferroelectricity in epitaxially strained Pb_2TiO_4. *Physical Review B*, 71:100102, 2005.

[15] Y. L. Li, L. E. Cross, and L. Q. Chen. A phenomenological thermodynamic potential for $BaTiO_3$ single crystals. *Journal of Applied Physics*, 98:064101, 2005.

[16] Y. L. Li and L. Q. Chen. Temperature-strain phase diagram for $BaTiO_3$ thin films. *Applied Physics Letters*, 88:072905, 2006.

[17] Y. L. Li, S. Choudhury, J. H. Haeni, M. D. Biegalski, A. Vasudevarao, A. Sharan, H. Z. Ma, J. Levy, V. Gopalan, S. Trolier-McKinstry, D. G. Scholm, Q. X. Jia, and L. Q. Chen. Phase transition and domain structures in strained pseudocubic (100) $SrTiO_3$ thin films. *Physics Review B*, 73:184112, 2006.

[18] M. E. Lines and A. M. Glass. *Principles and Applications of Ferroelectrics and Related Materials*. Clarendon Press, Oxford, 1977.

[19] F. Jona and G. Shirane. *Ferroelectric Crystals*. Pergamon Press, MacMillan Company, New York, 1962.

[20] A. Sheikholeslami and P. G. Gulak. A survey of circuit innovations in ferroelectric random-access memories. *Proceedings of the IEEE*, 88(5):667–689, 2000.

[21] S. V. Kalinin, A. N. Morozovska, L. Q. Chen, and B. J. Rodriguez. Local polarization dynamics in ferroelectric materials. *Reports on Progress in Physics*, 73:056502, 2010.

[22] R. E. Cohen. Theory of ferroelectrics: A vision for the next decade and beyond. *Journal of Physics and Chemistry of Solids*, 61:139–146, 2000.

[23] B. Meyer and D. Vanderbilt. Ab initio study of ferroelectric domain walls in $PbTiO_3$. *Physical Review B*, 65, 2002.

[24] O. Diéguez and D. Vanderbilt. First-principles calculations for insulators at constant polarization. *Physical Review Letters*, 96:056401, 2006.

[25] O. Diéguez and D. Vanderbilt. Theoretical study of ferroelectric potassium nitrate. *Physical Review B*, 76, 2007.

[26] J. Paul, T. Nishamatsu, Y. Kawazoe, and U. Waghmare. Polarization rotation, switching, and electric-field-temperature phase diagrams of ferroelectric $BaTiO_3$. *Physical Review B*, 80:024107, 2009.

[27] S. J. Ahmed, S. Pichardo, L. Curiel, and O. Rubel. First-principle modelling of the ferroelectric switching in $BaTiO_3$: Concurrent switching versus domain wall motion. *Modelling and Simulation in Materials Science and Engineering*, 22:055014, 2014.

[28] Y. H. Shin, I. Grinberg, I. W. Chen, and A. M. Rappe. Nucleation and growth mechanism of ferroelectric domain-wall motion. *Nature*, 2007.

[29] A. Chandrasekaran, D. Damjanovic, N. Setter, and N. Marzari. Defect ordering and defect-domain-wall interactions in $PbTiO_3$: A first-principles study. *Physical Review B*, 88:214116, 2013.

[30] P. Marton and C. Elsässer. First-principles study of structural and elastic properties of the tetragonal ferroelectric perovskite $Pb(Zr_{0.50}Ti_{0.50})O_3$. *Physica Status Solidi B*, 248(10):2222–2228, 2011.

[31] A. Kubo, J. M. Albina, and Y. Umeno. Atomistic study of stress-induced switching of 90° ferroelectric domain walls in $PbTiO_3$: Size, temperature and structural effect. *Modelling and Simulation in Materials Science and Engineering*, 21:065019, 2013.

[32] R. E. García, W. C. Carter, and S. A. Langer. The effect of texture on the macroscopic properties of polycrystalline piezoelectrics: Applications to barium titanate and PZN-PT. *Journal of the American Ceramic Society*, 88(3):750–757, 2005.

[33] J. W. S. Rayleigh. On the influence of obstacles arranged in rectangular order upon the properties of a medium. *Philosophical Magazine*, 34:481–502, 1892.

[34] J. E. Eshelby. The determination of the field of an ellipsoidal inclusion and related problems. *Proceedings of the Royal Society of London A*, 241:376–396, 1957.

[35] R. Hill. A self-consistent mechanics of composite materials. *Journal of the Mechanics and Physics of Solids*, 13:213–222, 1965.

[36] B. Budiansky. On the elastic moduli of some heterogeneous materials. *Journal of the Mechanics and Physics of Solids*, 13:223–227, 1965.

[37] Z. Hashin. Analysis of composite materials. *Journal of Applied Mechanics*, 50:481–505, 1983.

[38] W. F. J. Deeg. *The analysis of dislocation, crack, and inclusion problems in piezoelectric solids.* PhD thesis, Stanford University, 1980.

[39] M. Marutake. A calculation of physical constants of ceramic barium titanate. *Journal of the Physical Society of Japan*, 11(8):807–814, 1956.

[40] N. A. Pertsev, A. G. Zembilgotov, and R. Waser. Aggregate linear properties of ferroelectric ceramics and polycrystalline thin films: Calculation by the method of effective piezoelectric medium. *Journal of Applied Physics*, 84(3):1524–1529, 1998.

[41] N. A. Pertsev, A. G. Zembilgotov, and R. Waser. Effective dielectric and piezoelectric constants of thin polycrystalline ferroelectric films. *Physics of the Solid State*, 40(12):2002–2008, 1998.

[42] S. Hwang, J. E. Huber, R. E. McMeeking, and N. A. Fleck. The simulation of switching in polycrystalline ferroelectric ceramics. *Journal of Applied Physics*, 84(3):1530–1540, 1998.

[43] W. Kreher and J. Rodel. Ferroelectric ceramics and composites: Statistical models for effective piezoelectric and pyroelectric properties. In *Applications of Ferroelectrics, 1998, IASF 98, Proceedings of the Eleventh IEEE International Symposium of Ferroelectrics*, pages 455–458, 1998.

[44] T. Olson and M. Avellaneda. Effective dielectric and elastic constants of piezoelectric polycrystals. *Journal of Applied Physics*, 71(9):4455–4464, 1992.

[45] M. L. Dunn. Effects of grain shape anisotropy, porosity, and microcracks on the elastic and dielectric constants of polycrystalline piezoelectric ceramics. *Journal of Applied Physics*, 78(3):1533–1541, 1995.

[46] V. Aleshin. Properties of anisotropic piezoactive polycrystals. *Journal of Applied Physics*, 88(6):3587–3591, 2000.

[47] J. Y. Li. The effective electroelastic moduli of textured piezoelectric polycrystalline aggregates. *Journal of the Mechanics and Physics of Solids*, 48:529–552, 2000.

[48] C. W. Nan and D. R. Clarke. Effective properties of ferroelectric and/or ferromagnetic composites: A unified approach and its applications. *Journal of the American Ceramics Society*, 80:1333–1340, 1997.

[49] L. Huang and H. F. Tiersten. Electroelastic equations describing slow hysteresis in polarized ferroelectric ceramic plates. *Journal of Applied Physics*, 83(11):6126–6139, 1998.

[50] G. H. Haertling. Ferroelectric ceramics: History and technology. *Journal of the American Ceramic Society*, 82(4):797–818, 1999.

[51] M. Kamlah. Ferroelectric and ferroeleastic piezoceramics-modeling of electromechanical hysteresis phenomena. *Continuum Mechanics and Thermodynamics*, 13(4):219–268, 2001.

[52] D. Bolten, U. Böttger, and R. Waser. Reversible and irreversible piezoelectric and ferroelectric response in ferroelectric ceramics and thin films. *Journal of the European Ceramic Society*, 24:725–732, 2004.

[53] M. Kamlah and C. Tsakmakis. Phenomenological modeling of the non-linear electromechanical coupling in ferroelectrics. *International Journal of Solids and Structures*, 36:669–695, 1999.

[54] M. Kamlah and U. Böhle. Finite element analysis of piezoceramic components taking into account ferroelectric hysteresis behavior. *International Journal of Solids and Structures*, 38:605–633, 2001.

[55] J. W. P. Schmelzer, editor. *Nucleation Theory and Applications*, chapter 6, pages 178–214. Wiley-VCH, 2004.

[56] V. Shur. Switching kinetics in normal and relaxor ferroelectrics: PZT thin films and PLZT ceramics. In *Proceedings of the 10th ISAF*, pages 233–240. IEEE, 1996.

[57] V. Shur, E. Rumyantsev, R. Batchko, G. Miller, M. Fejer, and R. Byer. Physical basis of the domain engineering in the bulk ferroelectrics. *Ferroelectrics*, 221:157–167, 1999.

[58] V. Y. Shur, E. L. Rumayantsev, E. V. Nikolaeva, E. I. Shishkin, and I. S. Baturin. Kinetic approach to fatigue phenomenon in ferroelectrics. *Journal of Applied Physics*, 90(12):6312–6315, 2001.

[59] V. Shur, E. Rumyantsev, E. Nikolaeva, E. Shishkin, I. Baturin, A. Shur, D. Lupascu, C. Randall, and M. Ozgul. Fatigue effect in bulk ferroelectrics. In *Smart Structures and Materials 2002: Active Materials: Behavior and Mechanics*, volume 4699, pages 40–50, 2002.

[60] V. Shur, E. Rumyantsev, E Hikolaeva, and E. Shishkin. Fast and superfast motion of ferroelectric domain boundaries. *Integrated Ferroelectrics*, 59:1439–1503, 2003.

[61] V. Shur. Domain engineering in lithium niobate and lithium tantalate: Domain wall motion. *Ferroelectrics*, 340:3–16, 2006.

[62] V. Shur. Kinetics of ferroelectric domains: Application of general approach to $LiNbO_3$ and $LiTaO_3$. *Journal of Materials Science*, 41:199–210, 2006.

[63] A. I. Lobov, V. Shur, I. S. Baturin, E. I. Shishkin, D. K. Kuznetsov, A. G. Shur, M. S. Bolbilov, and K. Gallo. Field induced evolution of regular and random 2D domain structures and shape of isolated domains in $LiNbO_3$ and $LiTaO_3$. *Ferroelectrics*, 341(1):109–116, 2007.

[64] J. Fousek, L. E. Cross, and J. Nosek. Domain phenomena in single crystalline and ceramic ferroics: Unresolved and attractive problems. *Microelectronic Engineering*, 66:574–583, 2003.

[65] R. C. Smith and C. L. Hom. Domain wall theory for ferroelectric hysteresis. *Journal of Intelligent Material Systems and Structures*, 10(3):195–213, 1999.

[66] V. K. Kalpakides and A. I. Arvanitakis. A level set approach to domain wall kinetics and domain patterning in elastic ferroelectrics. *Computer Methods in Applied Mechanics and Engineering*, 199(45-48):2865–2875, 2010.

[67] J. E. Huber, N. A. Fleck, C. M. Landis, and R. M. McMeeking. A constitutive model for ferroelectric polycrystals. *Journal of the Mechanics and Physics of Solids*, 47:1663–1697, 1999.

[68] F. Dave and P. M. Mariano. Evolution of domain walls in ferroelectric solids. *Journal of the Mechanics and Physics of Solids*, 49:1701–1726, 2001.

[69] Y. Su and C. M. Landis. Continuum thermodynamics of ferroelectric domain evolution: Theory, finite element implementation, and application to domain wall pinning. *Journal of the Mechanics and Physics of Solids*, 55(2):280–305, 2007.

[70] S. Zhang, J. Liu, and C. Yang. Growth and characterization of PZT films with different grain sizes. *Integrated Ferroelectrics*, 84:99–105, 2006.

[71] C-T. Sun and A. Achuthan. Domain-switching criteria for ferroelectric materials subjected to electrical and mechanical loads. *Journal of the American Ceramic Society*, 87(3):395–400, 2004.

[72] M. G. Shaikh, S. Phanish, and S. M. Sivakumar. Domain switching criteria for ferroelectrics. *Computational Materials Science*, 37:178–186, 2006.

[73] F. X. Li and R. K. N. D. Rajapakse. A constrained domain-switching model for polycrystalline ferroelectric ceramics part I: Model formulation and application to tetragonal materials. *Acta Materialia*, 55:6472–6480, 2007.

[74] F. X. Li and R. K. N. D. Rajapakse. A constrained domain-switching model for polycrystalline ferroelectric ceramics part II: Combined switching and application to rhombohedral materials. *Acta Materialia*, 55:6481–6488, 2007.

[75] C. M. Landis. A new finite-element formulation for electromechanical boundary value problems. *International Journal for Numerical Methods in Engineering*, 55:613–628, 2002.

[76] C. M. Landis. Fully coupled, multi-axial, symmetric constitutive laws for polycrystalline ferroelectric ceramics. *Journal of the Mechanics and Physics of Solids*, 50(1):127–152, 2002.

[77] C. M. Landis. Energetically consistent boundary conditions for electromechanical fracture. *International Journal of Solids and Structures*, 41(22-23):6291–6315, 2004.

[78] L. Daniel, D. A. Hall, and P. J. Withers. A multiscale model for reversible ferroelectric behaviour of polycrystalline ceramics. *Mechanics of Materials*, pages 85–100, 2014.

[79] J. E. Huber. Micromechanical modelling of ferroelectrics. *Current Opinion in Solid State and Materials Science*, 9:100–106, 2005.

[80] A. Arockiarajan, S. M. Sivakumar, and C. Sansour. A thermodynamically motivated model for ferroelectric ceramics with grain boundary effects. *Smart Materials and Structures*, 19:015008, 2010.

[81] K. Jayabal, A. Menzel, A. Arockiarajan, and S. M. Srinivasan. Micromechanical modelling of switching phenomena in polycrystalline piezoceramics: Application of a polygonal finite element approach. *Computational Mechanics*, 48:421–435, 2011.

[82] N. Setter and R. Waser. Electroceramic materials. *Acta Materialia*, 48:151–178, 2000.

[83] K. Bhattacharya and G. Ravichandra. Ferroelectric perovskites for electromechanical actuation. *Acta Materialia*, 51:5941–5960, 2003.

[84] W. Zhang and K. Bhattacharya. A computation model of ferroelectric domains part I: Model formulation and domain switching. *Acta Materialia*, 53:185–198, 2005.

[85] W. Zhang and K. Bhattacharya. A computation model of ferroelectric domains part II: Grain boundaries and defect pinning. *Acta Materialia*, 53:199–209, 2005.

[86] J. Li and K. Bhattacharya. *Fundamental Physics of Ferroelectrics*, chapter : A mesoscopic electromechanical theory of ferroelectric films and ceramics. AIP, 2002.

[87] K. Dayal and K. Bhattacharya. A real-space non-local phase-field model of ferroelectric domain patterns in complex geometries. *Acta Materialia*, 55:1907–1917, 2007.

[88] A. F. Devonshire. Theory of barium titanate: Part 1. *Philosophical Magazine*, 40:1040–1063, 1949.

[89] A. F. Devonshire. Theory of barium titanate: Part 2. *Philosophical Magazine*, 42:1065–1079, 1951.

[90] A. F. Devonshire. Theory of ferroelectrics. *Advances in Physics*, 3(10):85–130, 1954.

[91] S. M. Allen and J. W. Cahn. A microphase theory for antiphase boundary motion and its application to antiphase domain coarsening. *Acta Metallurgica*, 27:1085–1095, 1979.

[92] L. D. Landau and E. M. Lifshitz. *Statistical physics*. Pergamon Press, Oxford, 1980.

[93] Y. L. Li, S. Y. Hu, Z. K. Liu, and L. Q. Chen. Effect of electrical boundary conditions on ferroelectric domain structures in thin films. *Applied Physics Letters*, 2002.

[94] K. H. Chew, Y. Ishibashi, F. G. Shin, and H. L. W. Chan. Effective Landau-Devonshire-type theory of phase transitions in ferroelectric thin films based on the Tilley-Zeks model. *Journal of the Physical Society of Japan*, 72(11):2972–2978, 2003.

[95] J. Li and G. J. Weng. A theory of domain switch for the nonlinear behaviour of ferroelectrics. *Proceedings of the Royal Society A*, 455(1989):3493–3511, 1999.

[96] D. Damjanovic. Contributions to the piezoelectric effect in ferroelectric single crystals and ceramics. *Journal of the American Ceramic Society*, 88(10):2663–2676, 2005.

[97] A. K. Soh, Y. C. Song, and Y. Ni. Phase field simulations of hysteresis and butterfly loops in ferroelectrics subjected to electro-mechanical coupled loading. *Journal of the American Ceramic Society*, 89(2):652–661, 2006.

[98] Y. Xiao, V. B. Shenoy, and K. Bhattacharya. Depletion layers and domain walls in semiconducting ferroelectric thin films. *Physical Review Letters*, 95:247603, 2005.

[99] M. B. Okatan, A. L. Roytburd, J. V. Mantese, and S. P. Alpay. Domain engineering in compositionally graded ferroelectric films for enhanced dielectric response and tunability. *Journal of Applied Physics*, 105(11):114106, 2009.

[100] M. B. Okattan, J. V. Mantese, and S. P. Alpay. Effect of space charge on the polarization hysteresis characteristics of monolithic and compositionally graded ferroelectrics. *Acta Materialia*, 58:39–48, 2010.

[101] D. Schrade, R. Müller, and D. Gross. On the physical interpretation of material perameters in phase field models for ferroelectrics. *Archive of Applied Mechanics*, 83(10):1393–1413, 2013.

[102] B. X. Xu, D. Schrade, R. Mueller, and D. Gross. Micromechanical analysis of ferroelectric structures by a phase field method. *Computational Materials Science*, 45(3):832–836, 2009.

[103] D. J. Franzbach, B. X. Xu, R. Mueller, and K. G. Webber. The effects of polarization dynamics and domain switching energies on field induced phase transformations of perovskite ferroelectrics. *Applied Physics Letters*, 99(16), 2011.

[104] T. Sun, X. Wang, H. Wang, X. Zhang, Z. Cheng, C. Z. Sun, and L. Li. A phenomenological model on phase transitions in nanocrystalline barium titanate ceramic. *Journal of the American Ceramic Society*, 2010.

[105] B. Völker, P. Marton, C. Elsässer, and M. Kamlah. Multiscale modeling for ferroelectric materials: A transition from the atomic level to phase-field modeling. *Continuum Mechanics*, 23:435–451, 2011.

[106] B. Völker, C. M. Landis, and M. Kamlah. Multiscale modeling for ferroelectric materials: Identification of the phase-field model's free energy for PZT from atomistic simulations. *Smart Materials and Structures*, 21:035025, 2012.

[107] R. E. García, C. M. Bishop, and W. C. Carter. Thermodynamically consistent variational principles with applications to electrically and magnetically active systems. *Acta Materialia*, 52:11–21, 2004.

[108] R. E. García, W. C. Carter, and S. A. Langer. Finite implementation of a thermodynamic description of piezoelectric mictrostructures. *Journal of the American Ceramic Society*, 88(3):742–749, 2005.

[109] R. E. García, B. D. Huey, and J. E. Blendell. Virtual piezo-force microscopy of polycrystalline ferroelectric films. *Journal of Applied Physics*, 100(064105), 2006.

[110] J. F. Scott. Nanoferroelectrics: statics and dynamics. *Journal of Physics: Condensed Matter*, 18:R361–R386, 2006.

[111] A. Gruverman and A. Kholkin. Nanoscale ferroelectrics: Processing, characterization and future trends. *Reports on Progress in Physics*, 69:2443–2474, 2006.

[112] A. Chung, J. Deen, J. S. Lee, and M. Meyyappan. Nanoscale memory devices. *Nanotechnology*, 21:412001, 2010.

[113] Y. Lei, Y. Chen, and J. D. Lee. Atomistic study of lattice structure of $BiScO_3$. *Computational Materials Science*, 41:242–246, 2007.

[114] Y. He and J. Fan. Multiscale modeling methodology for layered composites of polymer-ferroelectric ceramics. *Journal of Intelligent Material Systems and Structures*, 16(7-8):603–612, 2005.

[115] N. Iles, A. Kellou, K. D. Khodja, B. Amrani, F Lemoigno, D. Dourbie, and H. Aourag. Atomistic study of structural, elastic, electronic and thermal properties of perovskites Ba(Ti, Z, Nb)O_3. *Computational Materials Science*, 39:896–902, 2007.

[116] D. Damjanovic, N. Klein, J. Li, and V. Porokhonskyy. What can be expected from lead-free piezoelectric materials? *Functional Materials Letters*, 3(1):5–13, 2010.

[117] W. W. Wolny. European approach to development of new environmentally sustainable electroceramics. *Ceramics International*, 30:1079–1083, 2004.

[118] T. Takenaka and H. Nagata. Current status and prospects of lead-free piezoelectric ceramics. *Journal of the European Ceramic Society*, 25:2693–2700, 2005.

[119] V. Shur, E. Rumyantsev, E. Nikolaeva, E. Shishkin, I. Baturin, D. Lupascu, J. Nuffer, C. Randall, and M. Ozgul. Kinetics of fatigue in bulk ferroelectrics. In *SPIE Proceedings*, volume 80, pages 1037–1039, 2002.

[120] V. V. Shvartsman, A. L. Kholkin, C. Verdier, Z. Yong, and D. Lupascu. Investigation of fatigue mechanism in ferroelectric ceramic via piezoresponse force microscopy. *Journal of the European Ceramic Society*, 25:2559–2561, 2005.

[121] J. S. Liu, S. R. Zhang, C. Yang, and L. Dai. Domain structure and fatigue behavior of La^{3+}-doped $SrBi_2Ta_2O_9$ thin films. *Journal of the American Ceramic Society*, 88(1):85–88, 2005.

[122] N. Suleimanov, A. Milner, I. Zon, A. Roytburd, and I. Lubomirsky. Evidence of 90° polarization switching in polycrystalline macro-domains of self-supported $BaTiO_3$ films. *Journal of Materials Science*, 44:5312–5317, 2009.

[123] G. Catalan, J. Seidel, R. Ramesh, and J. F. Scott. Domain wall nanoelectronics. *Reviews of Modern Physics*, 84:119–156, 2012.

[124] V. Shelke, D. Mazumdar, S. Jesse, S. Kalinin, A. Baddorf, and A. Gupta. Ferroelectric domain scaling and switching in ultrathin $BiFeO_3$ films deposited on vicinal substrates. *New Journal of Physics*, 14:053040, 2012.

[125] J. F. Scott. Self-assembly and switching in ferroelectrics and multiferroics. *Europhysics Letters*, 103:37001, 2013.

[126] D. Szwarcman, S. Prosandeev, L. Louis, S. Berger, Y. Rosenberg, Y. Lereah, L. Bellaiche, and G. Markovich. The stabilization of a single domain in free-standing ferroelectric nanocrystals. *Journal of the Physics: Condensed Matter*, 26:122202, 2014.

[127] R. W. C. Lewis, A. C. E. Dent, R. Stevens, and C. R. Bowen. Microstructural modelling of the polarization and properties of porous ferroelectrics. *Smart Materials and Structures*, page 085002, 2011.

[128] J. Wang and M. Kamlah. Three-dimensional finite element modeling of polarization switching in a ferroelectric single domain with an impermeable notch. *Smart Materials and Structures*, page 104008, 2009.

[129] A. Abdollahi and I. Arias. Phase-field simulation of anisotropic crack propagation in ferroelectric single crystals: Effect of microstructure on the fracture process. *Modelling and Simulation in Materials Science and Engineering*, page 074010, 2011.

[130] E. Y. Tsymbal and H. Kohlstedt. Tunneling across a ferroelectric. *Science*, 313:181–183, 2006.

[131] S. Trimper, T. Michael, and J. Wesselinowa. Ferroelectric soft modes and Gilbert damping. *Physical Review B 76*, 76:094108, 2007.

[132] S. Wan and K. Bowman. Modeling of electric field induced texture in lead zirconate titanate ceramics. *Journal of Materials Research*, 16(8):2306–2312–3, 2001.

[133] E. Suhir. An approximate analysis of stresses in multilayered elastic thin films. *ASME Journal of Applied Mechanics*, 55:143–148, 1988.

[134] E. Suhir. Analysis of interfacial thermal stresses in a trimaterial assembly. *Journal of Applied Physics*, 89(7):3685–3694, 2001.

[135] C. E. Murray and I. C. Noyan. Finite-size effects in thin-film composites. *Philosophical Magazine A*, 82(16):3087–3117, 2002.

[136] M. Y. Tsai, C. H. Hsu, and C. N. Han. A note on Suhir's solution of thermal stresses for a die-substrate assembly. *Journal of Electronic Packaging*, 126:115–119, 2004.

[137] V. Nagarajan. Scaling of the piezoelectric response in ferroelectric nanostructures: An effective clamping stress model. *Applied Physics Letters*, 87(242905), 2005.

[138] D. M. Kim, C. B. Eom, V. Nagarajan, J. Ouyang, R. Ramesh, V. Vaithynathan, and D. G. Schlom. Thickness dependence of structural and piezoelectric properties of epitaxial $Pb(Zr_{0.52}Ti_{0.48})O_3$ films on Si and $SrTiO_3$ substrates. *Applied Physics Letters*, 88(142904), 2006.

[139] T.M. Shaw, S. Trolier-McKinstry, and P. McIntyre. The properties of ferroelectric films at small dimensions. *Annual Review of Materials Science*, 30:263–298, 2000.

[140] S. Dunn. Determination of cross sectional variation of ferroelectric properties for thin film (ca. 500 nm) PZT (30/70) via PFM. *Integrated Ferroelectrics*, 59:1505–1512, 2003.

[141] Y.H. Chu, L. W. Martin, Q. Zhan, P. L. Yang, M. P. Cruz, K. Lee, M. Barry, S. Y. Yang, and R. Ramesh. Epitaxial multiferroic $BiFeO_3$ thin films: Progress and future directions. *Ferroelectrics*, 354:167–177, 2007.

[142] E.-M. Anton, R. E. García, T. S. Key, J. E. Blendell, and K. J. Bowman. Domain switching mechanisms in polycrystalline ferroelectrics with asymmetric hysteretic behavior. *Journal of Applied Physics*, 105(024107), 2009.

[143] S. Bühlmann, B. Dwir, J. Baborowski, and P. Muralt. Size effect in mesoscopic epitaxial ferroelectric structures: Increase of piezoelectric response with decreasing feature size. *Applied Physics Letters*, 80(17):3195–3197, 2002.

[144] A. Ferri, A. Da Costa, S. Saitezk, R. Desfeux, M. Datalle, G. S. Wang, and D. Remiens. Local piezoelectric hysteresis loops for the study of electrical properties of $0.7Pb(Mg_{1/3}Nb_{2/3})O_3$-$0.3PbTiO_3$ thin films: Bottom electrode dependence and film thickness effect. *Ferroelectrics*, 362:21–29, 2008.

[145] M. Alexe, C. Harnagea, D. Hesse, and U. Gösele. Patterning and switching of nanosize ferroelectric memory cells. *Applied Physics Letters*, 75(12):1793–1795, 1999.

[146] G. A. C. M. Spierings, G. J. M. Dormans, W. G. J. Moors, M. J. E. Ulenaers, and P. K. Larsen. Stresses in $Pt/Pb(Zr,Ti)O_3/Pt$ thin-film stacks for integrated ferroelectric capacitors. *Journal of Applied Physics*, 78(3):1926–1933, 1995.

[147] S. Tiedke, Schmitz. T., K. Prume, A. Roelofs, T. Schneller, U. Kall, R. Waser, C. S. Ganpule, V. Nagarajan, A. Stanishevesky, and R. Ramesh. Direct hysteresis measurements of single nanosized ferroelectric capacitors contacted with an atomic force microscope. *Applied Physics Letters*, 79:3678–3680, 2001.

[148] V. Nagarajan, S. Prasertchoung, T. Zhao, H. Zheng, J. Ouyang, R. Ramesh, W. Tian, X. Q. Pan, D. M. Dim, C. B. Eom, H. Kohlstedt, and R. Waser. Size effects in ultrathin epitaxial ferroelectric heterostructures. *Applied Physics Letters*, 84:5225–5227, 2004.

[149] I. C. Noyan, C. E. Morray, and J. S. Chey. Finite size effects in stress analysis of interconnect structures. *Applied Physics Letters*, 85(5):724–726, 2004.

[150] M. Östling, S. M. Koo, C. M. Zetterling, S. Khartsev, and A. Grishin. Ferroelectric thin films on silicon carbide for next-generation nonvolatile memory and sensor devices. *Thin Solid Films*, 469-470:444–449, 2004.

[151] M. M. Saad, R. M. Bowman, and J. M. Gregg. Thin film capacitor cut from single crystals using focused ion beam milling. *Integrated Ferroelectrics*, 61:239–248, 2004.

[152] A. K. Tagantsev, G. Gerra, and N. Setter. Short-range and long-range contributions to the size effect in metal-ferroelectric-metal heterostructures. *Physical Review B*, 77(174111), 2008.

[153] M. Stengel, D. Vanderbilt, and N. A. Spaldin. Enhancement of ferroelectricity at metal-oxide interfaces. *Nature Materials*, 8:392–397, 2009.

[154] M. D. Glinchuk, E. A. Eliseev, and A. N. Morozovska. Influence of built-in internal electric field on ferroelectric film properties and phase diagram. *Ferroelectrics*, 354:86–98, 2007.

[155] Q. Y. Qiu, R. Mahjoub, S. P. Alpay, and V. Nagarajan. Misfit strain-film thickness phase diagrams and related electromechanical properties of epitaxial ultra-thin lead zirconate titanate films. *Acta Materialia*, 58(3):823–835, 2010.

[156] A. G. Zembilgotov, N. A. Pertsev, H. Kohlstedt, and R. Waser. Ultrathin epitaxial ferroelectric films grown on compressive substrates: Competition between the surface and strain effects. *Journal of Applied Physics*, 91(4):2247–2254, 2002.

[157] A. Vasudevarao, S. Denev, M. D. Biegalski, Y. Li, L.-Q. Chen, S. Trolier-McKinstry, D. G. Schlom, and V. Gopalan. Polarization rotation transitions in anisotropically strained $SrTiO_3$ thin films. *Applied Physics Letters*, 92(192902), 2008.

[158] R. Jiménez, H. Amorín, J. Ricote, J. Carreaud, J. M. Kiat, B. Dkhil, H. Holc, M. Kosec, and M. Algueró. Effect of grain size on the transition between ferroelectric and relaxor states in $0.8Pb(Mg_{1/3}Nb_{2/3})O_3$-$0.2PbTiO_3$ ceramics. *Physical Review B*, 78(094103), 2008.

[159] J. S. Liu, S. R. Zhang, H. Z. Zeng, C. T. Yang, and Y. Yuan. Coercive field dependence of the grain size of ferroelectric films. *Physical Review B*, 72(172101), 2005.

[160] A. N. Morozovska, S. V. Svechnikov, E. A. Eliseev, and S. V. Kalinin. Extrinsic size effect in piezoresponse force microscopy of thin films. *Physical Review B*, 76(054123), 2007.

[161] E. Suhir. Stresses in bi-metal thermostats. *ASME Journal of Applied Mechanics*, 53:657–660, 1986.

[162] E. Suhir. Approximate evaluation of the elastic thermal stresses in a thin film fabricated on a very thick circular substrate. *Journal of Electronic Packaging*, 116:171–176, 1994.

[163] V. Nagarajan, A. Roytburd, A. Stanishevsky, S. Prasertchoung, T. Zhao, L. Chen, J. Melngailis, O. Auciello, and R. Ramesh. Dynamics of ferroelastic domains in ferroelectric thin films. *Nature Materials*, 2:43–47, 2003.

[164] W. A. Dollase. Correction of intensities for preferred orientation in powder diffractometry: Application of the March model. *Journal of Applied Crystallography*, 19:267–272, 1986.

[165] H. J. Bunge. *Texture Analysis in Materials Science: Mathematical Methods.* Butterworth, London, 1982.

[166] J. E. Blendell, M. D. Vaudin, and E. R. Fuller. Determination of texture from individual grain orientation measurements. *Journal of the American Ceramic Society*, 82(11):3217–3220, 1999.

[167] E. Zolotoyabko. Determination of the degree of perferred orientation within the March-Dollase approach. *Journal of Applied Crystallography*, 42(3):513–518, 2009.

[168] S. A. Langer, W. C. Carter, and Jr. E. R. Fuller. OOF: Analysis of real material microstructures. http://www.ctcms.nist.gov/oof/., 1999.

[169] A. Wu, P. Vilarinho, D. Wu, and A. Gruverman. Abnormal domain switching in Pb(Zr, Ti)O_3 thin film capacitors. *Applied Physics Letters*, 93(26):262906, 2008.

[170] Z. Zhao, R. E. García, and K. J. Bowman. Modeling 180° domain switching population dynamics in polycrystalline ferroelectrics. *Journal of the American Ceramic Society*, 95(5):1619–1627, 2012.

[171] A. Pramanick, D. Damjanovic, J. E. Daniels, J. C. Nino, and J. L. Jones. Origins of electro-mechanical coupling in polycrystalline ferroelectrics during subcoercive electrical loading. *Journal of the American Ceramic Society*, 94(2):293–309, 2011.

[172] A. Gruverman, O. Auciello, and H. Tokumoto. Imaging and control of domain structures in ferroelectric thin films via scanning force microscopy. *Annual Review of Material Science*, 28:101–123, 1998.

[173] S. Choudhury, Y. L. Li, C. Krill III, and L.-Q. Chen. Phase-field simulation of polarization switching and domain evolution in ferroelectric polycrystals. *Acta Materialia*, 53:5313–5321, 2005.

[174] S. Choudhury, Y. L. Li, C. Krill III, and L.-Q. Chen. Effect of grain orientation and grain size on ferroelectric domain switching and evolution: Phase field simulations. *Acta Materialia*, 55:1415–1426, 2007.

[175] S. Wicks, V. Anbusathaiah, and V. Nagarajan. Nanoscale domain switching behaviour in polycrystalline ferroelectric thin films. *Nanotechnology*, 18:465502, 2007.

[176] S. Wicks, K. Seal, S. Jesse, V. Anbusathaiah, S. Leach, R. E. García, S. V. Kalinin, and V. Nagarajan. Collective dynamics in nanostructured polycrystalline ferroelectric thin films using local time-resolved measurements and switching spectroscopy. *Acta Materialia*, 58:67–75, 2010.

[177] Y. Jing, J.E. Blendell, and K. J. Bowman. Three dimensional piezoresponse force microscopy polarization difference maps. *Journal of Applied Physics*, 109(7):074110, 2011.

[178] A. Roelofs, U. Böttger, R. Waser, F. Schlaphof, S. Trogisch, and L.M. Eng. Differentiating 180° and 90° switching of ferroelectric domains with three-dimensional piezoresponse force microscopy. *Applied Physics Letters*, 77(21):3444–3446, 2000.

[179] V. Nagarajan, S. Aggarwal, A. Gruverman, R. Ramesh, and R. Waser. Nanoscale polarization relaxation in a polycrystalline ferroelectric thin film: Role of local environments. *Applied Physics Letters*, 86:262910, 2005.

[180] Y. Jing, J. E. Blendell, R. E. García, and S. E. Leach. Correlated inter-grain switching in polycrystalline ferroelectric thin films. *In press, Journal of Applied Physics*, 2014.

[181] M. Hambe, W. Wicks, J. M. Gregg, and V. Nagarajan. Creation of damage-free ferroelectric nanostructures via focused ion beam milling. *Nanotechnology*, 19(17):175302, 2008.

[182] D. Fu, K. Suzuki, K. Kato, and H. Suzuki. Dynamics of nanoscale polarization backswitching in tetragonal lead zirconate titanate thin film. *Applied Physics Letters*, 82:21302132, 2003.

[183] A. Gruverman, A. Kholkin, A. Kingon, and H. Tokumoto. Asymmetric nanoscale switching in ferroelectric thin films by scanning force microscopy. *Applied Physics Letters*, 78(18):2751–2753, 2001.

[184] S. Jesse, A.P. Baddorf, and S. V. Kalinin. Switching spectroscopy piezoresponse force microscopy of ferroelectric materials. *Applied Physics Letters*, 88(6):062908, 2006.

[185] S. R. Gilbert, S. Hunter, D. Ritchey, C. Chi, D. V. Taylor, J. Amano, S. Aggarwal, T. S. Moise, T. Sakoda, S. R. Summerfelt, K. K. Singh, C. Kazemi, D. Carl, and B. Bierman. Preparation of $Pb(Zr,Ti)O_3$ thin films by metalorganic chemical vapor deposition for low voltage ferroelectric memory. *Journal of Applied Physics*, 93(3):1713–1717, 2003.

[186] J. L. Jones, E. B. Slamovich, and K. J. Bowman. Domain texture distributions in tetragonal lead zirconate titanate by x-ray and neutron diffraction. *Journal of Applied Physics*, 97(3):034113, 2005.

[187] W. Liu and X. Ren. Large piezoelectric effect in Pb-free ceramics. *Physical Review Letters*, 103:257602, 2009.

[188] Z.-M. Wang, K. Zhao, X.-L. Guo, W. Sun, H.-L. Jiang, X.-Q. Han, X.-T. Tao, Z.-X. Cheng, H. Kimura, G.-L. Yuan, J. Yin, and Z.-G. Liu. Crystallization, phase evolution and ferroelectric properties of sol-gel-synthesized $Ba(Ti)_{0.8}Zr_{0.2}O_3$-x$(Bz_{0.7}Ca_{0.3})TiO_3$ thin films. *Journal of Materials Chemistry C*, 1:522–530, 2013.

[189] D. Xue, Y. Zhou, H. Bao, C. Zhou, J. Gao, and X. Ren. Elastic, piezoelectric, and dielectric properties of $Ba(Zr_{0.2}Ti_{0.8})O_3$-$50(Ba_{0.7}Ca_{0.3})TiO_3$ Pb-free ceramic at the morphotropic phase boundary. *Journal of Applied Physics*, 109:054110, 2011.

[190] S. Yao, W. Ren, H. Ji, X. Wu, P. Shi, D. Xue, X. Ren, and Z.-G. Ye. High pyroelectricity in lead-free $0.5Ba(Zr_{0.2}Ti_{0.8})O_3$-$0.5(Ba_{0.7}Ca_{0.3})TiO_3$. *Journal of Applied Physics D: Applied Physics*, 45:195301, 2012.

[191] M. C. Ehmke, S. N. Ehrlich, J. E. Blendell, and K. J. Bowman. Phase coexistence and ferroelastic texture in high strain (1-x)$Ba(Zr_{0.2}Ti_{0.8})O_3$-x$(Ba_{0.7}Ca_{0.3})TiO_3$. *Journal of Applied Physics*, 111:124110, 2012.

[192] W. Li, Z. Xu, R. Chu, P. Fu, and G. Zang. Piezoelectric and dielectric properties of $(Ba_{1-x}Ca_x)(Ti_{0.95}Zr_{0.05})O_3$ lead-free ceramics. *Journal of the American Ceramic Society*, 90(10):2942–2944, 2010.

[193] Y. Saito, H. Takao, T. Tani, T. Nonoyama, K. Takatori, T. Homma, T. Nagaya, and M. Nakamura. Lead-free piezoceramics. *Letters to Nature*, 432:84–87, 2004.

[194] A. Piorra, A. Petraru, H. Kohlstedt, M. Wuttig, and E. Quandt. Piezoelectric properties of $0.5(Ba_{0.7}Ca_{0.3}TiO_3)$-$0.5[Ba(Zr_{0.2}Ti_{0.8})O_3]$ ferroelectric lead-free laser deposited thin films. *Journal of Applied Physics*, 109:104101, 2011.

[195] J. Gao, D. Xue, Y. Wang, D. Wang, L. Zhang, H. Wu, S. Guo, H. Bao, C. Zhou, W. Liu, S. Hou, G. Xiao, and X. Ren. Microstructure basis for strong piezoelectricity in Pb-free $Ba(Zr_{0.2}Ti_{0.8})O_3$-$(Ba_{0.7}Ca_{0.3})TiO_3$. *Applied Physics Letters*, 99:092901, 2011.

[196] B. Li, J. E. Blendell, and K. J. Bowman. Temperature-dependent poling behavior of lead-free BZT-BCT piezoelectrics. *Journal of the American Ceramic Society*, 94(10):3192–3194, 2011.

[197] D. Damjanovic, A. Biancoli, L. Batooli, A. Vahabzadeh, and J. Trodahl. Elastic, dielectric, and piezoelectric anomalies and raman spectroscopy of $0.5Ba(Ti_{0.8}Zr_{0.2})O_3$-$0.5(Ba_{0.7}Ca_{0.3})TiO_3$. *Applied Physics Letters*, 100:192907, 2012.

[198] G. Tutuncu, B. Li, K. Bowman, and J. L. Jones. Domain wall motion and electromechanical strain in lead-free piezoelectrics: Insight from the model system (1- x)$Ba(Zr_{0.2}Ti_{0.8})O_3$ - x$(Ba_{0.7}Ca_{0.3})TiO_3$ using in situ high-energy x-ray diffraction during application of electric fields. *Journal of Applied Physics*, 2014.

[199] Z. Zhao. *Modeling Ferroelectric Hysteresis Dynamics in Lead-Containing and Lead-Free Materials*. PhD thesis, Purdue University, 2012.

[200] M. C. Ehmke. Unpublished polarization hysteresis data as a function of temperature. BZT-50BCT. Data supplied as digital files.

[201] V. Nagarajan. Unpublished data, 2008. see V. Nagarajan for details.

APPENDICES

Appendix A Material Properties

Table A.1: Physical properties used to describe simulated PZN-PT film [109].

Symbol	Value	Units		Symbol	Value	Units
C_{11}	111.0	GPa		Q_{11}	0.186	m^4/C^2
C_{33}	105.0	GPa		Q_{12}	-0.09	m^4/C^2
C_{44}	64.0	GPa		Q_{44}	0.013	m^4/C^2
C_{12}	102.0	GPa		a	-23310023	$J{\cdot}m/C^2$
C_{13}	101.0	GPa		b	372960372	$J{\cdot}m^5/C^4$
C_{66}	63.0	GPa		c	0	$J{\cdot}m^9/C^6$
ϵ_{11}^{σ}	26.562×10^{-9}	F/m		ϵ_{33}^{σ}	8.854×10^{-9}	F/m
d_{33}	200.0×10^{-11}	C/N		α_{11}	5×10^{-7}	1/K
d_{31}	-97.0×10^{-11}	C/N		α_{33}	-3×10^{-6}	1/K
d_{15}	14.0×10^{-11}	C/N		M_P	1×10^{-5}	S/m

Table A.2: Physical properties used in the numerical simulation of PZT film. [109,201]

Symbol	Value	Units		Symbol	Value	Units	Reference
C_{11}	172.0	GPa		Q_{11}	0.0789	m^4/C^2	[201]
C_{33}	33.8	GPa		Q_{12}	-0.0248	m^4/C^2	[201]
C_{44}	76.4	GPa		Q_{44}	0.0636	m^4/C^2	[201]
C_{12}	78.9	GPa		a	-23310023	$J{\cdot}m/C^2$	[201]
C_{13}	25.4	GPa		b	56909236	$J{\cdot}m^5/C^4$	[201]
C_{66}	118.0	GPa		c	0	$J{\cdot}m^9/C^6$	[201]
ϵ_{11}^{σ}	1.04×10^{-9}	F/m		ϵ_{33}^{σ}	1.94×10^{-9}	F/m	[201]
d_{33}	10.4×10^{-11}	C/N		α_{11}	5×10^{-7}	1/K	[109]
d_{31}	-3.26×10^{-11}	C/N		α_{33}	-3×10^{-6}	1/K	[109]
d_{15}	7.86×10^{-11}	C/N		M_P	1×10^{-5}	S/m	[109]

Appendix B Thermal Effects and Fitting Parameters

The following method for extracting Landau coefficients from experimentally measured polarization hysteresis data was developed by Zizhao Zhao [199].

For a stress-free solid, the first four terms of Equation 2.3 are arranged so that:

$$E = aP + bP^3 + cP^5 \tag{B.1}$$

Where $a = \alpha(T - Tc)$. When the coercive field value is equal to zero, the polarization is equal to the remnant polarization, P_r. So the equation becomes

$$0 = aP + bP^3 + cP^5 \tag{B.2}$$

At $E = 0$, the dielectric susceptibility, χ is defined as $\partial P/\partial E$, so that Equation 4.1 can be expressed as:

$$\frac{1}{\chi} = a + 3bP^2 + 5cP^4 \tag{B.3}$$

Equation B.2 can be divided by P to yield

$$0 = a + bP^2 + cP^4 \tag{B.4}$$

which can be solved for P when given the fitted a, b, and c coefficients. This can be used to check the difference between the experimental and fitted values of P.

The mobility of the polarization switching, M, can be determined from experimental data by taking the derivative of Equation 2.1 for the condition when the applied field E is equal to the coercive field value and the polarization, $P = 0$, which yields:

$$\frac{\partial f}{\partial P}|_{P=0,E=E_c} = -E_c \tag{B.5}$$

Substituting this result into Equation 2.4 leads to $\partial P/\partial t = ME_c$. The value of E_c in a sinusoidally varying electric field is $E = E_0 sin(\omega t)$, where E_0 is the maximum

applied electric field value, ω is the frequency, and t is the time. At $t = t_c$, the instant where the electric field is a the coercive field value, $E_c = E_0 sin(\omega t_c)$. Equation 2.4 is then reduced to $\partial P/\partial t = M E_0 sin(\omega t_c)$. Using this equation and applying the chain rule, Equation 2.4 can be written as:

$$\frac{\partial P}{\partial t} = \frac{\partial P}{\partial E}\frac{\partial E}{\partial t} = \chi \omega E_0 cos(\omega t_c) = M E_c \tag{B.6}$$

An expression for M is developed from the relationship between Equation B.6 and $E = E_0 sin(\omega t)$. Using Pythagoras's theorem yields

$$M = \chi \omega \sqrt{\frac{E_0^2}{E_c^2} - 1} \tag{B.7}$$

Determination of the coefficients at each temperature was based on the statistical minimization of the difference between the experimental and calculated P_r, E_c, and the maximum polarization. The statistical errors for P_r, E_c and P_{max} were typically less than 2%. Although as the temperature increased, the error between the experimental maximum polarization value and the fitted value increased, but remained below 5%. Permittivity, mobility, and coercive field were adjusted at each temperature to arrive at an optimized correlation to the experimental results. Table B.1 summarizes the experimental values of P_r and E_c as a function of temperature, extracted from experimental results. The fitting strategy assumed a first-order ferroelectric transition where the α and c coefficients have positive values and the b coefficient has a negative value. Figures B.1 and B.2 show the experimental polarization hysteresis loops and the fitted loops for temperatures from 293 K to 353 K. The experimental polarixation loops for 293 K shown in Figure B.1 show good correlation between the data from Xue [189], Yao [190], Ehmke [191] and the fitted loop, even though the experimental measurements were acquired at three different frequencies. The fitted loops match the experimental values of P_r and E_c for the entire tempera-

ture range, but the P_{max} values for the fitted loops are lower than the experimental values for the high temperatures.

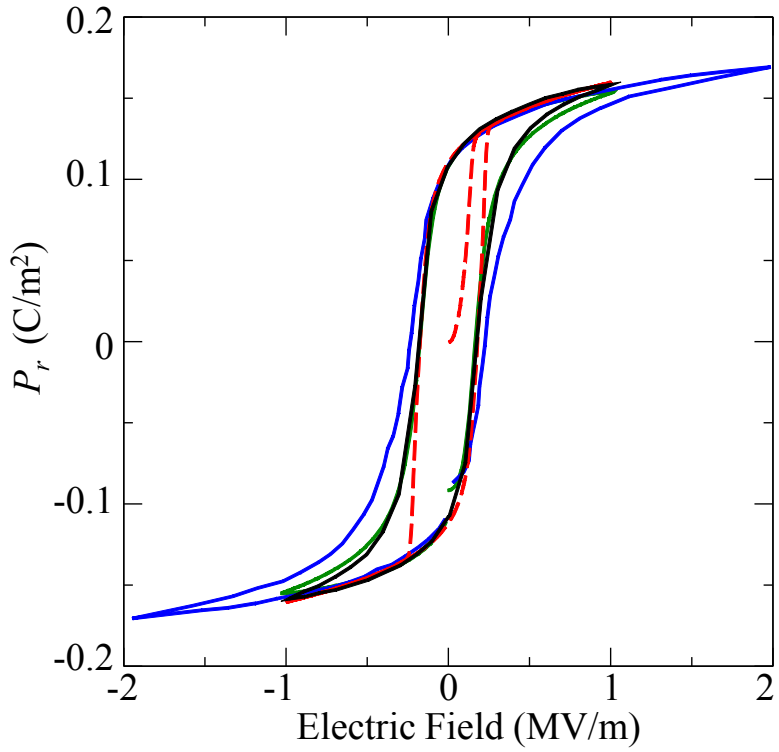

Figure B.1.: Polarization hysteresis loops at 293 K for three sets of experimental data and the loop generated by the model (dashed red line). The experimental data is from Xue [189] (blue line), Yao [190] (green line), and Ehmke [191] (black line). There is a close correlation of the remnant polarization and coercive field values for all three experimental conditions and for the model. The Xue data was acquired at a frequency of 10 Hz with a maximum electric field value of 2 MV/m. The Yao data was collected at 1 Hz with a maximum electric field value of 1 MV/m. The Ehmke data was acquired at 0.1 Hz with a maximum electric field value of 1 MV/m. The model used 0.1 Hz and a maximum electric field value of 1 MV/m.

Using data separately from the two temperature ranges allowed the closest fitting of the coefficients to the experimental results. Tables B.2 and B.3 summarize the details of fitting parameters for each individual coefficient. Figures B.3, B.4, and B.5 show the model Landau coefficients as a function of temperature. The circles show the coefficient values extracted from the published experimental data and the

lines indicate the results of fitting a temperature-dependent equation to the extracted results.

Table B.1: Temperature, Remnant Polarization, and Coercive Field from Experimental Results

Temperature (K)	P_r (C/m_2)	E_c (V/m)	method	Source
223	0.129	350000	digitized plot	Xue [189]
238	0.127	335000	digitized plot	Xue
253	0.125	320000	digitized plot	Xue
273	0.12	225000	digitized plot	Xue
283	0.115	200000	digitized plot	Xue
293	0.11	225000	digitized plot	Xue
293	0.11	225000	digitized plot	Yao [190]
296	0.109	180000	loop points file	Ehmke [191]
303	0.10	173000	loop points file	Ehmke
313	0.083	218000	loop points file	Ehmke
323	0.076	207000	loop points file	Ehmke
333	0.070	200000	digitized plot	Xue
333	0.069	181000	loop points file	Ehmke
343	0.061	151000	loop points file	Ehmke
353	0.049	113000	loop points file	Ehmke
363	0.013	60400	loop points file	Ehmke
373	0.006	44000	loop points file	Ehmke

Table B.2: Landau coefficient fitting parameters as a function of temperature, T, for the rhombohedral phase.

Coefficient	Equation Form	Parameter	Value	Units
α	A × exp(B×T)+C	A	5.0×10^3	$J{\cdot}m/C^2K$
		B	4.83×10^{-2}	K^{-1}
		C	3.0×10^3	$J{\cdot}m/C^2K$
b	A × exp(B×T)+C	A	1.12×10^{-8}	$J{\cdot}m^5/C^4$
		B	1.255×10^{-1}	K^{-1}
		C	3.45×10^8	$J{\cdot}m^5/C^4$
c	A × exp(B×T)+C	A	1.8×10^{10}	$J{\cdot}m^9/C^6$
		B	9.0×10^{-4}	K^{-1}
		C	0.0	$J{\cdot}m^9/C^6$

Table B.3: Landau coefficient fitting parameters as a function of temperature, T, for the tetrahedral phase.

Coefficient	Equation Form	Parameter	Value	Units
α	A $\times$ exp(B$\times$T)+C	A	6.19	J·m/C^{2}K
		B	2.58×10^{-2}	K^{-1}
		C	4.8×10^{3}	J·m/C^{2}K
b	A $\times$ exp(B$\times$T)+C	A	2.0×10^{-7}	J·m^5/C^4
		B	8.3×10^{-2}	K^{-1}
		C	7.0×10^{6}	J·m^5/C^4
c	A $\times$ exp(B$\times$T)+C	A	1.0×10^{3}	J·m^9/C^6
		B	5.3×10^{-2}	K^{-1}
		C	1.0×10^{10}	J·m^9/C^6

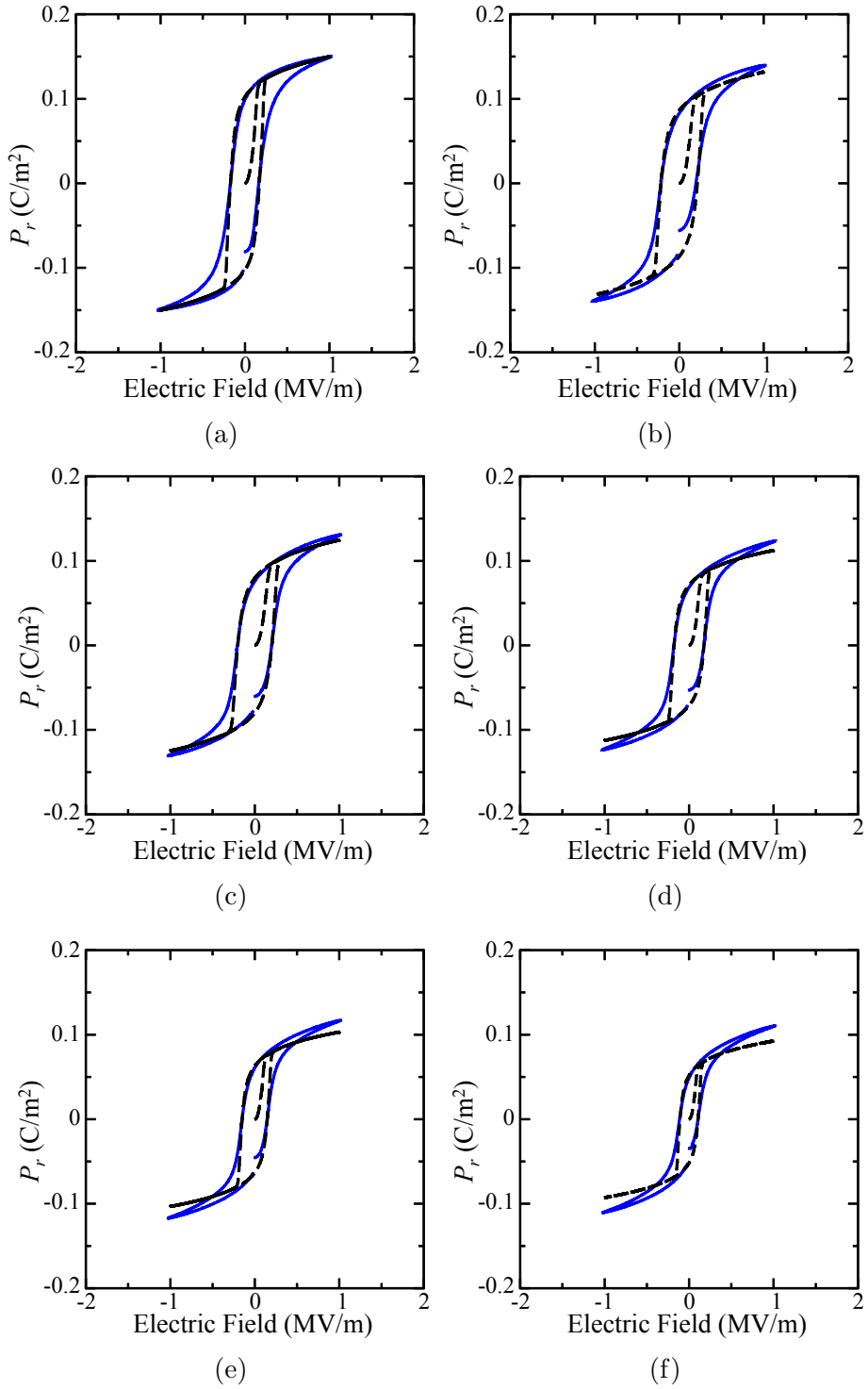

Figure B.2.: Polarization hysteresis loops for: (a) 303 K, (b) 313 K, (c) 323 K, (d) 333 K, (e) 343 K, (f) 353 K. Experimental results from Ehmke [191] are shown as blue solid lines and the fitted results are shown as black dashed lines.

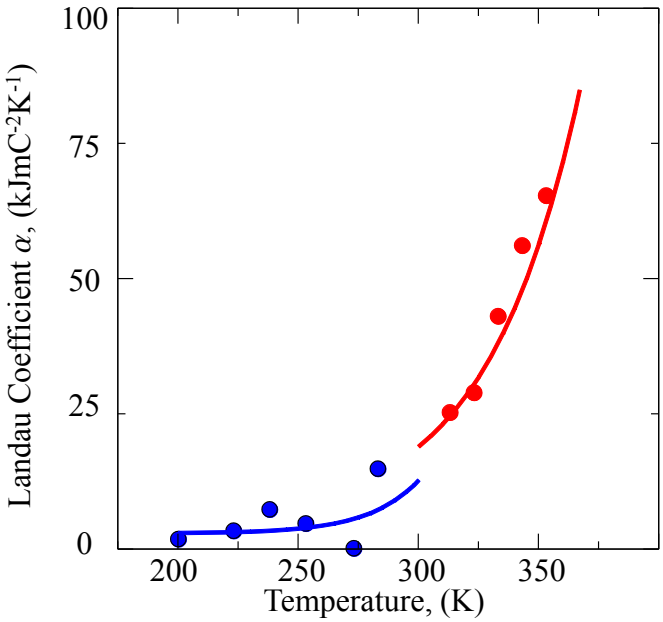

Figure B.3.: Landau coefficient α vs Temperature fitted to experimental data from Xue (blue circles) [189] and Ehmke (red circles) [191]. The fitted equations are plotted as continuous curves. Experimental values near the MPB were not included in the development of the temperature-dependent equation.

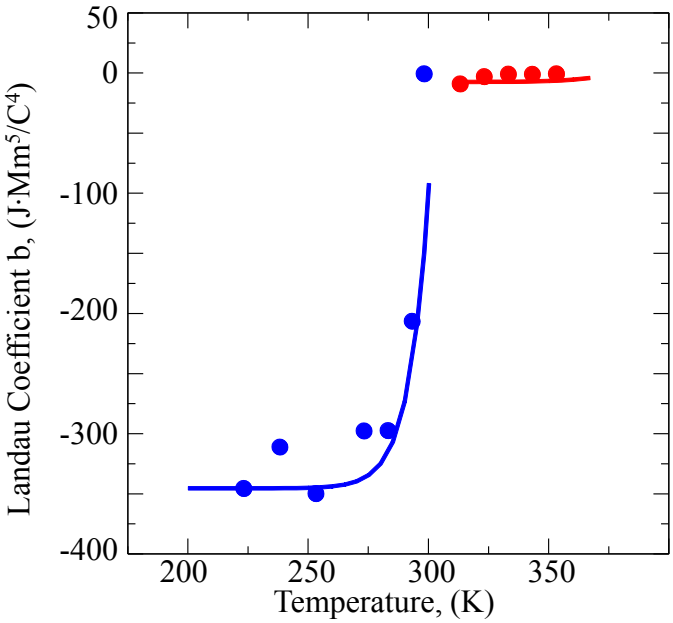

Figure B.4.: Landau coefficient b vs Temperature fitted to experimental data from Xue (blue) [189] and Ehmke (red) [191]. The fitted equations are plotted as continuous curves. Experimental values near the MPB were not included in the development of the temperature-dependent equation.

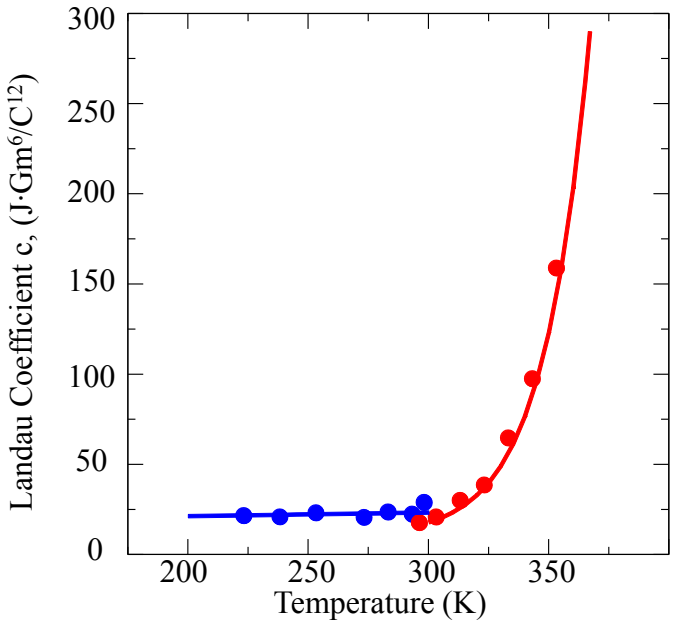

Figure B.5.: Landau coefficient c vs Temperature fitted to experimental data from Xue (blue) [189] and Ehmke (red) [191]. The fitted equations are plotted as continuous curves.

VITA

VITA

Sarah E. Leach was born and raised in Illinois. She earned her Bachelor's degree in mechanical engineering from Vanderbilt University in Nashville, Tennessee and returned to Illinois to work for Micro Switch, a Honeywell Division. Her work with electromechanical devices led to employment at CTS Corporation in Elkhart, Indiana. The direction of her work at CTS motivated her to complete a Master's degree in Materials Engineering at the University of Notre Dame. After a number of years in industry she joined the faculty of the Purdue College of Technology in South Bend, Indiana. She was tenured in 2005 and began working on her PhD in the school of Materials Engineering under the supervision of Professor R. Edwin García in August 2006.